

**The Incorporation of Geophysical, Petrophysical and Geological Constraints in
Gravity Modeling to Resolve Structures at Depth.**

by

Fabiano Della Justina

A thesis submitted in partial fulfillment of the requirements for the degree of
Doctor of Philosophy (PhD) in Mineral Deposits and Precambrian Geology

The School of Graduate Studies - Laurentian University

Harquail School of Earth Sciences

Mineral Exploration Research Centre

Sudbury, Ontario, Canada

© Fabiano Della Justina, 2022

THESIS DEFENCE COMMITTEE/COMITÉ DE SOUTENANCE DE THÈSE
Laurentian Université/Université Laurentienne
Office of Graduate Studies/Bureau des études supérieures

Title of Thesis Titre de la thèse	The Incorporation of Geophysical, Petrophysical and Geological Constraints in Gravity Modeling to Resolve Structures at Depth
Name of Candidate Nom du candidat	Della Justina, Fabiano
Degree Diplôme	Doctor of Philosophy
Department/Program Département/Programme	Mineral Deposits and Precambrian Geology
	Date of Defence Date de la soutenance December 21, 2022

APPROVED/APPROUVÉ

Thesis Examiners/Examineurs de thèse:

Dr. Richard Smith
(Co-Supervisor/Co-directeur(trice) de thèse)

Dr. Harold Gibson
(Co-Supervisor/Co-directeur(trice) de thèse)

Mr. Alan King
(Committee member/Membre du comité)

Dr. Hernan Ugalde
(External Examiner/Examineur externe)

Dr. Corey Laamanen
(Internal Examiner/Examineur interne)

Approved for the Office of Graduate Studies
Approuvé pour le Bureau des études supérieures
Tammy Eger, PhD
Vice-President Research (Office of Graduate Studies)
Vice-rectrice à la recherche (Bureau des études supérieures)
Laurentian University / Université Laurentienne

ACCESSIBILITY CLAUSE AND PERMISSION TO USE

I, **Fabiano Della Justina**, hereby grant to Laurentian University and/or its agents the non-exclusive license to archive and make accessible my thesis, dissertation, or project report in whole or in part in all forms of media, now or for the duration of my copyright ownership. I retain all other ownership rights to the copyright of the thesis, dissertation or project report. I also reserve the right to use in future works (such as articles or books) all or part of this thesis, dissertation, or project report. I further agree that permission for copying of this thesis in any manner, in whole or in part, for scholarly purposes may be granted by the professor or professors who supervised my thesis work or, in their absence, by the Head of the Department in which my thesis work was done. It is understood that any copying or publication or use of this thesis or parts thereof for financial gain shall not be allowed without my written permission. It is also understood that this copy is being made available in this form by the authority of the copyright owner solely for the purpose of private study and research and may not be copied or reproduced except as permitted by the copyright laws without written authority from the copyright owner.

ABSTRACT

Gravity modeling is an important tool for interpreting and understanding geological structures in the subsurface. In forward modeling or inverse modeling, the main goal is to modify a geophysical/geological model to accomplish an acceptable level of reproducibility in the observed data. However, due to the non-uniqueness of potential-field data, more than one model might fit the observed data. In order to reduce the number of acceptable models, constraints are commonly incorporated into the model. There are countless studies available in the literature demonstrating the necessity of constraining gravity and magnetic models. However, typically they do not demonstrate the individual enhancements that come as a consequence of integrating each constraint into the geophysical model. This study demonstrates how the model, either inverse or forward, is improved as new constraints are built into the modeling workflow. The constraints include information from a density compilation, high-resolution seismic sections, geological maps as well as geological interpretations. The mapped surface geology and the density of this surface data were important to explain the gravity variations associated with faults and to estimate the dip and the error in this dip estimation. The high-resolution seismic sections were helpful to identify reflective features that were most likely lithological contacts where there could be changes in density. Incorporating some of these deeper features and the gradual changes in depth evident in the seismic data resulted in changes in the thickness of the near-surface rocks that was more consistent along strike. Information from previous studies in the area, such as geological interpretations of seismic sections, were required to ensure the geological feasibility of gravity models.

KEYWORDS

Gravity modeling, forward model, inverse model, petrophysics, error analysis, Abitibi greenstone belt, Porcupine-Destor fault, Porcupine assemblage, Deloro assemblage, Matheson, Lake Wanapitei.

CO-AUTHORSHIP STATEMENT AND STRUCTURE OF THE THESIS

Parts of this thesis are drawn from two extended abstracts presented at conferences (Della Justina and Smith, 2020; Della Justina and Smith, 2021). The first extended abstract forms the basis of Chapter 4 and the second is part of Chapter 5. This thesis is written in such a way that each chapter can be submitted with minor modification to a journal. Hence, each chapter has its own standalone introduction and conclusions. The introduction and conclusion chapters of the thesis are therefore brief. The introductory chapter outlines the general objective of the thesis and introduces the individual chapters and the concluding chapter draws general conclusions and bring together the threads from individual chapters.

ACKNOWLEDGEMENTS

This thesis represents a confluence of ideas, learning process, resilience, and support from innumerable people, whom I am deeply grateful for helping with my research and supporting me through challenging moments in this important step in my life.

Firstly, I would like to express my sincere gratitude to Richard Smith, my supervisor, for the continuous support of my Ph.D. study and research. His advice helped me in all the time of research and writing of this thesis. Besides his active guidance, the way he integrates teaching and research has been an inspiration to me.

Secondly, I would like to thank the advisory committee members: Alan King and Harold Gibson. Their suggestions were crucial to extract the maximum benefit out of my research.

I would like to thank Mostafa Naghizadeh for sharing his knowledge of seismic and other geophysical methods.

I also would like to thank the Metal Earth project at Laurentian University for funding my research as well as providing gravity, seismic and petrophysical data.

I owe much to Metal Earth research fellows Rajesh Vayavur and Esmail Eshaghi for helping me in uncountable moments and also taking their time and engaging in useful discussions. I don't have words to express my gratitude to Rasmus Nielsen Haugaard for not only assisting me to better understand the geology in the Matheson area, but also for helping to estimate the density of rocks in the study area. I also have to thank Ademola

Adetunji, Saeid Cheraghi, and Gaëtan Launay for providing suggestions for my research as well as sharing their experience.

The geophysics crew: Hussein, Francisca, Eric, Elton, Cristopher, Anthony, Tomas, Robert, Amir, and William. Students like me, with whom not only knowledge and skills have been shared, but also frustration, excitement as well as dreams. It has been an honour to be part of this group.

A special thanks to the Metal Earth staff. Natalie for being always empathetic with the student's problems, and for being more than willing to help no matter what was the issue. I have an immense gratitude to Bryona, Dean, Brandon, and Courtney for making my life easier during the 2018 and 2019 field seasons by providing assistance. I am also very grateful to Kipp for resolving any problem and for predicting and helping me avoid IT issues.

I am grateful for assistance from Glenn Pears, who helped me whenever I had questions or problems using the GoCad/VPmg software.

A special thanks to Seequent, Mira Geoscience Ltd., and Emerson Paradigm for providing specialized software.

I am deeply grateful to my wife, Janaina, who has sacrificed her own career and has taken any job, regardless of their inherent challenges and difficulties, to support our family while I was pursuing a dream. I love you so much.

I also have to thank my two kids, Lorenzo and Caterina, for understanding when I couldn't play and have fun with them due to the demanding load that sometimes a Ph.D. research requires.

A special thanks to my parents in law, Silvia and Luiz Henrique, for supporting my wife's and my choices. I am also deeply grateful for them coming to Canada to help take care of my kids when I was in the field.

I also would like to thank my parents, Tereza and Antonio, for supporting me financially and emotionally in my studies whenever I needed them.

TABLE OF CONTENTS

CHAPTER 1: INTRODUCTION TO THE THESIS	1
1.1. Introduction	1
CHAPTER 2: GRAVITY DATA AND GRAVITY DATA REDUCTIONS	5
2.1. Gravity Acquisition	5
2.2. Gravity Reduction	7
2.2.1. Tidal Effect	7
2.2.2. Residual Instrument Drift	8
2.2.3. Latitude Correction	8
2.2.4. Ellipsoidal to Geoidal Height Conversion	9
2.2.5. Free-air Correction	10
2.2.6. Simple Bouguer Correction	10
2.2.7. Terrain Correction	11
CHAPTER 3: ERROR ANALYSIS OF THE GRAVITY DATA AND PORCUPINE-DESTOR FAULT DIP UNCERTAINTIES	14
3.1. Error Analysis of the Gravity Data	14
3.1.1. Error Estimation via Error Propagation Equation	17
3.1.1.1. Gravity Meter Readings Error	18
3.1.1.2. Latitude Correction	21
3.1.1.3. Free-air Correction Error	22
3.1.1.4. Simple Bouguer Correction Error	24
3.1.1.5. Terrain Correction Error	26
3.1.2. Error Estimation via Repeated Measurements Comparison	29
3.2. Porcupine-Destor Fault Dip Estimation	36
3.2.1. Forward Modeling	38
3.2.1.1. The Gravity Anomaly due to a Polygon	39
3.2.2. PDF Dip Estimation - Constraint A: Density Compilation	40
3.2.3. PDF Dip Estimation - Constraint B: High Resolution Seismic Sections	43
3.2.4. PDF Dip Estimation: Gravity Data	46
3.2.5. PDF Dip Estimation: Contaminating the Data with Random Noise Normally Distributed	50
3.2.6. PDF Dip Angles at Matheson Area	57
3.2.7. The Importance of Gravity Data Error estimation	59
3.2.8. The implications for Gravity Survey Planning and Specifications	62
CHAPTER 4: DETERMINING THE VARIATION IN THE DIP OF THE STRUCTURE BOUNDING A SUCCESSOR BASIN	63
4.1. Geology	63

4.2. Model Constraints	65
4.2.1. Petrophysical Data and Surface Geology Map	65
4.2.2. High Resolution Seismic Sections	71
4.3. Gravity and Magnetic Data	73
4.3.1. Gravity Data	73
4.3.2. Magnetic Data	77
4.4. Forward Modeling	80
4.4.1. Shillington Line Model (Profile A)	82
4.4.2. Val Gagné Line Model (Profile B)	84
4.4.3. Watabeag Traverse Model (Profile C)	86
4.4.4. Matheson Traverse Model (Profile D)	88
4.4.5. 3D Visualization of the Models	91
4.5. Conclusions from the PASA profile models	92
CHAPTER 5: 3D GRAVITY INVERSION OF THE MATHESON AREA	95
5.1. Geology of the MSA	97
5.2. Density Properties	100
5.3. Gravity Data	106
5.4. 3D Unconstrained to Constrained Inversions of the MSA Gravity Data.	108
5.4.1. Inverse Modeling	110
5.4.2. Unconstrained Gravity Inversion	113
5.4.3. Constrained Gravity Inversion I: Resolving the Source's Location for the Porcupine assemblage	120
5.4.4. Constrained Gravity inversion II: Resolving the Source's Location and Solving the Density Problem for the Porcupine Assemblage	127
5.4.5. Constrained Gravity inversion III: Resolving the Density Problem, the Source's Location, and the Source's Geometry for All Units – Geometry Inversion	131
5.4.5.1. 3D Geometry Inversion: Constraining the Surface Geology and Density Properties.	132
5.4.5.2. 3D Geometry Inversion: Maintaining the Contacts of the Porcupine Assemblage Fixed During the Inversion for Obtaining Superior Results	135
5.4.5.3. 3D Carr Intrusion Geometry Inversion	139
5.4.5.4. 3D Porcupine Assemblage Starting Model	143
5.4.5.5. Maintaining the Contacts of the Porcupine Assemblage and Carr Intrusion Fixed During the Inversion	144
5.5. Conclusions	151
CHAPTER 6: DELORO ASSEMBLAGE HYPOTHESES	156
6.1. 2D Models	158
6.2 Homogeneous 3D Models	163

6.3. 3D Heterogeneous Models -----	167
6.3.1. Model αS (Heterogeneous)-----	168
6.3.2. Model βS (Heterogeneous)-----	170
6.4. Model Comparison -----	173
6.5. Discussion and Conclusions -----	176
7. THESIS CONCLUSIONS -----	178
REFERENCES -----	183

LIST OF FIGURES

<i>Figure 2.1. i), Elevation map of the Matheson area showing the gravity stations (black dots) and the CGSN gravity station (red triangle), to which the survey measurements were tied. ii) a photography of the Scintrex CG-6 Autograv™ gravity meter on the tripod on the right, and the Trimble R2 receiver on the orange traffic cone on the left.</i>	6
<i>Figure 2.2. Representation of the intermediate zone correction. This step in the terrain correction computes the topography effect of the eight closest cells immediately surrounding cell 0 (at the gravity station).</i>	13
<i>Figure 3.1. Matheson Metal Earth gravity station location (gray dots) and the repeat gravity stations (blue squares) overlaying the geology. In total 242 gravity stations were acquired in this area and 31 of these were reoccupied twice as repeat measurements.</i>	19
<i>Figure 3.2. Histogram of the differences between gravity readings (g_{RiGSj}) and the average (μ_{gRGSj}) obtained for a specific gravity station.</i>	21
<i>Figure 3.3. Histogram of the differences between latitude readings (ϕ_{iGSj}) and the average obtained ($\mu_{\phi GSj}$) for a specific gravity station.</i>	22
<i>Figure 3.4. Histogram of the differences between GNSS elevation readings (Sh_{iGSj}) and the average obtained (μ_{ShGSj}) for a specific gravity station.</i>	24
<i>Figure 3.5. (i) Metal Earth Sudbury transect gravity stations and Lake Wanapitei with its bathymetry shown in color. The closest gravity stations have been selected to assess the effect of the lake on the gravity measurements (ii and iii). Bathymetry source: Land Information Ontario Database (10 m accuracy).</i>	28
<i>Figure 3.6. Histogram of the differences between the free-Air anomaly reduced data point (FA_{iGSj}) and the average obtained (μ_{FAGSj}) for the relevant gravity station.</i>	30
<i>Figure 3.7. Histogram of the differences between the simple Bouguer anomaly reduced data point (SB_{iGSj}) and the average obtained (μ_{SBGSj}) for the relevant gravity station.</i>	31
<i>Figure 3.8. Histogram of the differences between the complete Bouguer reduced data point (CB_{iGSj}) and the average obtained (μ_{CBGSj}) for the relevant gravity station.</i>	32
<i>Figure 3.9. Porcupine-Destor fault (black dashed lines) and the surrounding geology (Ayer et al., 2005).</i>	37
<i>Figure 3.10. Rock-density estimation apparatus, shown when weighting a rock sample submerged in water.</i>	41

Figure 3.11. Spatial distribution of the density samples compiled to constrain the model. Some symbol location might represent more than one sample, either on an outcrop or in a borehole. ----- 42

Figure 3.12. Histogram of the estimated density values of the Porcupine assemblage indicating its density mean ($\mu\rho_{Porc}$) and the standard deviation ($\sigma\rho_{Porc}$). ----- 42

Figure 3.13. Histogram of the estimated density values of the Lower Tisdale assemblage indicating its density mean ($\mu\rho_{LT}$) and the standard deviation ($\sigma\rho_{LT}$). ----- 43

Figure 3.14. Val Gagne (i) Watabeag (ii) and Matheson (iii) interpreted seismic sections. The green dashed line indicates strong reflectors interpreted as the bottom of the Porcupine assemblage, but this gradually weakens to the south, so the location where it ends is not clear. The PDF, marked with a black dashed line is not a strong reflector, nor does it show coherent truncation, hence the location of the PDF is uncertain. The figure has a question mark, which indicates that the PDF dip angle is to be estimated. ----- 45

Figure 3.15. ME and CGDB gravity stations location in the study area. ----- 46

Figure 3.16. Complete Bouguer anomaly map, generated using a compilation of the ME and CGDB data, overlaid by the Porcupine-Destor fault and the ME selected gravity stations. ----- 48

Figure 3.17 Geology map overlaid by the Porcupine-Destor fault and the ME selected gravity stations. ----- 48

Figure 3.18. Focussed complete Bouguer anomaly gravity profiles along the Val Gagne (B), Watabeag (C) and Matheson (D) profiles. ----- 49

Figure 3.19. Four Matheson profile datasets after contamination with noise with uncertainty 0.121 mGal (i) and one of these datasets ('n') is compared to the predicted data (ii). Panel iii shows the misfit between the contaminated data and the data predicted for the model revealed in iv that has a dip of 45°. ----- 51

Figure 3.20. Misfit as function of the PDF dip angles in the Matheson profile for three different contaminated data sets. ----- 52

Figure 3.21. Histogram of the estimated dip angles for the Porcupine-Destor fault below the Val Gagne profile (B) as estimated from ensembles of noise-contaminated gravity data. ----- 55

Figure 3.22. Histogram of the estimated dip angles for the Porcupine-Destor fault below the Watabeag profile (C) as estimated from ensembles of noise-contaminated gravity data. ----- 56

Figure 3.23. Histogram of the estimated dip angles for the Porcupine-Destor fault below the Matheson profile (D) profile as estimated from ensembles of noise-contaminated gravity data. ----- 56

Figure 3.24. Porcupine-Destor fault estimated dip at Val Gagne (B), Watabeag (C), and Matheson (D) profiles. ---- 57

Figure 3.25. The estimated dip of the Porcupine-Destor fault and the corresponding uncertainty (one standard deviation is shown by the orange triangle) at the Val Gagne (B), Watabeag (C), and Matheson (D) profiles presented as cross sections (no vertical exaggeration).----- 58

Figure 3.26. 3D visualization of the computed 2D models imaging of the PDF fault dip along the strike direction. -- 59

Figure 3.27 Porcupine-Destor fault dip (dashed line) and dip error standard deviation (orange zone) estimation for the Matheson profile. In this case, the estimation process was repeated with the noise ensembles for the measured gravity given a standard deviation of 1 mGal, a value typical for regional compilations. ----- 61

Figure 4.1. The location of the Abitibi greenstone belt on the Ontario and Quebec map on the right and the geological map of the study area on the left. The black lines are the location of seismic transects where the gravity data have been modeled (A - Shillington line, B - Val Gagné line, C – Watabeag line, and D – Matheson line). The Porcupine-Destor (PDF) and Pipestone (PSF) faults are shown with red and blue dashed lines respectively. (Modified after Montsion et al., 2018).----- 64

Figure 4.2. Simplified surface geology map (modified after Ayer, 2005), using slightly different colors than Figure 4.1. Also shown are the locations of samples with associated density measurements. Different location symbols are used for each geological unit, as shown in the legend. Some symbols might be indicating the location of more than one sample. ----- 66

Figure 4.3. Histogram of the measured density values of the upper part of the Tisdale assemblage with the mean ($\mu\rho_{UT}$) and the standard deviation ($\sigma\rho_{UT}$) on the top left of the figure. ----- 68

Figure 4.4. Histogram of the measured density values of the Carr intrusion, with the mean ($\mu\rho_{Carr}$) and the standard deviation ($\sigma\rho_{Carr}$) shown top left. ----- 69

Figure 4.5. Histogram of the measured density values of the Kidd-Munro assemblage, with the estimated mean ($\mu\rho_{KM}$) and standard deviation ($\sigma\rho_{KM}$) shown in the top left. ----- 70

Figure 4.6. Seismic sections to guide construction of the density model for traverses A (Shillington line), B (Val Gagné Line), C (Watabeag line), and D (Matheson Line). On the top of the seismic sections, the color indicates the surface geology using the legend of Figure 4.2. ----- 72

Figure 4.7. Location of the seismic lines, the sections from which are shown in Figure 4.6, overlain on the simplified geology. For the color legend, see Figure 4.2. ----- 73

Figure 4.8. Gravity grids and the four profile traverses (A to D). On the left (i), the complete Bouguer anomaly map is displayed as a color image, while on the right (ii) it is shown as a qualitative transparent greyscale image with the geology map underneath. The data was obtained for the Metal Earth project and from the Canadian Gravity Database compilation. ----- 75

Figure 4.9. Gravity station locations, showing ME data (in blue) and CGDB data (in black), overlaying the surface geology map in the PASA. The locations inside the brown rectangles are the gravity stations, which were used when modeling the data. ----- 76

Figure 4.10. Total magnetic intensity (TMI) grid of the PASA. The left is a color image, with the lows cool (blue) colors and the highs hot (red). On the right, the surface geology map is overlaid by the first vertical derivative of the TMI grid, strong negatives red and strong positives black. The data was obtained from the two Ontario Geological Survey data sets mentioned in the text. ----- 78

Figure 4.11. Interpreted dikes from the magnetic grid based on Berger (2010). The magnetic grid and geological map are the same as those shown in Figure 4.10-ii. ----- 80

Figure 4.12. Location of the forward-modeling profiles highlighting the locations of the seismic sections (blue with white infill). While in C and D the seismic lines entirely cover the model lengths, in A and B there is only partial coverage. ----- 82

Figure 4.13. The Shillington line modeling showing the measured and predicted gravity data and the difference between these (red line) (i), the geological model with the units indicated by the color legend at the bottom of the figure and the modeled fault localizations shown with dashed lines (ii), which are also shown in green on the interpreted seismic section (iii). ----- 83

Figure 4.14. The 3D visualization of the Shillington line model (profile A), also shown in 2D in Figure 4.13-ii. The first vertical derivative of TMI, which is overlaying the surface geology, is displayed on the top to highlight the dikes at the surface. ----- 84

Figure 4.15. The Val Gagné line modeling showing the measured and predicted gravity data and the difference (red line) (i), the model itself showing the lithologies (colors are shown on the legend at the bottom of the figure) and the modeled fault localizations are shown with dashed lines (ii), and the interpreted seismic section (iii). ----- 85

Figure 4.16. The 3D visualization of the Val Gagné line (profile B) model also shown in 2D in Figure 4.15-ii. The first vertical derivative of TMI, which is overlaying the surface geology, is displayed on the top to highlight the dikes at the surface. ----- 86

Figure 4.17. The Watabeag line modeling showing the measured and predicted gravity data and the difference (red line) (i), the model itself (with the lithologies indicated by the colors shown in the legend at the base of the figure) and the modeled PDF fault location is shown with the dashed line (ii), and the interpreted seismic section (iii). ----- 87

Figure 4.18. The 3D visualization of the Watabeag line model (profile C) also shown in 2D in Figure 4.17-ii. The first vertical derivative of TMI, which is overlaying the surface geology, is displayed on the top to highlight the dikes at the surface.----- 88

Figure 4.19. The Matheson line modeling showing the measured and predicted gravity data and the difference (red line) (i), the model itself (with the lithologies indicated by the colors shown in the legend at the base of the figure) and the modeled fault localizations shown with the dashed lines (ii), and the interpreted seismic section (iii). ----- 90

Figure 4.20. The 3D visualization of the Matheson line model (profile D) also shown in 2D in Figure 4.19-ii. The first vertical derivative of TMI, which is overlaying the surface geology, is displayed on the top to highlight the dikes at the surface.----- 91

Figure 4.21. The 3D view of the parallel 2D models referred to the Shillington line (section A), the Val Gagné line (Section B), the Watabeag line (Section C), and the Matheson line (Section D). ----- 92

Figure 5.1. Simplified surface geology map showing the full extent of the Matheson Study Area or MSA (modified after Ayer, 2005). The area delimited by the dashed rectangle refers to the PASA described in Chapter 4. The blue line represents the location of the low-resolution Matheson seismic line (R1). ----- 97

Figure 5.2. The study area location map on the top-left (i), the geological map (modified after Ayer et al., 2005) of the Matheson area on the right (ii). The legend for the geological map is shown in stratigraphic order, with the youngest at the top. ----- 99

Figure 5.3. Location of samples that have associated density measurements for the geologic units that are in the MSA, but not the PASA (which have already been described in Chapter 4). Different location symbols are used for each geological unit, as shown in the legend. Some symbols might be indicating the location of more than one sample. ----- 101

Figure 5.4. Histogram of the measured density values of the Sthoughton-Roquemaure assemblage with the mean ($\mu\rho_{SR}$) and the standard deviation ($\sigma\rho_{SR}$) on the top left of the figure. ----- 102

Figure 5.5. Histogram of the measured density values of the Blake River assemblage with the mean ($\mu\rho_{BR}$) and the standard deviation ($\sigma\rho_{BR}$) on the top left of the figure. ----- 103

Figure 5.6. Histogram of the measured density values of the Watabeag Lake intrusion with the mean ($\mu\rho_{WB}$) and the standard deviation ($\sigma\rho_{WB}$) on the top left of the figure. ----- 103

Figure 5.7. Histogram of the measured density values of the Huronian supergroup with the mean ($\mu\rho_{HC}$) and the standard deviation ($\sigma\rho_{HC}$) on the top left of the figure. ----- 104

Figure 5.8. Graph showing the density measurements: mean (black circles), and standard deviation from the mean (blue bars) for each geological unit. ----- 105

Figure 5.9. The gravity stations location (on the left), where blue circles refer to the ME data, and the black diamonds represent the CGDB data. On the right the estimated minimum spacing of the gravity stations. ----- 106

Figure 5.10. Complete Bouguer anomaly gravity grid on the right and the surface geology for the MSA (left). The gravity data was obtained from the Metal Earth project and the Canadian gravity data compilation. For the geological legend, see Figure 5.2. The grid cell spacing is 100 m, whereas the gravity station spacing can vary up to 2 km or more in some locations. ----- 107

Figure 5.11. R1 Matheson seismic line section shown in perspective and overlaid by the MSA surface geology (i) and below as a function of two-way travel time (ii). On both views the main reflectors, a, b and c are marked. -- 109

Figure 5.12. Free-air anomaly gravity grid in the MSA. The data was obtained from the Metal Earth project and the Canadian gravity data compilation (CGDB). ----- 114

Figure 5.13. RMS misfit as a function of the iteration number for the unconstrained inversion (Unc). The maximum number of iterations and the achieved misfit are shown on the top right of the figure. ----- 116

Figure 5.14. Observed data grid (i), calculated data grid (ii), and the residual data grid (iii) computed from the unconstrained inverse model shown in Figure 5.15. ----- 116

Figure 5.15. S-N vertical and horizontal sections of the unconstrained inverse model overlaid by the surface geology map (i and iii). They represent the same model differing solely by the color palette (ii and iv). In iii the feature associated with the Porcupine assemblage is highlighted by the dashed square. ----- 117

Figure 5.16. Zoomed in view of the unconstrained model. The dashed rectangle (i) highlights the feature that might be associated with Porcupine assemblage. The color bar is shown in panel (ii) and the smaller dashed rectangle on the color bar (iii) shows that the light grey densities that have been associated with the Porcupine (2.65 to 2.67 g/cm³).----- 119

Figure 5.17. Histogram of the inverted density values from the unconstrained model. The X axis displays the density values, while in the Y axis shows the frequency of the density values.----- 119

Figure 5.18. S-N vertical and horizontal sections of the depth-weighted or slightly constrained smoothed inverse model overlaid by the surface geology map (i and iii). The vertical section is at the location of the Shillington transect. The model is the same, but different color palette (ii and iv) are used for i and iii respectively. ----- 123

Figure 5.19. Histogram of the inverted density values from the depth-weighted or slightly constrained model. The X axis is the density values, while the Y axis is the frequency of the density values. ----- 124

Figure 5.20. Zoomed unconstrained model highlighting the feature that might be associated with the Porcupine assemblage (i) with the corresponding density values (iii) shown in the color legend (ii). The vertical section is at the location of the Shillington transect. ----- 125

Figure 5.21. Zoomed view of the unconstrained model highlighting the feature that might be associated with the Porcupine assemblage, in this case the vertical section corresponds to the Matheson transect, which is further towards the east and the Porcupine assemblage is thinner, in agreement with other studies (i). The color legend is shown in (ii), with the range of density values for the Porcupine shown in the dashed rectangle (iii). ----- 126

Figure 5.22. S-N vertical and horizontal sections of the depth-weightened smoothed inversion model after the density has been incremented by 0.1 g/cm^3 . The vertical section for Matheson is displayed below the surface geology map (i and iii). The model is the same as that in Figure 5.21, differing solely by the color palette (ii and iv). ----- 128

Figure 5.23. Histogram of the inverted density values with a more dense initial guess and depth-weighting and smoothing applied to the inversion model. The X axis is the density, while in the Y axis is the frequency at each density. ----- 129

Figure 5.24. Zoomed view of the adjusted density model applied to the depth-weightened smoothed inverse model highlighting the feature that might be associated with the Porcupine assemblage (i) and the corresponding density values (iii) in the color legend (ii). The vertical section is for the Matheson transect. ----- 130

Figure 5.25. Starting density model (Model GIA) and its assigned density values associated with the assemblages and intrusions overlaid by the surface geology map (i) and the density model color legend (ii). ----- 133

Figure 5.26. RMS misfit as a function of the iteration number for the Geometry Inversion A (GIA). The maximum number of iterations and the achieved misfit is shown on the top right of the figure. ----- 134

Figure 5.27. Final density model obtained from the geometry inversion A (i) and the color legend bar (ii). ----- 134

Figure 5.28. The Section E modeling showing the measured and predicted gravity data and the difference (red line) (i). The model itself providing faults localizations and the depth of the Porcupine assemblage (ii). ----- 136

Figure 5.29. The Section F modeling showing the measured and predicted gravity data and the difference (red line) (i). The model itself providing faults localizations and the depth of the Porcupine assemblage (ii). ----- 136

Figure 5.30. The Section G modeling showing the measured and predicted gravity data and the difference (red line) (i). The model itself providing faults localizations and the depth of the Porcupine assemblage (ii). ----- 137

Figure 5.31. The locations of the cross sections of the Porcupine assemblage (i) and the 2D models on these sections distinguishing between the sections where the 2D modeling could benefit from available high-resolution seismic sections (darker green) and those where they could not (lighter green) (ii). At the bottom (iii), the created 3-D surface from the cross sections (i). The hole in the Porcupine between section C and D is the Carr intrusion. ----- 138

Figure 5.32. Gravity stations location in the CAI (ii) and in the larger model (i), which CAI was incised from. ----- 140

Figure 5.33. 3D CAI initial model (i) and the legend of the geological units (ii). ----- 140

Figure 5.34. 3D CAI model embedded by a S-N cross-section of the larger model (i) and the legend of the geological units (ii). ----- 141

Figure 5.35. RMS misfit as a function of the number of iterations for the geometry inversion of the Carr intrusion. The number of iterations and the achieved misfit on the top right of the figure. ----- 142

Figure 5.36. Starting (i) and final model (ii) computed for the Carr intrusion. ----- 142

Figure 5.37. Observed data grid (i), calculated data grid (ii), and the residual data grid (iii) computed from the Carr intrusion geometry inverse model. ----- 143

Figure 5.38. Modified starting density model and the assigned density values associated with the assemblages and intrusions overlaid by the surface geology map (i). The density model color legend is in the inset (ii). The Carr intrusion is not shown, being further to the east than this section. ----- 144

Figure 5.39. RMS misfit as a function of the number iterations for the geometry inversion B. The maximum number of iterations and the achieved misfit are shown on the top right of the figure. ----- 145

Figure 5.40. Final density model (i) obtained by maintaining the Porcupine assemblage and Carr intrusion contacts fixed during the inversion. Label (ii) highlights the density color legend bar. ----- 145

Figure 5.41. Final geological model (i) associated with the density model shown in Figure 5.39. In ii is displayed the geology legend. ----- 146

Figure 5.42. RMS misfit as a function of the algorithm iterations for the geometry inversion BS (GIBS). The maximum number of iterations and the achieved misfit on the top right of the figure. ----- 147

Figure 5.43. Final density model GIBS (i) and the density color legend bar (ii). ----- 147

Figure 5.44. Observed data grid (i), calculated data grid (ii), and the residual data grid (iii) computed from the final density model BS. ----- 149

Figure 5.45. Smaller area (ii) selected from the MSA (i) to illustrate in greater detail the topographic effect in the calculated data grid (iii) in places where there are rapid change in the topography (for example the lows shown with green arrows) . On the topographic map (iv), this corresponds to the location of the incised valley marked with the dashed white line. Note as well that the gravity stations (inverted triangles) are sparser than the topographic variations. For comparison, panel (vi) shows the observed data grid, which is similar in wavelength to panel (v), which shows the calculated data (iii), but only sampled at the gravity station locations (inverted triangles). ----- 149

Figure 5.46. Observed data grid (i), calculated data grid (ii), and the residual data grid (iii) computed from the final density model GIBS when the gravity data are gridded from data only at sampled at the gravity station locations. ----- 150

Figure 6.1. View from below looking NW to the high-resolution (R2) seismic sections overlaid by the surface geology map. The deeper reflections are identified on the seismic sections (SR3, SR5, SR7, and SR9).----- 157

Figure 6.2. Histogram of the measured density values of the Deloro assemblage with the mean ($\mu\rho_{Del}$) and the standard deviation ($\sigma\rho_{Del}$) given in the top left of the figure. ----- 158

Figure 6.3. Section A model with the Deloro included. The measured and predicted gravity data and the difference (red line) (i). The modified model showing faults localizations and seismic reflections – SR (ii). ----- 159

Figure 6.4. Section B model with the Deloro included. The measured and predicted gravity data and the difference (red line) (i). The modified model showing faults localizations and seismic reflections – SR (ii). ----- 159

Figure 6.5. Section C model with the Deloro included. The measured and predicted gravity data and the difference (red line) (i). The modified model showing faults localizations and seismic reflections – SR (ii). ----- 160

Figure 6.6. Section D model with the Deloro included. The measured and predicted gravity data and the difference (red line) (i). The modified model showing faults localizations and seismic reflections – SR (ii). ----- 160

Figure 6.7. High-resolution seismic-section interpretation indicating the seismic reflections (SR) used in the modeling. ----- 161

Figure 6.8. 3D models generated from the 2D modeling sections. On the left (i) Model α and on the right Model β (ii). Both models are viewed from the southeast. ----- 163

Figure 6.9. 3D models highlighting the Porcupine and Deloro assemblages generated from the 2D modeling sections. On the left (i) the Porcupine assemblage in Model α , and on the right the Porcupine assemblage and the Deloro in Model β . The geological legend is shown on the bottom and the view is from the southwest. ----- 164

Figure 6.10. Observed data grid (i), calculated data grid (ii), and the residual data grid (iv) from the forward modeling of Model α . In iii and v the calculated data grid and residual data are computed solely at the gravity station (denoted GS). ----- 165

Figure 6.11. Observed data grid (i), calculated data grid (ii), and the residual data grid (iv) from the forward modeling Model β . In panels (iii) and (v) the calculated data grid and residual data are computed solely at the gravity station (denoted GS). ----- 166

Figure 6.12. The predicted data for models α (i) and β (ii) and the grid difference (iii) between these two grids. -- 166

Figure 6.13. RMS misfit as a function of the number of iterations to compute the smoothed Model αS . The maximum number of iterations and the achieved misfit are on the top right of the figure. ----- 168

Figure 6.14. Model αS . Panel (iii) shows the volume classified as Porcupine assemblage and panel (i) shows the density variation in this assemblage and within a north-south section. Panel (iv) is the volume designated as the Lower Tisdale (light green) and Kidd-Munro (dark green) assemblages. Panel (iii) is the density variations within these two assemblages. ----- 169

Figure 6.15. Observed data grid (i), calculated data grid (ii), and the residual data grid (iv) from Model αS . In panels (iii) and (v) the calculated data grid and residual data grids are computed solely at the gravity stations (denoted GS). ----- 170

Figure 6.16. RMS misfit as a function of the number of iterations while inverting to obtain the smoothed Model βS . The maximum number of iterations and the achieved misfit are displayed on the top right of the figure. ----- 171

Figure 6.17. Model βS . Panel (iii) shows the volume classified as Porcupine assemblage and panel (i) shows the density variation in this assemblage and within a north-south section. Panel (iv) is the volume designated as the Lower Tisdale (light green) Kidd-Munro (dark green) and Deloro (brown) assemblages. Panel (iii) is the density variations within these three assemblages. ----- 172

Figure 6.18. Observed data grid (i), calculated data grid (ii), and the residual data grid (iv) from the Model βS . In panels (iii) and (v) the calculated data grid and residual data grids are computed solely at the gravity stations (denoted GS). ----- 173

Figure 6.19. Porcupine assemblage 3D models comparison looking NE (i) and looking NW (ii). The red material is what must be added to Model β in order to make Model α . ----- 175

LIST OF TABLES

<i>Table 3.1. Error estimations comparison obtained from two different methodologies.....</i>	<i>33</i>
<i>Table 3.2 – Estimated PDF dip angles for Val Gagne (B), Watabeag (C), and Matheson (D) transects.</i>	<i>54</i>
<i>Table 4.1. Data summarizing the density measurements: the mean, standard deviation from the mean, as well as the number of samples.</i>	<i>71</i>
<i>Table 4.2. Comparison of fault dips from Chapter 3 and this chapter.</i>	<i>93</i>
<i>Table 5.1 - Data summarizing the density measurements: mean, standard deviation from the mean, as well as the number of samples. Including those already reported in Chapter 4.</i>	<i>105</i>
<i>Table 5.2 – Table of results showing the misfit and characteristics for each of the models.....</i>	<i>154</i>
<i>Table 6.1 – Seismic interpretation comparison between the original interpretation and by including the Deloro assemblage.</i>	<i>162</i>
<i>Table 6.2 – Density variation statistics for the computed models.</i>	<i>174</i>
<i>Table 6.3. Comparison of estimated PDF dip angles.</i>	<i>176</i>

Chapter 1: Introduction to the Thesis

1.1. Introduction

A well-established consensus is that models obtained from potential-field data, when not constrained by other sources of data, are deemed non-unique; that is, there are an infinite number of density or magnetism distributions in the subsurface that can reproduce the observed anomalies (Dentith and Mudge, 2014). In order to reduce the non-uniqueness characteristic of potential-field data, constraints are incorporated into the model, such as petrophysics, data from seismic surveys and geological maps. The goal is to reduce the number of models that can explain the data and to select the model that best explains the anomalies. It is expected that for a successful model the petrophysical parameters of the model are resolved as well as the geometry and the depth of the anomaly sources. There are innumerable studies in the literature that demonstrate the benefits of constraining gravity or magnetic models (e.g. Kamm et al., 2015; Mahmoodi et al., 2017, Sun et al., 2019; Vallée et al., 2019; Eshaghi et al., 2020). However, these studies commonly do not demonstrate the individual improvements that result as a consequence of incorporating each constraint into the geophysical model.

This study will demonstrate how the model, either inverse or forward, is improved as new constraints are incorporated into the modeling workflow. These constraints include data from a density compilation, high-resolution seismic sections, geological maps as well as geological interpretations.

When modeling geophysical data, the petrophysical model is adjusted to have a geophysical response that is as close as possible to the measured data. Hence, the measured data is a constraint that the model must also satisfy. When undertaking the modeling process, it is necessary to decide how close the model data must be to the measured data. Normal scientific practice is to adjust the model data so that it agrees to within the experimental error of the measured data, that is, it is within one or two standard deviations of the mean. Hence, it is important to know the mean and standard deviation of the measured data. However, for gravity data, the model data cannot be compared directly with the data measured by the gravimeter, the measured data must first be corrected so that it is in the same form as the model data. As these corrections are applied to the data, they change the means and standard deviations of the measured data. Chapter 2 describes in detail the corrections that are applied to reduce the data from the raw measurement to the data that can be compared with the model data.

In Chapter 3, an error propagation analysis of the Metal Earth (ME) gravity data is undertaken to determine how the errors change as the data is reduced. Such an analysis is not available in the literature. This is not always straightforward for some of the more numerical reduction steps, like terrain correction, so an upper estimate of the error from this step by estimated using the error associated with not accounting for a large terrain feature. This error-propagation estimate is comparable with the errors estimated from a second procedure that reduced multiple repeat measurements and then calculated the mean and standard deviation of these measurements. Once these errors in the reduced data are known, an innovative new methodology was employed to estimate an error in a petrophysical model parameter, the dip of the Porcupine-Destor fault (PDF). In this

modeling, it was assumed that the geometry of the model was two-dimensional (did not vary in the strike direction, but only in the depth and profile directions) and that the PDF was a simple linear fault. Information from seismic sections, the density property compilation and the bedrock geological map were also used as constraints to ensure that the two-dimensional (2D) model is realistic.

While Chapter 3 was primarily focussed on estimating the error in one parameter, the dip of the PDF, in Chapter 4, the modeling was expanded to model a longer profile and used to estimate other parameters. For example, the linear fault was divided into a number of piecemeal linear sections and the thickness of the Porcupine assemblage was also adjusted, as was the dip and shape of the PSF. These changes made it impractical to estimate errors on the derived model parameters, as it would have been too laborious. The magnetic data was also interpreted, which was most useful for interpreting the magnetic dikes, as these are the strongest magnetic features in the Matheson study area (MSA). The 2D modeling was undertaken on a number of sections and this was useful for understanding how the model changes along strike.

The 2D models derived in Chapter 4 were used to build a three-dimensional (3D) model, which is the focus of Chapter 5. This chapter illustrates how gradually adding constraints results in a model that progressively becomes more consistent with the geological and geophysical information. In most of the models, the model data is within one or two standard deviations of the reduced data, so the gravity-data constraint is always satisfied. The application of the other constraints results in a more realistic model.

Generally, small changes in the parameters of the near-surface rocks have a greater impact on the gravity data than comparable changes to deeper rocks. Thus, it is

normally possible to fit the data by changing parameters of the near-surface rocks. This means that using gravity data to explain deeper features is more difficult. A good example of this is provided in Chapter 6, where a seismic reflection at a depth of about 7 km on some profiles was interpreted by Haugaard et al. (2021) as being caused by the top of the Deloro assemblage. The 3D models in Chapter 5 are able to adequately explain the gravity data without the top of the Deloro being the source of this seismic reflector. Adding the Deloro at the depths suggested on the seismic sections resulted in a misfit in the gravity data. The inversion will adjust the parameters of the near-surface rocks to remove this misfit and not the parameters of the deeper Deloro material. Hence, the inversions cannot be used to adjust the depth to the Deloro at other locations. To determine the depth to the Deloro at other locations requires that the 2D modeling be redone by revising the near-surface material on the section where there are seismic constraints. Secondly, the parameters of the near-surface rocks are fixed and only the depth of the Deloro is allowed to change. Using this methodology, the depth to the Deloro changed in the Matheson area, getting shallower to the west. This is consistent with the geological map, which shows it outcropping further to the west.

Chapter 2: Gravity Data and Gravity Data Reductions

2.1. Gravity Acquisition

Gravity data collected along the Matheson traverses for the Metal Earth (ME) project were used for this study. All ME gravity readings were taken using Scintrex CG-6 Autograv™ gravity meters and Trimble R2 GNSS (Global Navigation Satellite System) receivers (see Figure 2.1-*ii*). The GNSS systems include the GPS, and GLONASS systems. Data collected by the Trimble R2 receiver was processed with Fieldpoint RTX software to estimate precisely the location and height of each station. The Metal Earth gravity survey stations were chosen alongside roads or within walking distance of roads with an average station-spacing of 300 m. These stations were tied to existing Canadian Gravity Station Network (CGSN) base stations. In the case of the Matheson survey, the base was station 9656-1970 on Highway 101 (located at the red triangle on Figure 2.1-*i*). As well, side road measurements with distances up to 1 km from the traverses were acquired when road access permitted (Maleki et al., 2018). The purpose of the side-road stations 1 km from the profile is to improve the quality of grids produced when this data is combined with other regional data away from the profile line. In total there were 242 (regular and side-road) gravity stations acquired along Matheson transects.

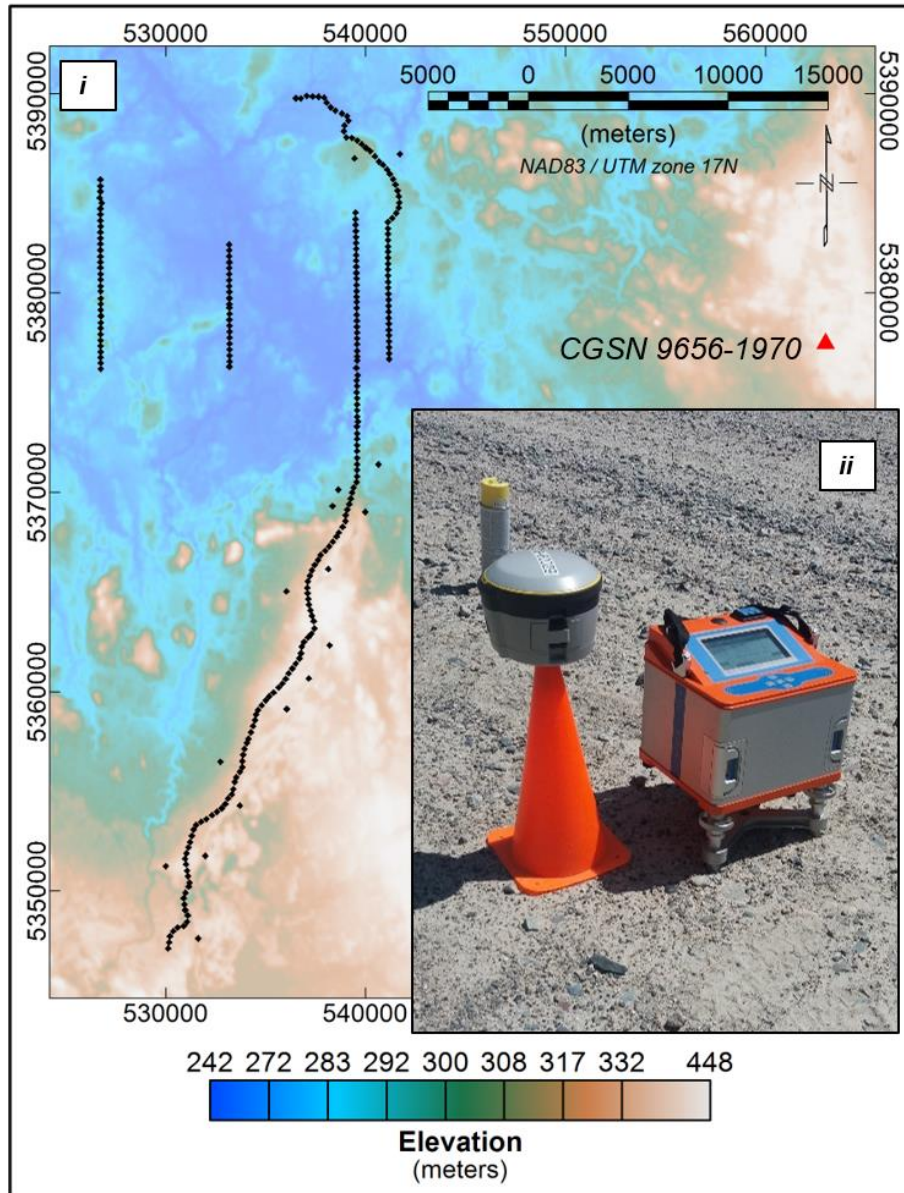


Figure 2.1. *i*), Elevation map of the Matheson area showing the gravity stations (black dots) and the CGSN gravity station (red triangle), to which the survey measurements were tied. *ii*) a photograph of the Scintrex CG-6 Autograv™ gravity meter on the tripod on the right, and the Trimble R2 receiver on the orange traffic cone on the left.

2.2. Gravity Reduction

Gravity data were processed and corrections applied to remove unwanted variations associated with changes in latitude and elevation (Dentith and Mudge, 2014). This was done to produce a final “complete Bouguer anomaly” (Nowell, 1999) or CBA. These corrections were applied using Oasis Montaj® software (<https://www.seequent.com/products-solutions/geosoft-oasis-montaj/>). The gravity-data correction process is also called gravity data reduction, and details of each correction are described below.

2.2.1. Tidal Effect

Gravity at every location varies with time owing to the gravitational attraction of the Moon, and to a lesser extent of the Sun (Dentith and Mudge, 2014). The effect is both time and latitude-dependent and never exceeds 0.3 mGal (Blakely, 1996). The Scintrex CG-6 Autograv™ gravity meter, which was used in the ME surveys, automatically removed these tidal variations. The correction used Longman’s formula (Scintrex, 2012) to compute the tidal accelerations at any given time and place on the Earth’s surface (Pollack, 1973). The CG-6 has an internal GPS to provide the time and position of each measurement as this is necessary for calculating the tidal correction (Scintrex, 2012). This internal GPS gives the location accurate enough for the tidal corrections, however the height accuracy is insufficient for the corrections below, which is why the Trimble R2 receiver and Fieldpoint RTX software was necessary. Other corrections automatically undertaken by the Scintrex CG-6 Autograv™ gravity meter include instrument tilt,

temperature and drift corrections. The drift correction is made using measurements acquired in a drift calibration test, which was undertaken prior to the survey.

2.2.2. Residual Instrument Drift

The instrument does not always drift as predicted by data acquired in the drift calibration test. These changes from the assumed drift are called the residual drift and are attributed to creep in the springs of the gravity meter and is usually gradual and unidirectional (Telford et al., 1996). This residual variation is normally corrected by taking repeated readings at a base station or a repeat station throughout the survey and assuming that the residual drift is linear between these repeated readings (Dentith and Mudge, 2014). The residual instrument drift-corrected data, denoted g_R , implicitly includes the instrument corrections for tidal effect as well as tilt and temperature variations.

2.2.3. Latitude Correction

The Earth's gravity field is stronger at the poles than the equator because of several effects. Firstly, due to centrifugal acceleration associated with the spin of the earth, the Earth's shape is roughly ellipsoidal, with the equatorial radius greater than the polar radius (Dentith and Mudge, 2014). This means that the surface of the earth at the equator is further from the centre of the earth and the gravity is less. Secondly, the centrifugal force also acts on the test mass in the gravity meter. Accounting for this equatorial bulge and the centrifugal force is done using the latitude correction (Roy,

2008). The variation in gravity, g , with latitude, ϕ , on the surface of the spheroid is known as the normal or theoretical gravity (Dentith and Mudge, 2014). It can be calculated using the international formula correction (IGFC), which is occasionally updated. The 1967 formula (equation 2.1), has been selected as the standard for the Metal Earth project,

$$IGFC(\phi) = 978031.846[1 + 0.005278895\sin^2(\phi) - 0.000023462\sin^4(\phi)], \quad (2.1)$$

$$g_{IGF} = g_R - IGFC(\phi), \quad (2.2)$$

where, g_{IGF} is the latitude corrected data after the residual instrument drift corrected gravity data, g_R , has had the theoretical latitude correction $IGFC(\phi)$ subtracted.

2.2.4. Ellipsoidal to Geoidal Height Conversion

The heights of the gravity instrument at all the measurement stations are given relative to the ellipsoidal datum World Geodetic System 1984 (WGS-84). Nevertheless, the gravity corrections are relative to the geoid (Blakely, 1996), which is the equipotential surface coinciding with mean sea level (Dentith and Mudge, 2014). Historically, this choice stems from the easy availability of the orthometric height of a point above sea level. This orthometric height is determined by levelling relative to the local horizontal (or vertical) with orthometric reductions, and is listed for all survey benchmarks and contoured on topographic maps (Jacoby and Smilde, 2009). The ME ellipsoidal heights were converted to be relative to the geoidal datum. This conversion was undertaken using the online GPS.H tool provided by the Canadian Geodetic Survey at the government of

Canada website. For this study, the geoid is the Canadian Geodetic Vertical Datum of 2013 (CGVD13).

2.2.5. Free-air Correction

Gravity measurements over land are adjusted to be an equivalent reading on the geoid using the free-air correction (*FAC*), the equation for this correction in mGal is

$$FAC = 0.3086h, \quad (2.3)$$

where h is the height in meters of the gravity station above the geoidal datum (Blakely, 1996). Including this correction gives

$$g_{FA} = g_{IGF} + FAC, \quad (2.4)$$

where g_{FA} is the gravity data after free-air reduction from the aforementioned corrections and is referred to as the gravity anomaly (Blakely, 1996).

2.2.6. Simple Bouguer Correction

The free-air correction ignores mass that may exist between the level of observation and the geoid (Blakely, 1996). However, if the gravity station is located on topography above the geoid, then the intervening layer of rock between the geoid and the station will exert a gravitational attraction that will be measured by the gravity meter (Dentith and Mudge, 2014). The Bouguer correction removes the impact of this additional mass. This correction is made assuming that there is a homogeneous, infinitely extended

slab of thickness equal to the height of the observation point above the geoid. It is called the simple Bouguer correction (*SBC*) (Blakely, 1996), and is given in mGal by

$$SBC = -0.04192\rho h, \quad (2.5)$$

where ρ is the Bouguer density in g/cm^3 , which is the average density of material in the Bouguer slab and h is the height in meters of the station above the geoidal datum level, which is also the thickness of the Bouguer slab. Applying this correction, gives

$$g_{SB} = g_{FA} + SBC, \quad (2.6)$$

where g_{SB} is known as the simple Bouguer anomaly.

2.2.7. Terrain Correction

The uniform slab assumption in the simple Bouguer correction does not account for the topographic roughness of the slab near the gravity station. Because of these topography variations, surrounding areas may have mass above the slab (hills), as well as lack of mass (valleys) in the volume occupied by the slab. Therefore, the effects of these features in the gravity data require correction. The magnitude of the correction is obtained by determining the gravitational attraction of the mass in the hills and of the mass deficiencies of the valleys. This gravitational correction is calculated using topographic information and density values for the terrain. The process is repeated for each gravity station as they all have different topographic variations in their vicinity.

Oasis Montaj® computes the terrain correction at each station using both a regional correction and a local terrain correction. The procedure is based on a

combination of the methods described by Nagy (1996) and Kane (1962) (Seequent, 2022). The regional corrections account for topography more distant than 3 km and up to a distance of 300 km away from the station to make sure that the gravitational effects of distant topographic variations are accounted for. This 300 km distance is larger than recommended (Hallinan, 1991, as cited in Nowell, 1999), so should be more than adequate. The closer or local correction is divided in 3 zones: near, intermediate and far zones. In the near zone, the effect of the slopes from cell 0 (at the measurement station) to cell 1 (closest diagonal corner of the defined grid) are summed. However, as the slope measurements were not made or easily accessible in our data set, this near zone calculation was not computed for this study. The intermediate zone computes the topographic effect of the 8 closest cells immediately surrounding cell 0 for each station point using the flat-topped square-prism approach of Nagy (1996) (see Figure 2.2). The far zone accounts for all cells from outside the eighth cell out to 3 km. The correction for the far zone uses an annular ring segment approximation to a square prism (Seequent, 2022). SRTM (Shuttle Radar Topography Mission) data with 30 m cell-size was utilized as the digital elevation model for use in the intermediate and far zone. When the terrain correction (TC) is applied to the data, the result is called the complete Bouguer anomaly (CBA), denoted with the symbol g_{CB} , which is given by

$$g_{CB} = g_{SB} - TC. \quad (2.7)$$

This complete Bouguer anomaly is what is usually modeled to determine the subsurface distribution of densities below the geoid datum, as the effect of all the material above has been removed under the assumption of uniform densities.

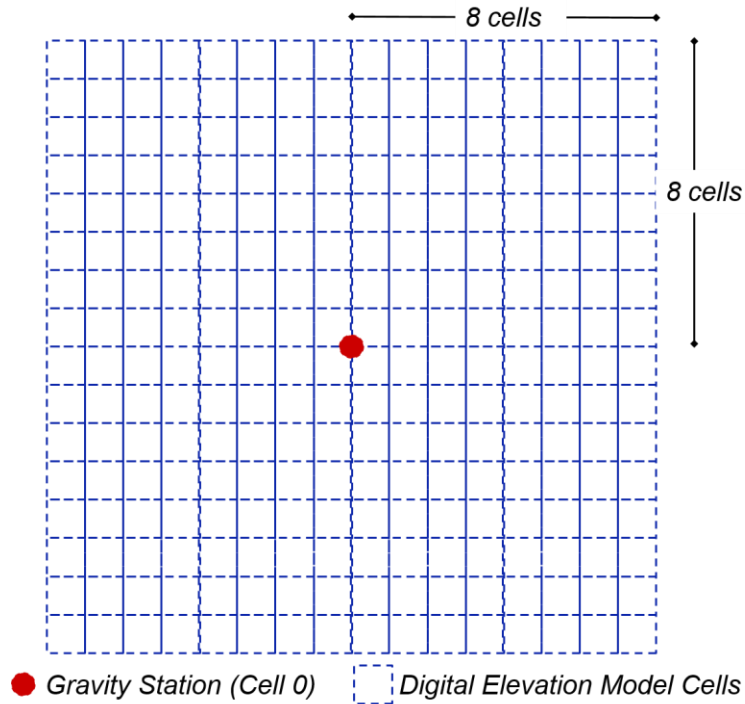


Figure 2.2. Representation of the intermediate zone correction. This step in the terrain correction computes the topography effect of the eight closest cells immediately surrounding cell 0 (at the gravity station).

The gravity corrections described in this chapter will be used in the next chapter to estimate the errors in the corrected data.

Chapter 3: Error Analysis of the Gravity Data and Porcupine-Destor Fault Dip Uncertainties

The gravity modeling procedure requires that the final model have a gravity response that agrees with the measured data. The agreement does not have to be exact, but within some tolerance. Typically, the tolerance is the error in the gravity reading, which requires that this error be quantified. However, there are no published studies that quantify the error in reduced gravity data.

Two methodologies were tested to estimate the error of the gravity data acquired on the Matheson, Watabeag, and Val Gagne traverses. One of these used the well-known error propagation equation. This methodology is used to combine all the individual errors associated with each variable to determine the overall error, which in the case of gravity data is a consequence of the data acquisition and data reduction. The other method was by comparing the partial or final reduced data using repeated measurements. These errors in the data can be propagated to provide an error in the model that is used to fit the data. As an example, we used the estimated gravity errors to estimate an error for the dip of the Porcupine-Destor Fault (PDF), which is present in the study area.

3.1. Error Analysis of the Gravity Data

Uncertainty is the recognition that the results of measurements and observations may deviate more or less from natural reality. The term error, on the other hand, is a quantified estimate of the uncertainty (Bardossy and Fodor, 2001).

Geological models, are subject to many sources of uncertainty (e.g. Mann, 1993; Bardossy and Fodor, 2001) such as measurement inaccuracies, sampling limitations, insufficient sample numbers, imperfect concepts and hypotheses, the need for simplifications, heterogeneity, inherent randomness and other factors (Wellmann et al., 2010). These types of uncertainties may be separated into three categories (Mann, 1993; Bardossy and Fodor, 2001): imprecision and measurement error, stochasticity and imprecise knowledge. Wellmann et al., 2010 provides more details about these three classes for the case of structural modeling:

- Imprecision and measurement error (errors, bias, and imprecision) relates to any uncertainty in all types of raw numerical data that are used for modeling. This includes uncertainty in the measurement, systematic biases, say in the experimental design or the instruments and a lack of precision in the measurements.
- Stochasticity and inherent randomness relates to the fact that there may be heterogeneities or short wavelength variations in what is being measured. Such variations can occur when the data is being sampled less frequently or too coarsely than is appropriate. This will result in uncertainty when this data is interpolated (and extrapolated from) known data points.
- Imprecise knowledge relates to the fact that there can be general conceptual ambiguities and the need for generalisations. For example, some model or structure may be assumed implicitly or explicitly without strong evidence or justification.

The uncertainties associated with gravity data acquisition and corrections (also known as reduction), might be categorized into two types: imprecision (measurement error), and stochasticity (inherent randomness). An example relates to the measurement of the station height, which uses the GNSS signal from satellites. Changes in the atmospheric conditions can change the signal paths and produce what appear to be random changes. On the other hand, the spatial distribution of the satellite constellations in the sky mean that there are many satellites distributed in multiple directions (north, south, east and west) around the measurement station, so the easting and northing can typically be estimated with of a higher precision than height since there are only a few satellites directly above the station and none below.

Estimating the error associated with the gravity data does not provide an uncertainty in the subsurface model, since there are several other sources of uncertainties involved in potential-field modeling. However, knowing the uncertainty in a gravity measurement is the first step towards quantifying the uncertainty in the model, which will ultimately allow us to have more confidence in the model. Importantly, the gravity data error provides, whether for forward models or inverse models, a good estimate for the expected misfit between the predicted data and the observed data.

In this study, the gravity data error is estimated in two ways. 1) By calculating the variability of the gravity readings *after reduction* for stations where readings have been taken multiple times at the same station. The reduction process is undertaken independently for each of those reading using independent estimates of the reduction parameters that are associated with that measurement (position, height, drift, etc.). Ideally, the reduced gravity reading would be identical, as the subsurface geology does

not change over the period that the readings are taken. Hence, any variations will be due to random errors, imprecision or some other cause. 2) By estimating the uncertainty of all the parameters used in the reduction formula (position, height, drift etc.), these errors can be propagated through the formulae to estimate the error in the reduced gravity reading. This methodology is known as error propagation (Bevington et al., 1993) and commonly taught in first-year physics classes.

3.1.1. Error Estimation via Error Propagation Equation

The errors associated with the ME gravity data set were estimated by determining the error associated with each parameter in a gravity correction formula and propagating these errors through a formula to determine the error in the corrected data. The general error propagation equation for a dependent variable x , which is a function of one or more different measured variables (u , v , and any other variables there might be), is given by the following approximation (Bevington and Robinson, 1992):

$$\sigma_x^2 \cong \sigma_u^2 \left(\frac{\partial x}{\partial u} \right)^2 + \sigma_v^2 \left(\frac{\partial x}{\partial v} \right)^2 + \dots , \quad (3.1)$$

where σ_u , σ_v , etc. are the estimated errors of each measured variable, which in this study represent latitude coordinates, elevations, densities. The σ_x could represent the error in an intermediate gravity correction, or a final gravity value.

It is important to highlight that in general, equation (3.1) may be used to quantify the uncertainties on the intermediate or final result if we are neglecting covariant terms

(Bevington and Robinson, 1992). Covariant terms are where there is a correlation between two variables (Menke, 2012)

The error associated with uncertainties of each measured variable acquired or computed in the ME gravity data reduction is described as follows.

3.1.1.1. Gravity Meter Readings Error

The variability of the gravity readings taken with the gravity meter was determined by using repeat measurements (for locations see Figure 3.1). The data acquisition procedure involved occasionally looping back, to get a repeat measurement to check the quality of the data. In total 31 out of 242 (or 13%) of the gravity station measurements have one repeat reading, which provides a sufficient number of points to get a statistically reliable estimate. This procedure, sums several errors associated with the gravity meter itself and several real-time gravity data corrections, such as tidal corrections, equipment drift, and any other corrections the equipment performs in order to correct the readings because of its own technical particularities (temperature corrections, tilt corrections, etc.) (Scintrex, 2012).

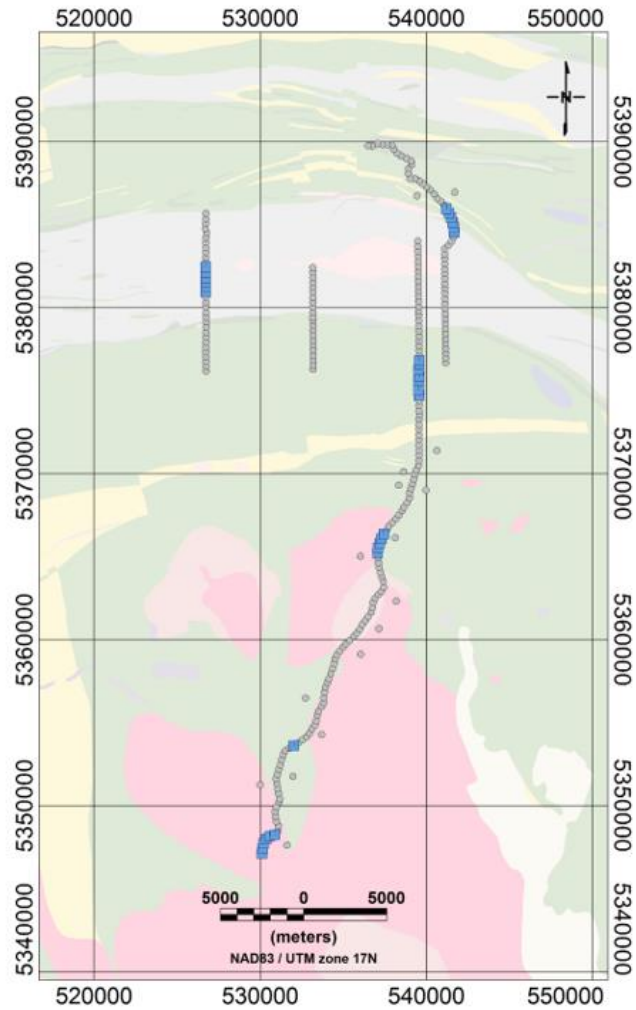


Figure 3.1. Matheson Metal Earth gravity station location (gray dots) and the repeat gravity stations (blue squares) overlaying the geology. In total 242 gravity stations were acquired in this area and 31 of these were reoccupied as repeat measurements.

One way to estimate the error is to calculate the standard deviation, σ

$$\sigma = \sqrt{\frac{\sum_{i=1}^N (x_i - \mu)^2}{N}}, \quad (3.2a)$$

where x_i is the i^{th} repeated measurement value, $i = 1, 2, \dots, N$, N is the total number of repeat measurements and μ is the mean of the N measurement. If the distribution is normal, we can subtract the mean from each measured value and plot a histogram of the resulting difference and we should get a normal distribution, showing a peak close to a difference of zero and having more than 66% of values within one standard deviation of zero. In our case, we do not have a large number of measurements at each station, just two at each station, which is not a good statistical sample for calculating a mean and standard deviation. However, we have 31 stations for which we can calculate 31 mean values and 62 differences. We can therefore modify our formula for the standard deviation to get

$$\sigma = \sqrt{\frac{\sum_{j=1}^N \sum_{i=1}^2 (x_{ji} - \mu_j)^2}{2N}}, \quad (3.2b)$$

where N is the number of stations, μ_j is the mean value of the two measurements x_{j1} and x_{j2} at station j . The histogram of the difference between all the gravity readings and the respective mean is shown in Figure 3.2. The histogram looks like a normal distribution, so this justifies our procedure for calculating a mean at each station and a standard deviation for all the readings. Note that the mean is half way between the two values at each station, one difference will be positive and the other negative and they will have the same magnitude. Hence, the histogram on Figure 3.2 is perfectly symmetric about zero. Using equation 3.2b, gives an error in the gravity readings, σ_{gR} of 0.019 mGal.

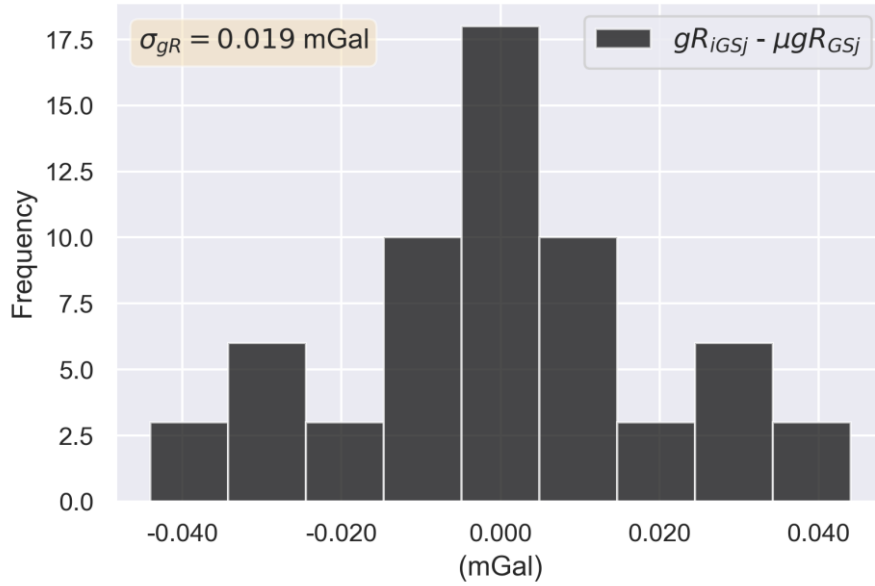


Figure 3.2. Histogram of the differences between gravity readings (gR_{iGSj}) and the average (μgR_{GSj}) obtained for a specific gravity station.

3.1.1.2. Latitude Correction

The uncertainty associated with the latitude correction, also known as the International Gravity Formula Correction (IGFC), is dependent of the accuracy/precision of the latitude coordinates. The error in the latitude position (σ_{ϕ}) was estimated from repeat reoccupations at stations acquiring GNSS location measurements using equation 3.2b. Once again, we have used the procedure involving two measurements at one station, described in the previous section, to calculate the mean and standard deviation. The standard deviation of the latitude coordinates measurements found at the repeat stations was 2.46×10^{-6} degrees (or ~ 0.27 meters) horizontally. The error associated with the latitude correction (σ_{IGF}), was computed using

$$\sigma_{IGF} = \sqrt{\sigma_{\phi}^2 \left(\frac{\partial g_{IGF}}{\partial \phi} \right)^2} \quad (3.3)$$

and gives $\sigma_{IGF} = 6 \times 10^{-5}$ mGal. Equation 3.3 was obtained by substituting the latitude correction formula (equation 2.1) into equation (3.1).

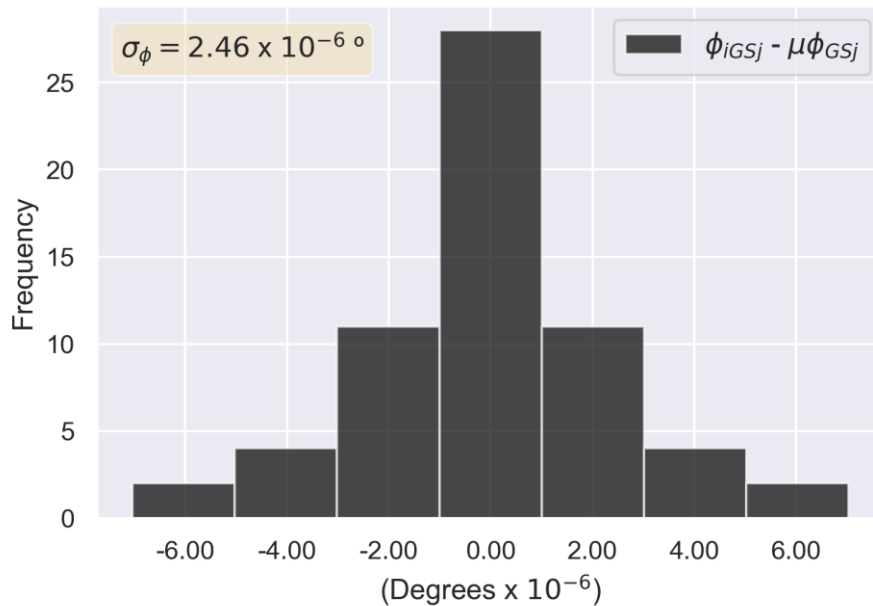


Figure 3.3. Histogram of the differences between latitude readings (ϕ_{iGSj}) and the average obtained ($\mu\phi_{GSj}$) for a specific gravity station.

3.1.1.3. Free-air Correction Error

The errors in this correction are associated with height uncertainties, which come from GNSS height inaccuracies and precision and uncertainties that originate from the ellipsoidal-geoidal data conversion. The GNSS height error (σ_{GNSS}) was estimated to be 0.53 m by applying equation 3.2b to the repeat measurements of the elevation readings,

denoted Sh . Figure 3.4 shows the histogram of the differences in the repeated height measurements. The mean was estimated using the same method described above. The height conversion is based on the Canadian Gravimetric Geoid model of 2013 (CGG13). The CGG13 model error (σ_{CGG13}) in height has been estimated by the Canadian Geodetic Survey (CGS) and varies from place to place. According to CGS documentation, the geoid model is validated using GPS and levelling data and shows differences with a mean of -0.157 m and a standard deviation of 0.131 m, which goes down to 0.073 m after filtering out systematic errors (Natural Resources Canada, 2022). Therefore, 0.230 m was used to avoid underestimation, as this value is the sum of the absolute value of the mean and the standard deviation after filtering. Combining GNSS and CGG13 estimates of height error into the error propagation general formula will give the formula for total height uncertainty σ_h as

$$\sigma_h = \sqrt{\sigma_{GNSS}^2 + \sigma_{CGG13}^2}, \quad (3.4)$$

which has a value of $\sigma_h = 0.57$ m. Combining equation 2.3 with equation 3.1 and including the errors associated with the gravity reading and latitude corrections gives the error associated with the free-air anomaly, σ_{gFA} , as

$$\sigma_{gFA} = \sqrt{\sigma_{gR}^2 + \sigma_{IGF}^2 + 0.3086^2 \sigma_h^2}. \quad (3.5)$$

Using equation 3.5, the free-air anomaly uncertainty was estimated to be $\sigma_{gFA} = 0.176$ mGal.

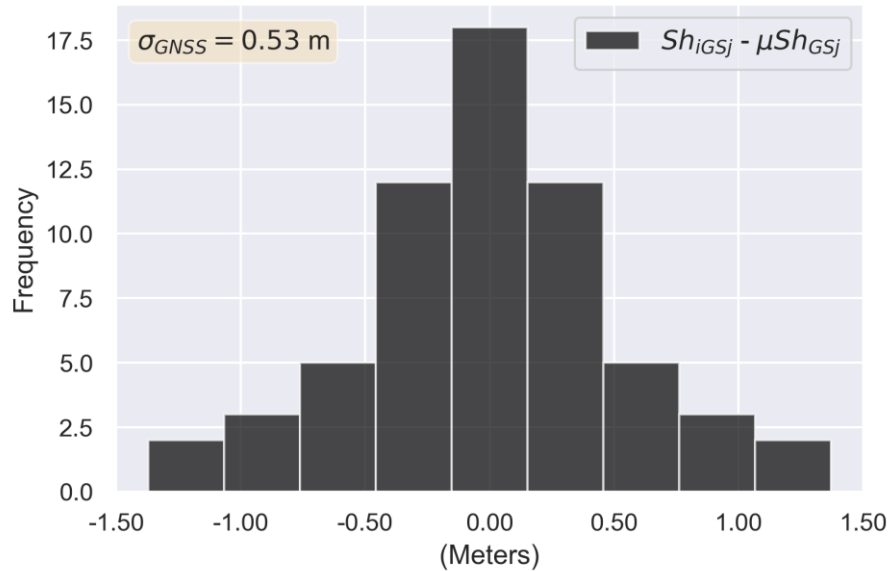


Figure 3.4. Histogram of the differences between GNSS elevation readings (Sh_{IGSj}) and the average obtained (μSh_{GSj}) for a specific gravity station.

3.1.1.4 Simple Bouguer Correction Error

The simple Bouguer correction depends on the height and the Bouguer density value. The uncertainties of the height measurements (σ_h) have already been estimated in the free-air correction section above, but the choice of the Bouguer density value is also a source of error in the Bouguer correction (Chen and Macnae, 1997; Hinze, 2003). The ME project has compiled/acquired more than 15,000 density samples from the Abitibi Greenstone belt area (Eshaghi et al., 2018), and the sample locations include the Matheson study area. However, mafic and intermediate rocks are sampled proportionately more due to their greater economic interest. This is despite the fact that in Matheson and many other areas, felsic batholiths and plutons can cover a larger area. Hence, an unweighted average value of all the samples collected in the compilation of

Eshaghi et al (2018) may not be representative of a true average Bouguer density value. Gibb (1968) has weighted the density by the percentage of mapped outcrop and estimated the average density as 2.67 g/cm³. The density values from Gibb's (1968) study came from a study in the Precambrian shield areas of Northern Manitoba, which included over 2000 individual density measurements. Therefore, this weighted average value has been used in the Bouguer correction and we have assumed that it is reasonable to neglect this as a source of error. A more sophisticated approach might take into account the density associated with mapped geology in the local area, but software for this purpose would have to be developed and tested and this is beyond the scope of this study.

As the free-air and simple Bouguer correction, are both functions which depend on the height variable, so they are covariant. Furthermore, they are of opposite sign, so including a height term twice will overestimate the size of the error compared with the size of the correction. This issue can be avoided by combining the free-air correction and simple Bouguer correction equation into a single expression

$$g_{SB} = g_R - g_{IGF} + h(0.3086 - 0.04192\rho), \quad (3.6)$$

which if we use a Bouguer density of 2.67 g/cm³ becomes

$$g_{SB} = g_R - IGFC(\phi) + 0.1966h, \quad (3.7)$$

so the error is

$$\sigma_{SB} = \sqrt{\sigma_{g_R}^2 + \sigma_{IGF}^2 + 0.03868\sigma_h^2}, \quad (3.8)$$

which gives a value of $\sigma_{SB} = 0.113$ mGal.

3.1.1.5. Terrain Correction Error

The terrain correction (Nowell, 2005) is complex and involves multiple weighting factors and a variety of data that are input (slopes and heights). The errors in the terrain correction will depend most critically on the quality of the terrain model and how the topography is quantified around the gravity station (Nowell, 2005). It can also depend on other factors that are difficult to quantify such as the flatness of the location that the operator selects as the position of the gravity station. As with the simple Bouguer correction, density distributions might be a source of error in the terrain correction as well (Xia and Dewhurst, 1986). Another important feature that could introduce errors might be the presence of a body of water close to the gravity station, which also has to be properly accounted for during this correction (Ugalde et al., 2006). In some terrain models, such as the SRTM, the terrain model is the upper surface of lakes, rivers, etc. and in many cases the computer algorithm assumes that the material below this upper surface is rock with a Bouguer density (typically 2.67 g/cm^3). In fact, the density of water is much lower, so the correction will be incorrect in that case. In order to calculate an appropriate correction, it is necessary to know the depth of water (that is, the lake bathymetry).

Terrain corrections account for additional material above the Bouguer slab or a lack of material below the slab and a water body is an example of the latter. In order to quantify the effect that a body of water has on the terrain correction, a study has been computed and analysis being made in another project area (the Sudbury Metal Earth transect). In this region, a massive body of water (Lake Wanapitei) is located proximal to the gravity profile and the bathymetry for this lake is known, being 123 m at its deepest part (see Figure 3.5-*i*). Otherwise, the Sudbury traverse survey specifications are

essentially the same as those in the Matheson area. Figure 3.4 compares the complete Bouguer anomaly (terrain corrected) data when reduced using two different scenarios:

- Scenario 1 – the lake water density was set to the density value used for the Bouguer slab (2.67 g/cm^3). This is equivalent to not knowing that there is a low-density lake below the terrain, or having a hill of height 123 m above the terrain with a density of 1.67 g/cm^3 (which is roughly equivalent to a hill of 76 m with a density of 2.67 g/cm^3). This is a significant hill in the Abitibi greenstone belt, so this scenario could be considered an example of the maximum error that could be expected if the terrain correction is done incorrectly.
- Scenario 2 – the material in the lake was assigned a density equal to the value for water (1 g/cm^3) and the thickness of the lake from the lake bathymetry is taken into account. This is an example of a scenario when the terrain correction is done correctly.

The highest value of the differences between the terrain correction determined in these two scenarios was used as the maximum terrain correction errors (σ_{TC}), which is numerically equal to 0.040 mGal (see Figure 3.5-*ii*). In areas with different topography a different value would be obtained, typically smaller, as this lake is deep or the equivalent hill is relatively high.

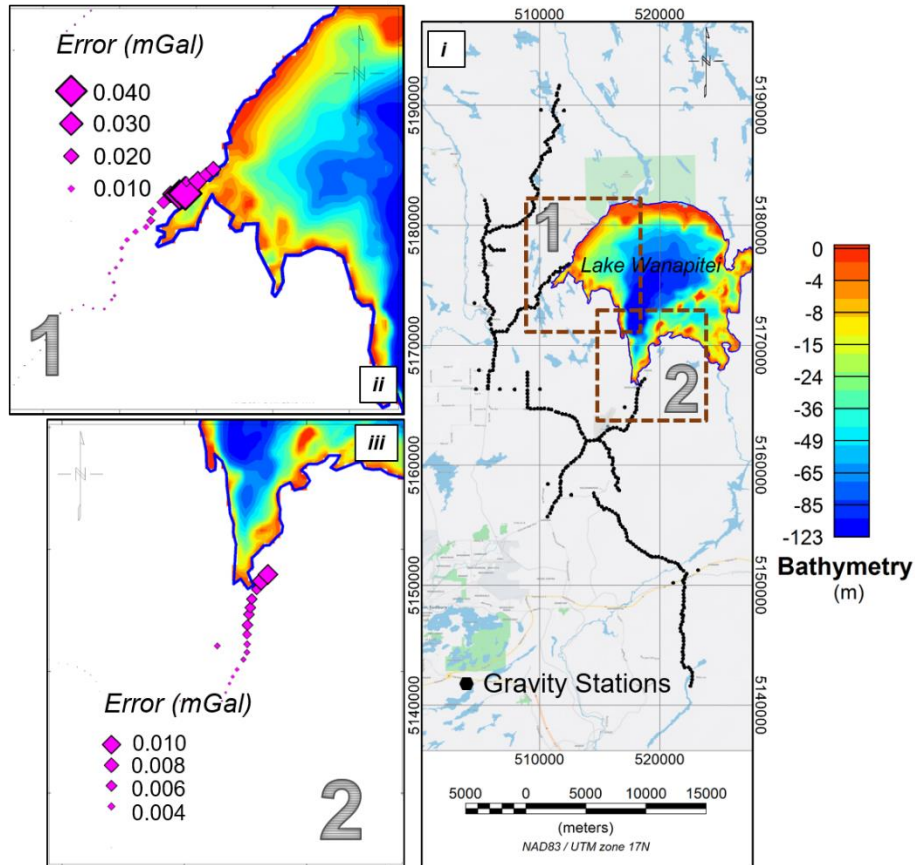


Figure 3.5. (i) Metal Earth Sudbury transect gravity stations and Lake Wanapitei with its bathymetry shown in color. The closest gravity stations have been selected to assess the effect of the lake on the gravity measurements (ii and iii). Bathymetry source: Land Information Ontario Database (10 m accuracy).

The errors associated with the complete Bouguer anomaly was estimated as being equal to 0.120 mGal and was obtained using

$$\sigma_{CB} = \sqrt{\sigma_{SB}^2 + \sigma_{TC}^2}. \quad (3.9)$$

Even though, there is no lake as large as Wanapitei Lake in the Matheson area, this value provides a reasonable estimate of the upper limit of the uncertainties associated with the Bouguer anomaly in the study area.

3.1.2. Error Estimation via Repeated Measurements Comparison

An alternative method to using the error propagation equation was also used to estimate the gravity data error. In this methodology independent values of the final or partially reduced data at the repeat points are used to estimate the errors associated with free-air, latitude and Bouguer corrections. These repeat measurements tests do not account for errors that remain the same at a station, such as the estimate of the geoid and terrain correction errors. However, this method would be simpler than the error propagation formula. It should also be consistent with the error propagation method, particularly as the geoid and terrain correction errors have been shown to be small.

Figure 3.6 shows the histogram of the differences between the repeat readings of the gravity reduced to the free-air anomaly FA_{GSj} and the average value at the relevant gravity station μFA_{GSj} .

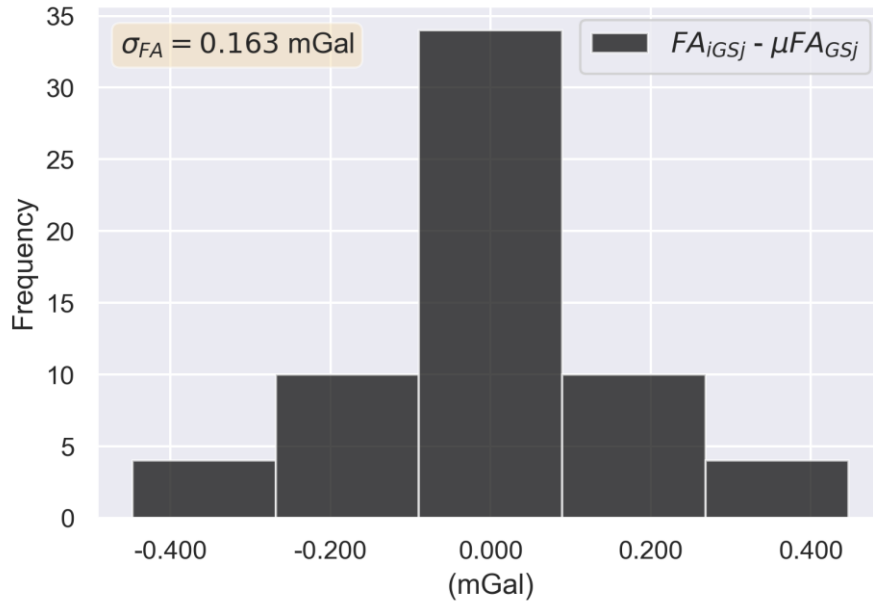


Figure 3.6. Histogram of the differences between the free-Air anomaly reduced data point (FA_{iGSj}) and the average obtained (μFA_{GSj}) for the relevant gravity station.

The free-air error (σ_{FA}) was obtained by determining one standard deviation of the differences between the free-Air anomaly reduced data point (FA_{iGSj}) and the average obtained (FA_{GSj}) at the repeat gravity stations. Using equation 3.2b, the value obtained was $\sigma_{FA} = 0.163$ mGal.

Like σ_{FA} , the error associated with the simple Bouguer anomaly was calculated from the repeat measurements using equation 3.2b, giving $\sigma_{SB} = 0.104$ mGal. See Figure 3.7 for the histogram.

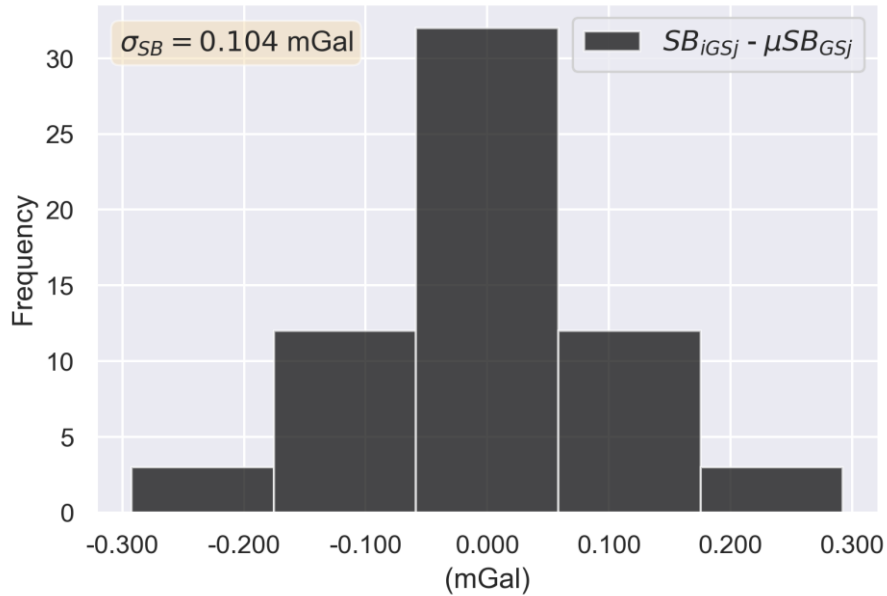


Figure 3.7. Histogram of the differences between the simple Bouguer anomaly reduced data point (SB_{iGSj}) and the average obtained (μSB_{GSj}) for the relevant gravity station.

The final gravity correction is the terrain correction, which after application gives the complete Bouguer anomaly. Analyzing the differences in the repeat estimates of the CBA in a similar manner to above gives a standard deviation of $\sigma_{CB} = 0.109$ for the Matheson gravity survey and data processing. Figure 3.8 shows the histogram associated with the differences.

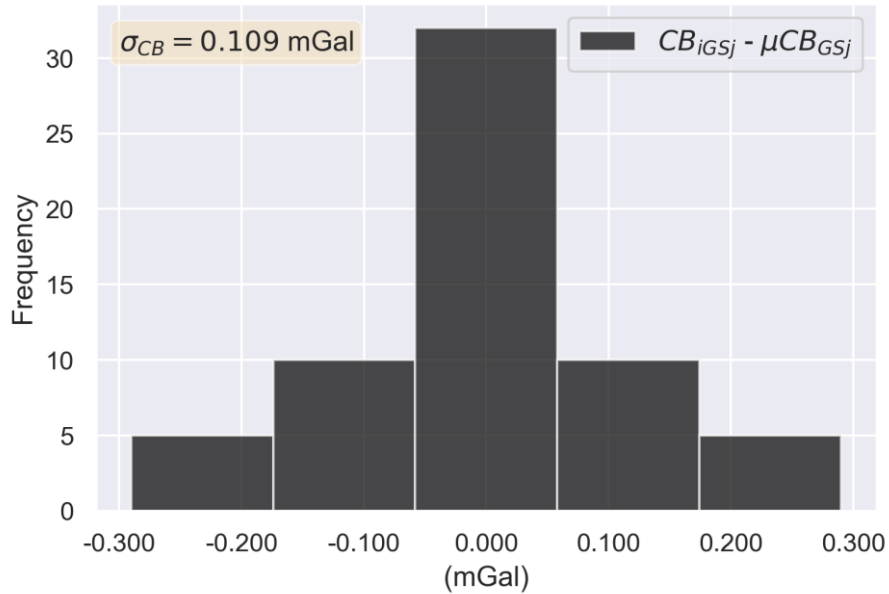


Figure 3.8. Histogram of the differences between the complete Bouguer reduced data point (CB_{IGSj}) and the average obtained (μCB_{GSj}) for the relevant gravity station.

In Table 3.1, the data errors estimated using the two different methodologies are compared. The second column shows the errors obtained by error-propagation estimates, and on the third column the errors derived from comparison of the repeated reduced-data measurements. The results from the two methodologies seem to be consistent.

Table 3.1. Error estimations comparison obtained from two different methodologies.

	Error Propagation Equation (mGal)	Reduced data of repeat measurements (mGal)
Free-Air anomaly (σ_{FA})	0.177	0.163
Simple Bouguer anomaly (σ_{SB})	0.114	0.104
Complete Bouguer anomaly (σ_{CB})	0.121	0.109

The lower uncertainty for the simple Bouguer correction compared with the uncertainty of the free-air correction is consistent with the result from the error propagation method. The complete Bouguer anomaly error is only marginally larger than the simple Bouguer anomaly error since the terrain corrections are relatively small.

Even though both estimation methodologies are comparable, the survey requirements are different for each method. The error propagation does not require retaking measurements at selected gravity stations, it does require some extra measurements to estimate the individual errors of the variables needed in the data reduction such as elevation, and latitude. The advantage of the error-propagation-equation method is that knowing the errors of these extra variables provides the uncertainties for every step throughout the data reduction. However, the repeat measurements method is only able to reveal the data error in the final corrected data, such as free-air anomaly, Bouguer anomaly, etc. The advantage of repeat measurements as a quality control (QC) procedure is that the errors can be estimated and compared as the data is acquired. The disadvantage is that the estimates are dependent on the location of the repeat station, so that a location where, for example, there is poor GPS signal, will give a large error, which might not be representative of the error at other locations.

Regardless of which method is being used, the survey ought to be designed and planned to provide adequate information for the error analysis. This planning would include selecting the repeat station location at a number of different locations representative of different conditions. This selection process requires experience to know where the conditions might be poor or good. In a new area, or when working with a new crew, one way of gaining this experience might be to use the error propagation method in the first part of a survey.

The error analysis using the error propagation equation was able to highlight how the accuracy/precision of the elevation measurements plays an important role on the overall uncertainties of the gravity-data reduction. The largest contribution to the error comes during the free-air correction since an adjustment of 0.3086 mGal/m is added to a measurement to compensate for the change in the gravitational field with height. If the datum height is significantly different from the measurement height, then this contribution can result in a large error. However, a subsequent Bouguer correct has the opposite sign and can cancel a significant portion of this error.

The uncertainty related to the terrain correction is burdensome to estimate using the error propagation method, since it is time-consuming to compute the derivatives with respect to all the variables used during the terrain correction. When the Bouguer correction is important, perhaps the repeat measurement method is most appropriate. If the input data used for the terrain correction (terrain density and terrain height) at a particular location do not change, then the terrain correction will not change and will not generate any additional variability or uncertainty in the final result. Therefore, an error propagation approach can be suitable and is recommended at some representative

locations at the start of a survey. In the ME gravity surveys generally, and the MSA survey specifically, about 10% of all gravity stations were reoccupied and repeat measurements were taken. Since the error estimated using this methodology is consistent with the error propagation estimation, this suggests that a repeatability rate of 10% is adequate for acquisition in the MSA. However, this study has not analysed whether this rate could be reduced and still provide reliable uncertainty estimations. As these repeat measurements add extra cost at the data acquisition stage, future studies could be undertaken to see if error estimates comparable to the error propagation method could be obtained with fewer repeat measurements. The Matheson area is relatively flat, so the 10% number could be different in a different area. The size of the survey might also be a factor in determining the optimal number of repeat stations in Matheson there were 242 stations and 31 stations were repeated, which is 13% of stations, which is close to 10%. However, about 30 repeated measurements is also a good number of measurements to check that a measurement is normally distributed (Tukey, 1977) and to estimate the standard deviation. A useful strategy might be to collect repeat station until the errors look normally distributed and once the variance can be estimated with confidence, the number of repeat stations reduced. Repeat stations can have other uses, for example checking for a sudden offset (or tare) in the gravity meter, so after the variance is estimated the repeat measurements could be set to the minimum number required for this purpose.

3.2. Porcupine-Destor Fault Dip Estimation

In this section, we provide an example of how the estimated uncertainties for the reduced gravity values can be used to estimate the uncertainties in structural models derived from this data.

Previous workers have sought to quantify the uncertainty in estimating the dip of fault structures that are modeled using gravity data by approximating the structure by two semi-infinite horizontal slabs with a dipping interface and in some cases a slip along the interface (Geldart et al., 1966; Abdelrahman et al., 1989). Work that is more recent has been presented to enhance the confidence in estimating the characteristics of these structures (Essa, 2013; Kusumoto, 2017; Elhussein 2021). One challenge in having a confident estimation of the structural dip of contacts and faults, when derived from gravity modeling, is dealing with the non-uniqueness problem, an inherent issue with potential-field data (Jacoby and Smilde, 2009). Although these workers have significantly contributed towards obtaining more reliable estimates of the dip, they did not explicitly quantify the estimation uncertainties per se, neither from the data errors nor from the inherent non-uniqueness problem. This study aims to provide a procedure for estimating the fault-dip-estimation errors associated with the gravity data uncertainties whilst minimizing the non-uniqueness problem.

The Porcupine-Destor Fault (PDF) zone, a first-order, crustal-scale fault that is associated with a number of gold deposits (Monecke et al., 2017), has long been recognized as the major structure of the study area, but there is a lack of clear and detailed geological data about this structure because of its poor exposure (Bateman et al., 2005). Nevertheless, recent geophysical studies have indicated that the PDF is

dipping gently south (Snyder et al., 2008; Della Justina and Smith, 2020; Haugaard et al., 2021).

The lithologies to the south of the PDF are rocks of the Lower Tisdale assemblage and to the north is the Porcupine assemblage (see Figure 3.9). The Porcupine assemblage (2690 to 2685 Ma) consists of wacke, siltstone and mudstone displaying Bouma sequence subdivisions that indicate predominantly distal deposition by turbidity currents (Ayer et al., 2007). The Lower Tisdale assemblage (2710 to 2706 Ma) consists predominantly of tholeiitic mafic volcanic rocks with lesser komatiite, intermediate to felsic calc-alkaline volcanic rocks and iron formation (Ayer et al., 2007). Snyder et al., 2008, suggested that the Lower Tisdale assemblage also underlies the Porcupine assemblage.

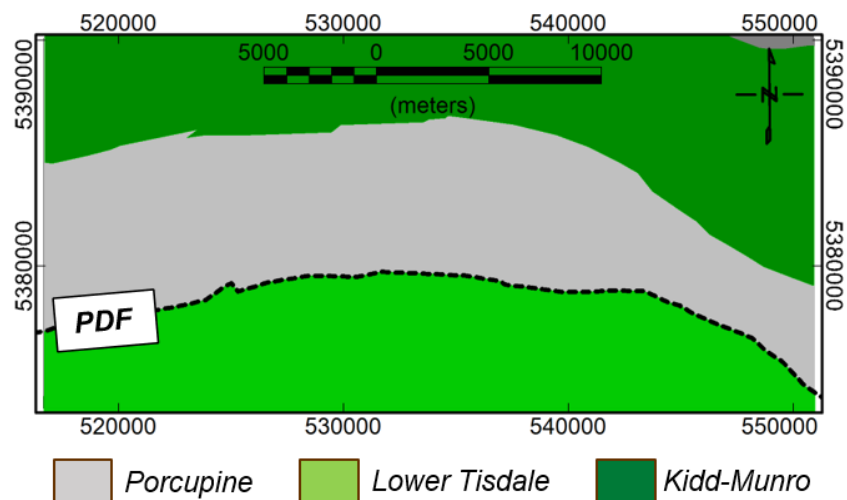


Figure 3.9. Porcupine-Destor fault (black dashed lines) and the surrounding geology (Ayer et al., 2005).

In this study, the dip of the Porcupine-Destor Fault has been estimated in three different locations by 2D forward modeling. In the modeling, *a priori* information was used,

specifically density and seismic information, to remove some of the non-uniqueness to constrain the modeling. Furthermore, the gravity data error has been taken into account to provide an estimate of the error associated with estimation of the PDF dip angle.

3.2.1. Forward Modeling

In forward modeling, the interpreter adjusts the model parameters until a match between the model and observed data is obtained (Dentith and Mudge, 2014). Some geological structures such as fracture zones, faults, dikes, rift zones, and anticlines, are often elongated and unchanging along a direction, typically called a strike direction. This means that gravity anomalies that they produce are also elongated in this direction, so they have a linear appearance on a map. If the anomalies are sufficiently “linear”, it may be possible to consider the gravitational response as essentially invariant in the direction parallel to the elongated direction (Blakely, 1996), also known as the infinite-strike-length case (Dentith and Mudge, 2014). If the y axis is assigned to be parallel to the invariant direction only the x and z dimensions of the body need to be adjusted in the model (Blakely, 1996). In this case, a three-dimensional (3D) density model, ρ , that could depend on three spatial variables (x, y, z) , simplifies to

$$\rho(x, y, z) = \rho(x, z), \quad (3.11)$$

and the body and hence the model is said to be two dimensional or 2D.

A very useful variation of the 2D model, which removes the restriction of infinite strike length, and is easier to specify than the more complex 3D model, is a model with constant cross-section as in the 2D model, but only extends over a finite strike length.

This is called a 2.5D model, and it gives the interpreter some control over the third dimension without the complexity of manipulating a full 3D model (Dentith and Mudge, 2014). Along the PDF, the gravity response varies sufficiently slowly along strike, that we can assume a 2D model.

3.2.1.1. *The Gravity Anomaly due to a Polygon*

The gravitational attraction due to a 2D body can be expressed as a line integral around its periphery (Hubbert, 1948). However, Talwani et al. (1959), considered the case of a single n -sided polygon and broke the line integral up into n contributions, each associated with a side of the polygon (Won and Bevis, 1987). The expressions for the vertical (z) and horizontal (x) components of the gravity anomaly at a point, which is located at the origin of the coordinates system, is given by (Won and Bevis, 1987)

$$\Delta g_z = 2G\rho \sum_{i=1}^n Z_i \quad (3.12)$$

and

$$\Delta g_x = 2G\rho \sum_{i=1}^n X_i , \quad (3.13)$$

where Z_i and X_i are line integrals for that component along the i th side of the polygon for that point G and ρ are defined as the gravitational constant and the density of the polygon respectively. When a model is comprised of multiple polygons, the gravity anomaly is the sum of the anomalies from each polygon.

3.2.2. PDF Dip Estimation - Constraint A: Density Compilation

Whereas the density values from the Metal Earth database, which was compiled as part of the Metal Earth project (Eshaghi et al., 2018), provide an adequate number of samples for the Lower Tisdale assemblage (90 samples), only 21 samples are available for the Porcupine assemblage. In order to increase the number of samples, 25 extra samples were utilized to estimate the mean density of the Porcupine assemblage. These samples were obtained from the geological mapping undertaken by the transect geologist in 2019. The specific gravity values (or relative densities) were obtained from weighting the samples in air and in water (see Figure 3.10). Combining the density compilation dataset with these measurements gives 46 density samples for the Porcupine assemblage.



Figure 3.10. Rock-density estimation apparatus, shown when weighting a rock sample submerged in water.

The location of the Lower Tisdale assemblage samples and the Porcupine assemblage samples in our study area are shown on Figure 3.11. The mean density obtained for the Porcupine assemblage ($\mu_{\rho_{Porc}}$) samples was $2.73 (\pm 0.04) \text{ g/cm}^3$ (see the histogram on Figure 3.12). A value of $2.89 (\pm 0.10) \text{ g/cm}^3$ was the mean determined to the Lower Tisdale assemblage ($\mu_{\rho_{LT}}$), as shown on Figure 3.13. In each case, the uncertainty given in brackets is one standard deviation. The total of samples utilized for

estimating the density values for Porcupine assemblage and Lower Tisdale were 46 and 90, respectively.

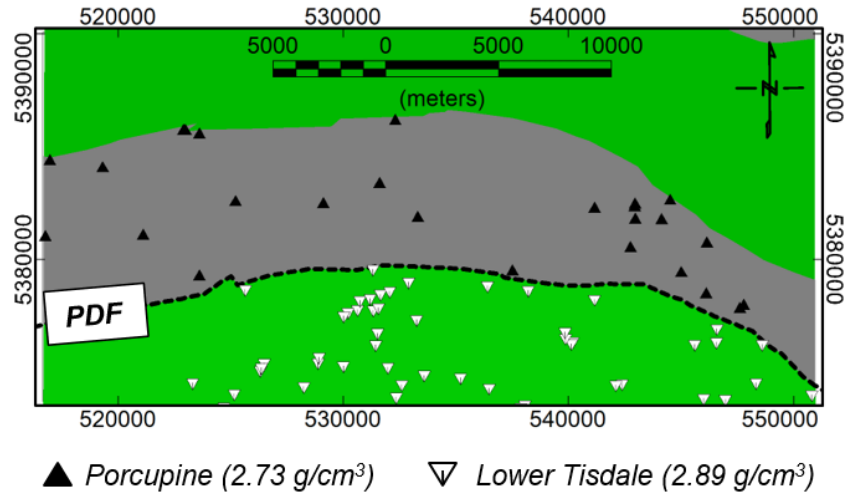


Figure 3.11. Spatial distribution of the density samples compiled to constrain the model. Some symbol location might represent more than one sample, either on an outcrop or in a borehole.

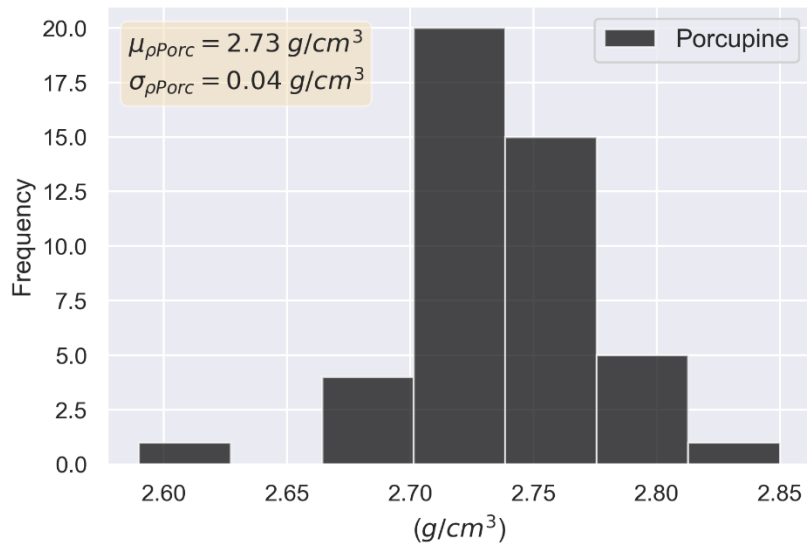


Figure 3.12. Histogram of the estimated density values of the Porcupine assemblage indicating its density mean ($\mu_{\rho_{Porc}}$) and the standard deviation ($\sigma_{\rho_{Porc}}$).

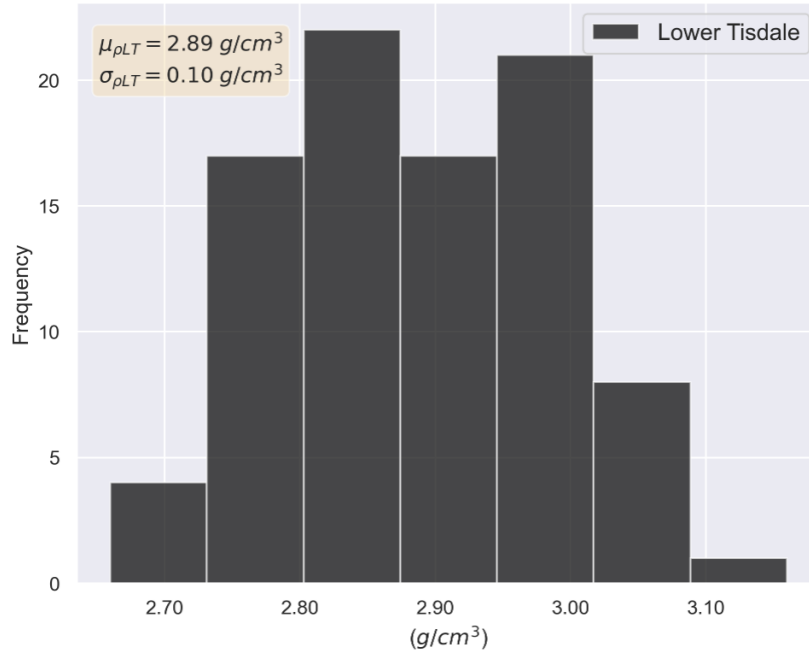


Figure 3.13. Histogram of the estimated density values of the Lower Tisdale assemblage indicating its density mean ($\mu_{\rho_{LT}}$) and the standard deviation ($\sigma_{\rho_{LT}}$).

3.2.3. PDF Dip Estimation - Constraint B: High Resolution Seismic Sections

Three high-resolution seismic reflection sections were utilized to help construct the initial model, since these provide high-resolution images of structures within the crust. The seismic data were part of the Metal Earth project (Naghizadeh et al., 2019). All the seismic profiles were acquired using Vibroseis sources. The survey utilized source and receiver spacing of 6.25 and 12.5 m, respectively, and one sweep was recorded in each source location. The natural frequency of the receivers is 5 Hz with a low-cut recording filter of 2 Hz. The sampling rate was 2 ms, so that the maximum-recorded frequency was 207 Hz (Cheraghi et al., 2020).

Whereas the compilation of density samples is crucial to resolve the petrophysical ambiguity in the gravity model, the seismic data can help to resolve the depth and/or the geometry of the source in gravity modeling. Figure 3.14 shows the seismic sections in the top four kilometers of three sections. On each section, there is no reflector that could be identified and interpreted as the PDF, which would be the contact between the Lower Tisdale (above) and the Porcupine (below). Nor is the PDF apparent as a structure, which has terminated imaged features on either side of the fault. There are a few small terminations, but these cannot be tied together to interpret a single coherent fault structure. The strongest reflector apparent in each section is marked with the dashed green line. These reflectors have been interpreted as the bottom of the Porcupine assemblage, an interpretation consistent with previous studies (Snyder et al., 2008; Della Justina and Smith, 2020; Haugaard et al., 2021). The south end of this reflector diminishes in strength gradually, so it is not possible to recognize a termination at the PDF. If this termination were obvious, then the location of the termination and the location of the PDF on surface would define the dip of the PDF. Because the termination is not obvious, the location of the dashed line is uncertain and the dip angle has been labeled with a question mark highlighted in yellow.

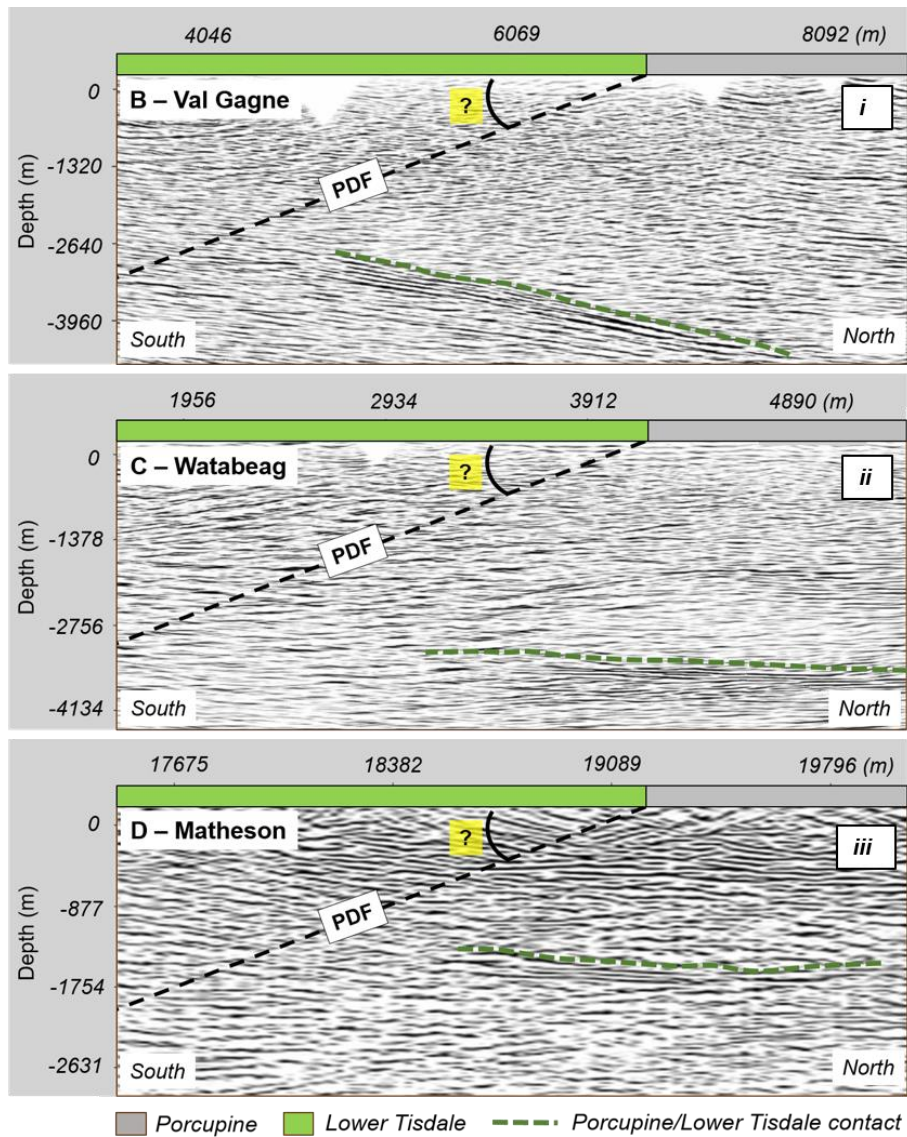


Figure 3.14. Segments of Val Gagne (i) Watabeag (ii) and Matheson (iii) interpreted seismic sections. The green dashed line indicates strong reflectors interpreted as the bottom of the Porcupine assemblage, but this gradually weakens to the south (left), so the location where it ends is not clear. The PDF, marked with a black dashed line is not a strong reflector, nor does it show coherent truncation, hence the location of the PDF is uncertain. The figure has a question mark, which indicates that the PDF dip angle is to be estimated. The location of these sections are shown in Figure 3.16.

3.2.4. PDF Dip Estimation: Gravity Data

The role of the gravity modeling will be to resolve the unknown dip of the PDF. As constraints, we will use densities from our density compilation, we will assume that the green line interpreted on the seismic section is the base of the Porcupine assemblage and we will assume that the top of the PDF is as marked on the geological map. We will also make the simplifying assumption that the PDF is linear and dipping to the south. This means that the only unknown is the dip angle and we will seek to estimate the uncertainty in this angle. Just one unknown also means that there is no inherent ambiguity in the model.

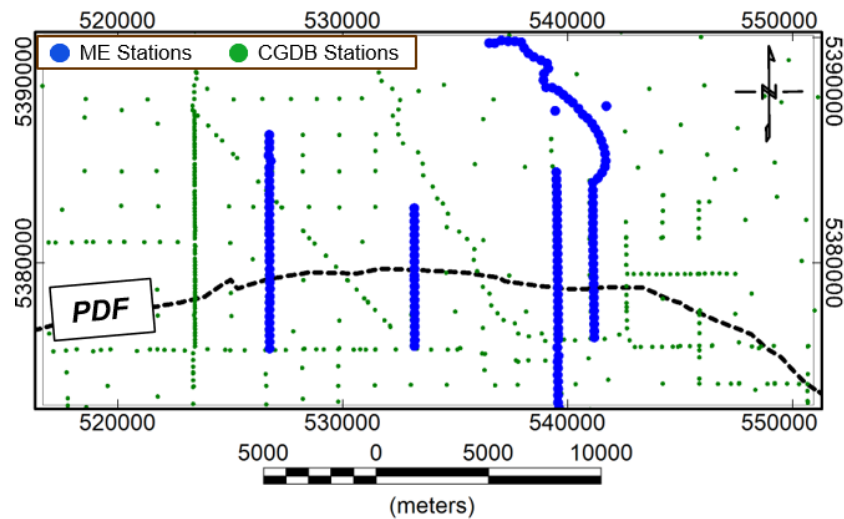


Figure 3.15. ME and CGDB gravity stations location in the study area.

Figure 3.15 shows the gravity-station locations of the available data in the study area. The data comes from the Canadian Gravity Database (CGDB) compilation (green dots), and the ME traverse data (blue dots). The CGDB is managed by the Canadian Geodetic Survey and it is available to download at the Government of Canada website

(Natural Resources Canada, 2016). Once combined, these two datasets provide a good coverage in the area and the complete Bouguer anomaly map is shown in Figure 3.16. In this map an anomalous low immediately north of the PDF is evident and is interpreted to be due to the Porcupine assemblage. However, only the ME data was used to estimate the dip of the PDF, since only this data has estimated uncertainties.

The impact of data uncertainties on geological/geophysical models has been discussed by previous workers (Roy et al., 2005; Wellmann et al., 2010; Lindsay et al., 2012; Kelley et al., 2014; Jin et al. 2020; Olierook et al., 2021). There is a consensus that uncertainty assessment should be a part of the data modeling in most studies.

The data marked with blue dots on Figures 3.16 and 3.17 (the geology map) were selected to determine the dip of the PDF and its uncertainty. The length of the profiles is about 3 km and this length was selected for a number of reasons. 1) The approximately 12 samples should be sufficient to resolve a single parameter, the dip. 2) This width is comparable to the depth to the bottom of the section of the PDF that has a density contrast. (Below the Porcupine Assemblage, there is interpreted to be no density contrast as the PDF has the Lower Tisdale both above and below). 3) These 3 km sections of the profiles are where the gravity gradients are steepest and will be most responsive to the nature of the density contrast in the subsurface. Profiles of the complete Bouguer anomaly data along these short focussed profiles are shown in Figure 3.18.

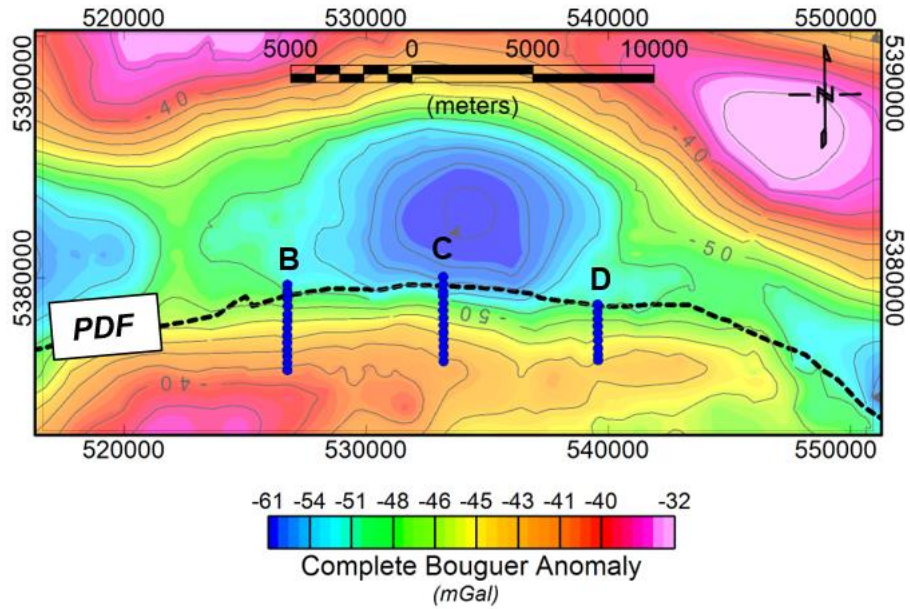


Figure 3.16. Complete Bouguer anomaly map, generated using a compilation of the ME and CGDB data, overlaid by the Porcupine-Destor fault and the ME selected gravity stations.

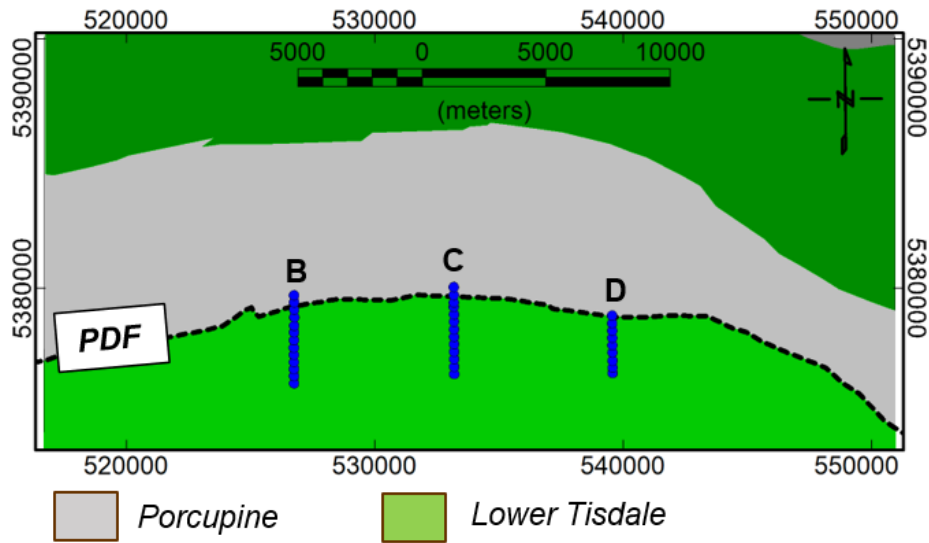


Figure 3.17 Geology map overlaid by the Porcupine-Destor fault and the ME selected gravity stations.

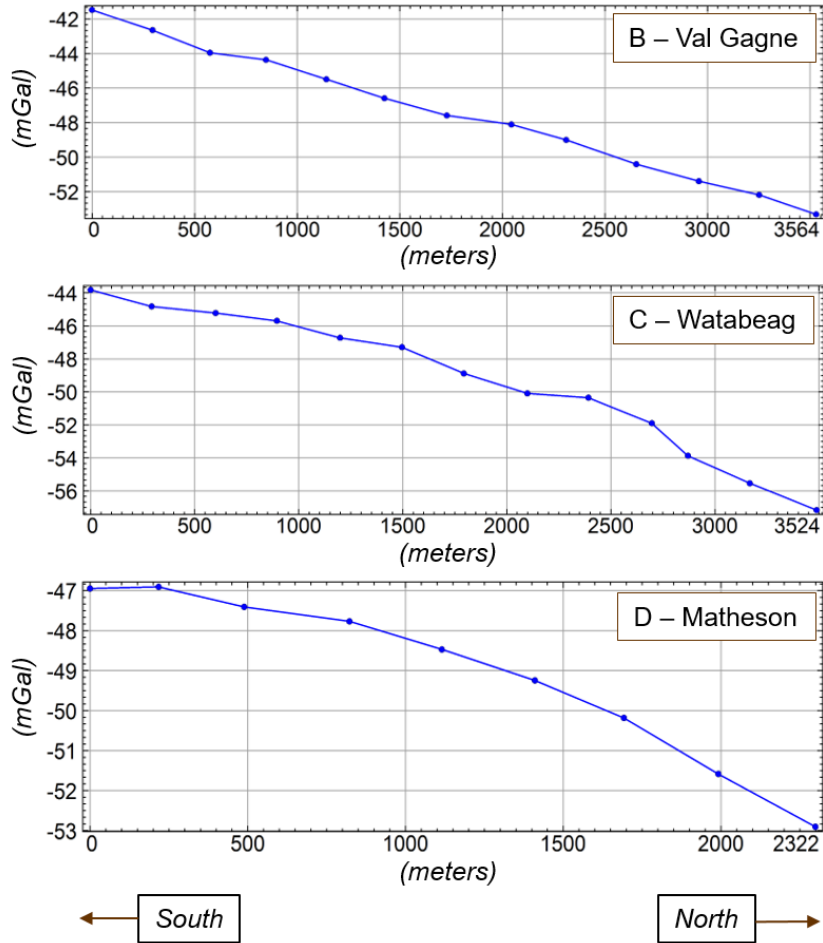


Figure 3.18. Focused complete Bouguer anomaly gravity profiles along the Val Gagne (B), Watabeag (C) and Matheson (D) profiles.

Taking into account all of the aforementioned constraints and assumptions, the gravity data along the profiles were modeled with the 2D forward modeling program GM-SYS and will be discussed in the following section. Typically, a number of models with different dip angles can be tried, and the model that provides the lowest misfit between the predicted data and observed data, is deemed to provide the more plausible fault dip. However, this approach does not provide an uncertainty for the estimated PDF dip. As there is an uncertainty in the gravity data, there is no need to fit the data better than the

data uncertainty. In the following section, we exploit this data uncertainty to estimate the model error.

3.2.5. PDF Dip Estimation: Contaminating the Data with Random Noise Normally Distributed

In Section 3.1, we estimated the gravity data error for the complete Bouguer anomaly (CBA) as 0.121 mGal using the error propagation equation. In order to investigate how this data error might effect the final result of the modeling, the observed CBA (reduced) data was contaminated with random noise consistent with this error and consistent with a normal distribution. In practice, this was done by ensuring that the standard deviation of the applied noise is numerically equal to that of the data error. In other words, any contaminated data sets are a stochastic representation of the observed data, since the contaminated data and the reduced gravity data have the same uncertainty and agree with each other to within experimental error.

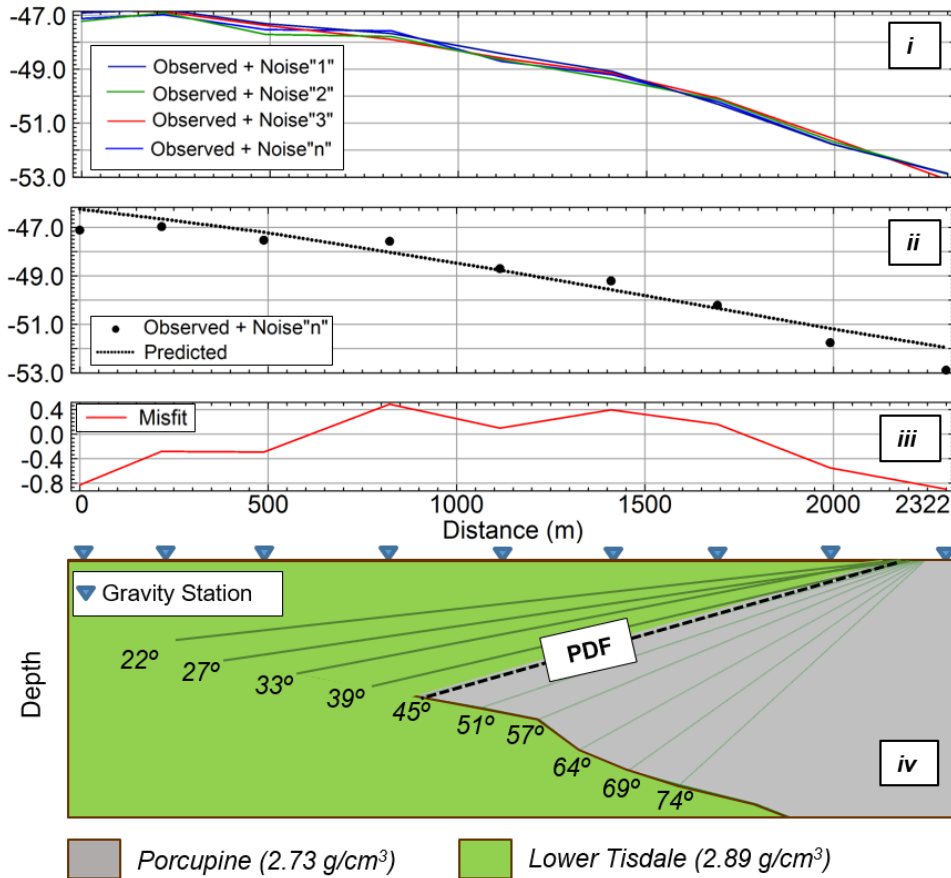


Figure 3.19. Four Matheson profile datasets after contamination with noise with uncertainty 0.121 mGal (*i*) and one of these datasets ('n') is compared to the predicted data (*ii*). Panel *iii* shows the misfit between the contaminated data and the data predicted for the model revealed in *iv* that has a dip of 45°.

Figure 3.19-*i* shows the observed data from section D at Matheson after it has been contaminated with four different noise ensembles, each consistent with the mean and standard deviation of the measured data. For each of these contaminated observed data (Figure 3.19-*ii*), there is a model with a dip angle that provide the lowest misfit (Figure 3.19-*iii*) assuming the fault plane is linear (Figure 3.19-*iv*). Recall that the bottom of the

porcupine assemblage is constrained by seismic data interpretation by extrapolating the strong reflection to the south until it intersects the PDF.

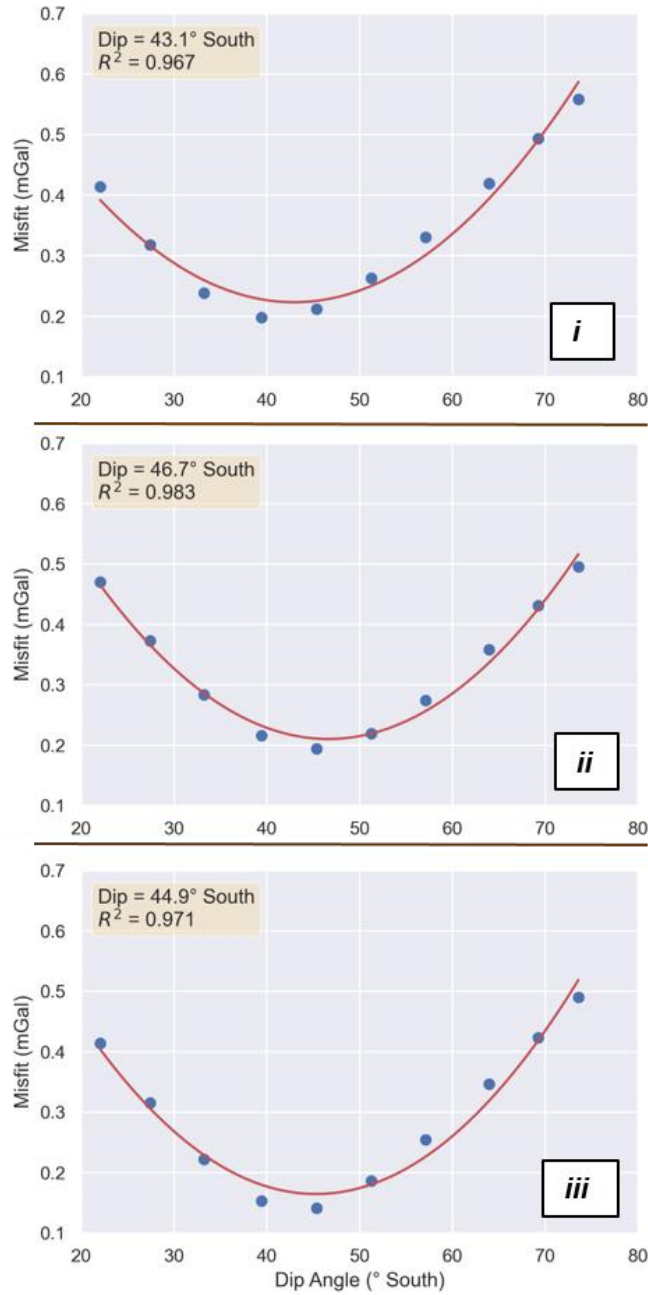


Figure 3.20. Misfit as function of the PDF dip angles in the Matheson profile for three different contaminated data sets.

Three of the four contaminated data sets shown in Figure 3.19-*i*, were fitted to forward models that had 10 dips between 22 and 74°. Each assigned model dip returned a different misfit. The dots in Figure 3.20-*i* show the misfits at each of these dips for one noise corrupted dataset and Figures 3.20-*ii* and 3.20-*iii* are for two other datasets. The angle that has the lowest misfit is different in each panel of Figure 3.20, but is always one of the 10 angles. This angle can be estimated with greater precision by fitting a second-degree polynomial function to the misfit and the turning point of the polynomial is the angle with the least misfit. In Figure 3.20-*i*, the vertex is at an angle of 43.1° south, while the other two data sets have the dip angles corresponding to the best dip at 46.7° and 44.9° south. The low R^2 values listed on Figure 3.20 suggest that a second-order polynomial is an appropriate model for the misfit. For brevity, we are only showing the gravity modeling of section D-Matheson for four noise ensembles.

Table 3.2 – Estimated PDF dip angles for Val Gagne (B), Watabeag (C), and Matheson (D) transects.

Noised Data Set	B - Dip (°)	C - Dip (°)	D - Dip (°)
1	26.8	53.5	43.1
2	28.6	54.0	46.7
3	28.7	53.9	44.9
4	28.0	52.8	44.6
5	27.2	55.3	45.1
6	28.3	53.4	46.0
7	28.3	56.1	44.5
8	27.7	53.2	44.9
9	27.9	55.5	46.3
10	27.5	54.0	46.5
11	28.8	55.0	46.6
12	28.0	53.4	42.9
13	28.3	53.1	42.8
14	28.6	53.4	41.3
15	29.0	54.4	43.8
16	29.0	54.0	45.3
17	28.6	54.0	42.6
18	28.4	54.2	44.6
19	29.4	54.6	44.5
20	28.4	53.8	44.1
21	27.5	54.1	48.0
22	29.6	54.6	45.1
23	28.0	52.0	44.7
24	28.5	54.6	
25	27.6		
26	28.5		
27	30.1		
28	27.3		
29	29.3		
30	29.3		
Mean (μ)	28.4	54.0	44.7
Std. Deviaton (σ)	0.8	0.9	1.6

In Figure 3.20, the variation in the dip angles obtained for the fault below section D-Matheson gives a qualitative idea of the PDF dip angle uncertainty. However, just four

ensembles of noise-contaminated data sets are insufficient for confidentially estimating the fault dip and its uncertainty. Table 3.2 contains all the PDF dip angles obtained for the profiles. In the Val Gagne (B), Watabeag (C), and Matheson (D) profiles we used 30, 24, 23 ensembles of noise-corrupted data sets respectively to estimated the fault dips and its uncertainty with confidence. Our procedure was to keep increasing the number of ensembles until the variance of the estimate of the dip of the fault no longer changes substantially. Figures 3.21, 3.22 and 3.23, reveal the histogram of the dip angles listed in Table 3.2, which display what appears to be a normal distribution.

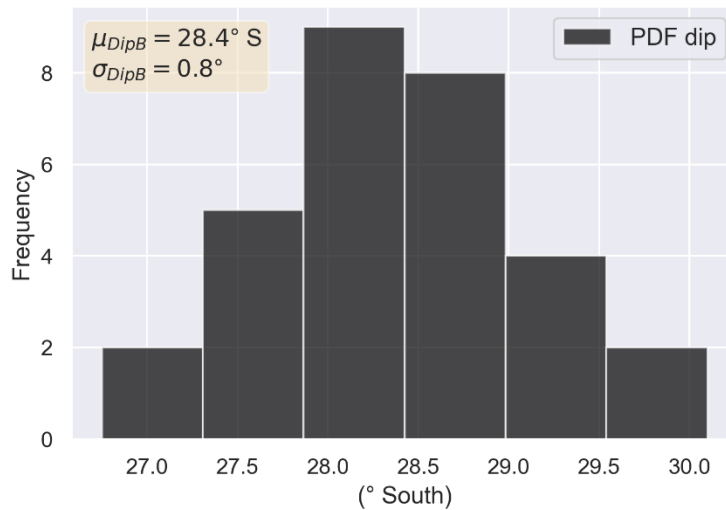


Figure 3.21. Histogram of the estimated dip angles for the Porcupine-Destor fault below the Val Gagne profile (B) as estimated from ensembles of noise-contaminated gravity data.

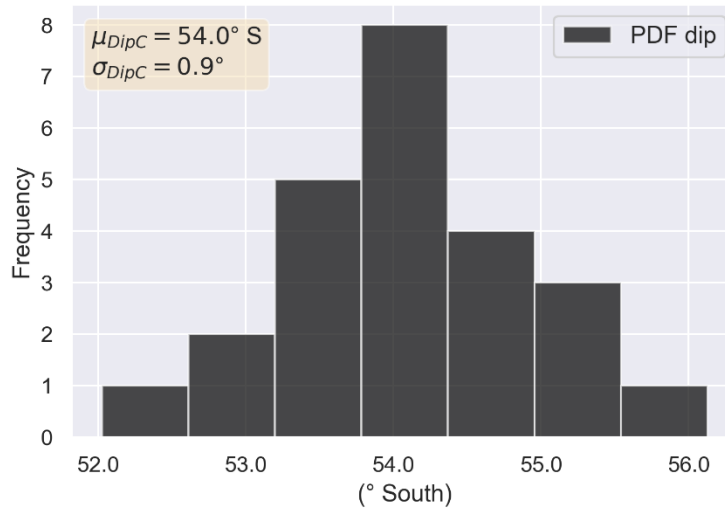


Figure 3.22. Histogram of the estimated dip angles for the Porcupine-Destor fault below the Watabeag profile (C) as estimated from ensembles of noise-contaminated gravity data.

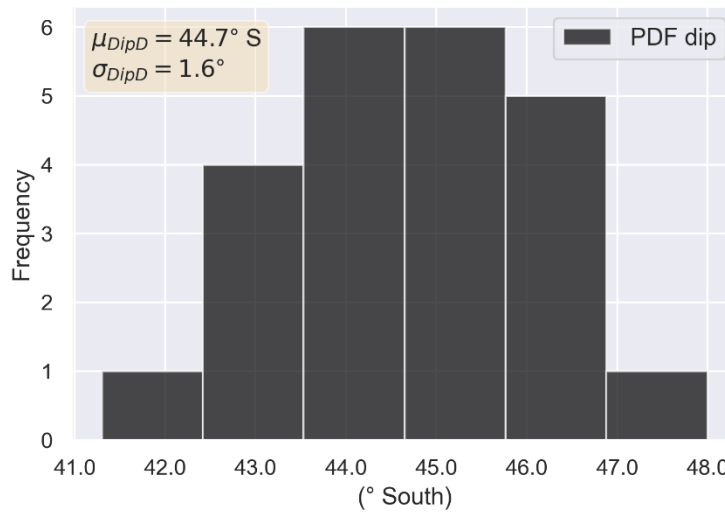


Figure 3.23. Histogram of the estimated dip angles for the Porcupine-Destor fault below the Matheson profile (D) profile as estimated from ensembles of noise-contaminated gravity data.

3.2.6. PDF Dip Angles at Matheson Area

Figure 3.24 shows the final results of the estimated dip of the Porcupine-Destor fault below the three modeled profiles. On this figure, the dips are only given to the nearest degree, as this is appropriate for the estimated uncertainties. The uncertainties are one standard deviation, and for normal distributions, we would expect that 66% of the estimated angles would lie within a range of two standard deviations (Bevington and Robinson, 1992). The PDF dip obtained for the Val Gagne, Watabeag, and Matheson profiles are therefore $28 \pm 1^\circ$ south, $54 \pm 1^\circ$ south, and $45 \pm 2^\circ$ south respectively.

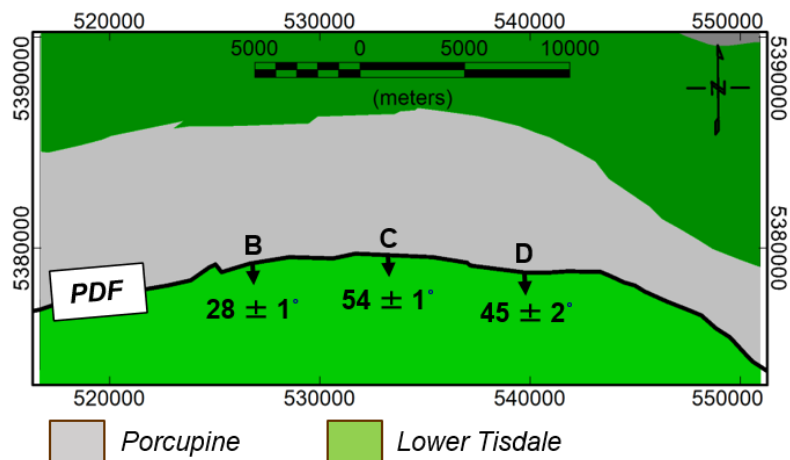


Figure 3.24. Porcupine-Destor fault estimated dip at Val Gagne (B), Watabeag (C), and Matheson (D) profiles.

Figure 3.25 is a graphical representation of the final models for the Val Gagne, Watabeag, and Matheson profiles. There is no vertical exaggeration, so we can visualize the geometric variation along the strike direction from the westernmost profile (top) to the easternmost profile (bottom). Clearly, the PDF is dipping at a much lower angle on the western profile (Val Gagne) in comparison to the other two sections.

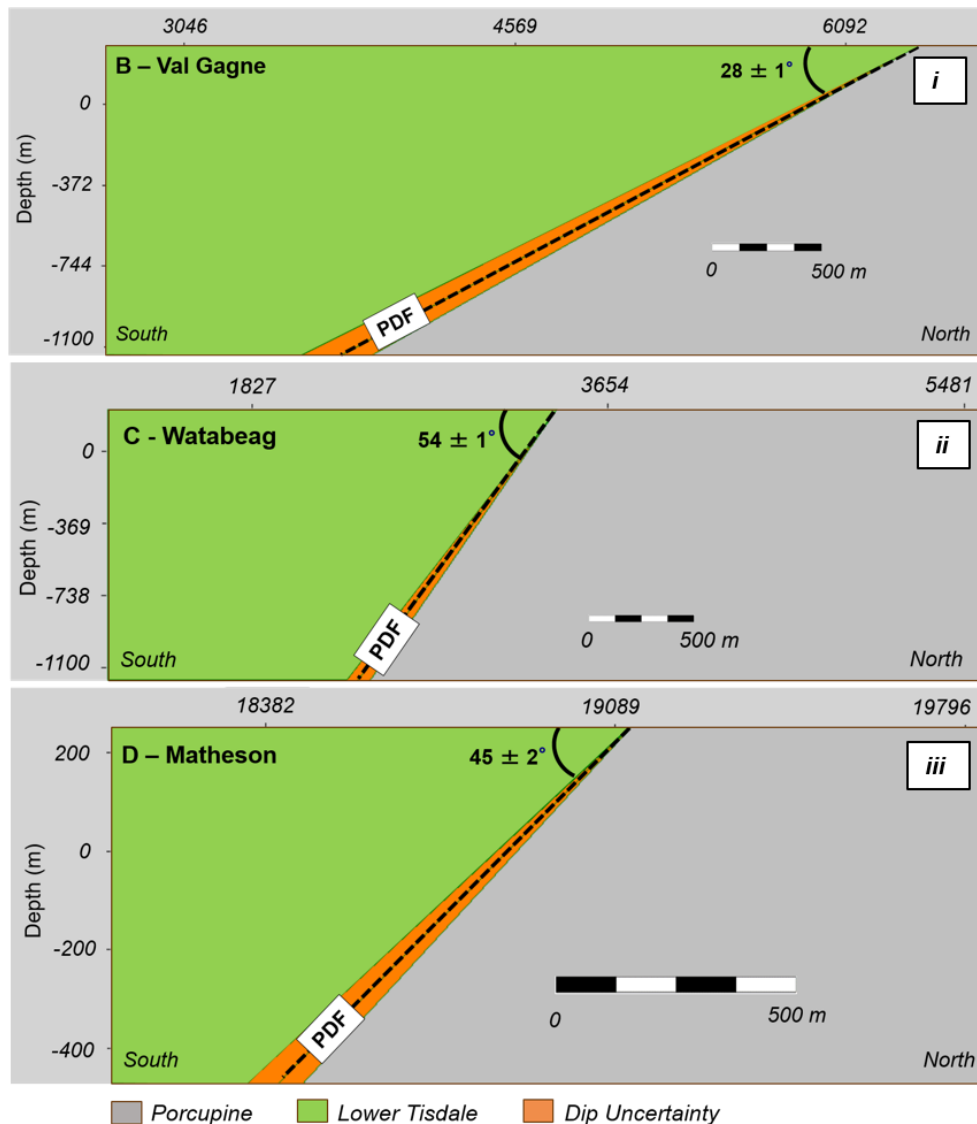


Figure 3.25. The estimated dip of the Porcupine-Destor fault and the corresponding uncertainty (one standard deviation is shown by the orange triangle) at the Val Gagne (B), Watabeag (C), and Matheson (D) profiles presented as cross sections (no vertical exaggeration).

Unlike Figure 3.25, which was a 2D view of the models, Figure 3.26 is a 3D visualization of the 2D PDF fault models. Although it does not represent a 3D model, this provides a 3D view of the PDF fault dip along the strike.

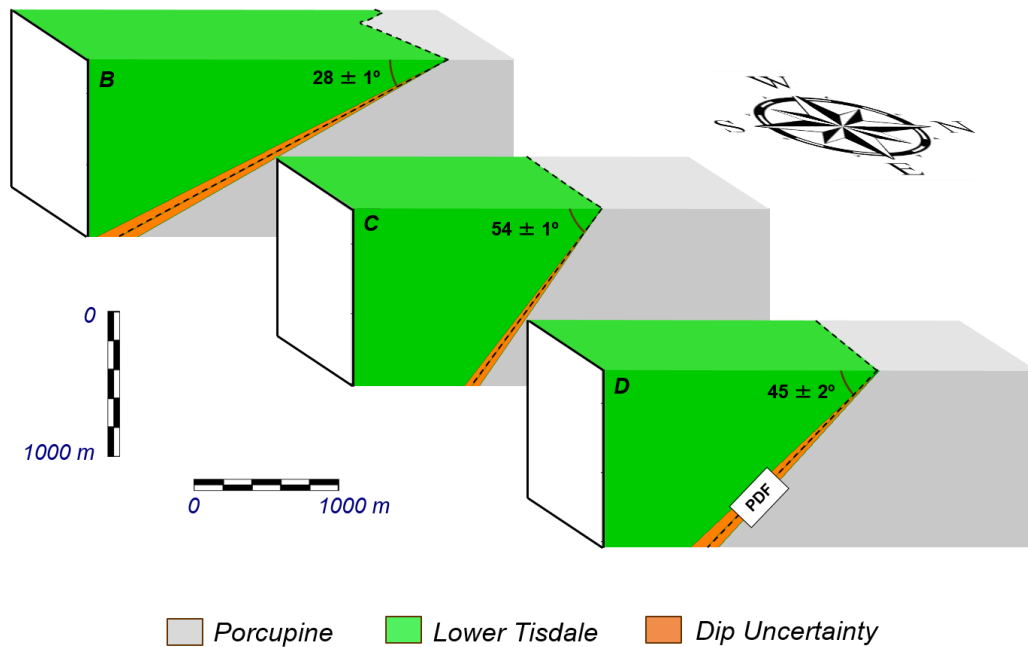


Figure 3.26. 3D visualization of the computed 2D models imaging of the PDF fault dip along the strike direction.

Given the assumptions to simplify the model and remove ambiguity we are able to use the gravity data uncertainties to infer that the uncertainties in the dip are from 1 to 2 degrees. This is a small uncertainty and allows us to conclude with greater certainty how an assumed linear fault is changing its dip along strike.

3.2.7. The Importance of Gravity Data Error estimation

The dip angle uncertainties might be higher in the general case as there are other uncertainties that we have not taken into account, these include (but are not limited to):

- Seismic data uncertainties: Information in seismic images is uncertain, for example, there is an uncertainty in the velocity estimation (Sergey and Landa,

2014; Bond, 2014), which will result in a depth error, when the two-way travel time is converted to a depth. The bottom of the Porcupine, as interpreted from the high-resolution seismic sections might therefore be in error (higher or lower).

- Density uncertainty: The modeling was also constrained by the density compilation assuming the density distribution within each assemblage is homogeneous. Nevertheless, heterogeneity is very common in most geological phenomena or processes (Khanfari et al., 2017). Our assumption of homogeneous geological units, will therefore introduce additional errors. Nonetheless, the histograms in Figures 3.12 and 3.13 suggest, that the Porcupine assemblage is more homogeneous, as the histogram is narrower and the standard deviation is smaller than they are for the Lower Tisdale assemblage.
- Linear fault plane: The assumption that the fault plane is linear, may add a bias or additional uncertainty to our analysis.
- Hidden layers/intrusions: Unknown layers, intrusions, etc. expected along major crustal structure with significantly different densities will also be a source of errors.

Acknowledging all of the above sources of uncertainties, means that our estimate of uncertainty is in doubt. However, quantifying these uncertainties is difficult. If they were not accounted for, then the uncertainty in the estimated dip would increase. These uncertainties could be thought of as equivalent, in some way, to a greater uncertainty in the reduced gravity data.

We can illustrate the importance of quantifying all these uncertainties by showing the impact that greater uncertainty in the reduced gravity data would have on our ability to model the data and achieve our interpretation objective. As an example, we will look

at the case when our measured data had a higher uncertainty, such as 1 mGal, which is common for regional data compilations provided by government agencies (Phillips et al, 1993). We have repeated the above process of noise-corrupting the data, but with noise with a 1 mGal standard deviation and estimated the mean dip of the PDF and the uncertainty in the estimate of this dip on the Matheson profile and found that the error was $45 \pm 41^\circ$, which is a much larger uncertainty. This implies that in this case the dip cannot really be determined with any certainty. This is evident on Figure 3.27, where the uncertain area, shown in orange covers nearly 90° , telling us no more than the fact that the fault dips to the south.

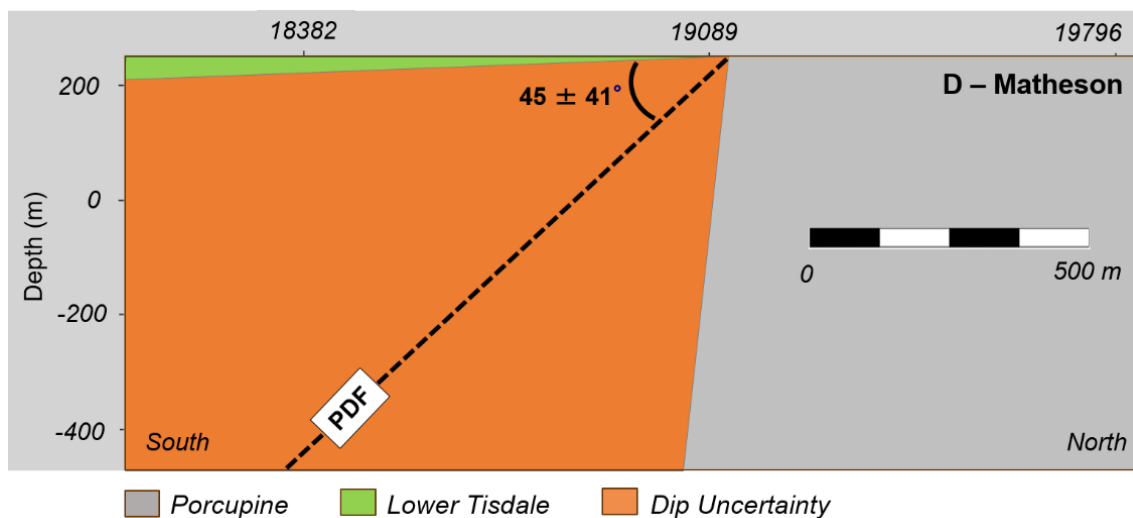


Figure 3.27 Porcupine-Destor fault dip (dashed line) and dip error standard deviation (orange zone) estimation for the Matheson profile. In this case, the estimation process was repeated with the noise ensembles for the measured gravity given a standard deviation of 1 mGal, a value typical for regional compilations.

3.2.8. The implications for Gravity Survey Planning and Specifications

One important consequence of our study is that we can outline a procedure for determining appropriate specifications for a gravity survey.

- 1) Define the geological problem to be solved in the model domain, such as estimating a specific source parameter such as the dip, depth, or density contrast of a feature to a desired uncertainty.
- 2) Generate some synthetic gravity data for that model.
- 3) Corrupt the synthetic data with an ensemble of noise with a specified noise level.
- 4) See if the source parameter can be estimated to the desired accuracy.
 - a. If the accuracy insufficient, reduce the specified noise level in step 3
 - b. If the accuracy is better than sufficient, then the specified noise level can be increased in step 3.
- 5) Once the appropriate noise level is determined, then the error propagation formula can be used to estimate the desired accuracy of the height estimation, terrain correction, etc.

Chapter 4: Determining the Variation in the Dip of the Structure Bounding a Successor Basin

The Abitibi greenstone belt (AGB), the location of which is shown on the right of Figure 4.1, contains some of the most important gold and base metal mining camps in Canada. Hence, a comprehensive knowledge of its geology has been acquired over the years (Monecke et al., 2017). Nonetheless, most of this understanding comes from mapping the surface geology and from drilling focused on prospective zones (Bateman et al., 2005). This study uses gravity and magnetic modeling to better understand the subsurface geometry of the Porcupine assemblage in the study area (shown as the thick grey package in the center of the left panel on Figure 4.1).

4.1. Geology

The Porcupine assemblage and the Lower Tisdale assemblage have been described in the previous chapter. In the study area, the Porcupine assemblage is bordered by mafic to intermediate metavolcanic rocks (depicted as light green on Figure 4.1). To the south is the Lower Tisdale assemblage, and to the north is the Kidd-Munro assemblage, which was not discussed in detail in Chapter 3. The Kidd-Munro assemblage (2717 to 2711 Ma) is dominated by tholeiitic mafic and komatiitic rocks with localized tholeiitic felsic volcanic rocks and graphitic sedimentary units (Ayer et al., 2007). The boundaries of the Porcupine assemblage are major faults: The Kidd-Munro assemblage to the north is separated from the Porcupine assemblage by the Pipestone

Fault (PSF), while the Lower Tisdale assemblage is separated from Porcupine assemblage to the south by the Porcupine-Destor fault (PDF) (shown on Figure 4.1 with blue and red dashed lines respectively). The PDF zone, discussed in the previous chapter, is associated with a number of gold deposits (Monecke et al., 2017). Therefore, a better understanding of the subsurface geometry of the Porcupine metasedimentary assemblage also might provide an improved understanding of those two important faults and their gold prospectively.

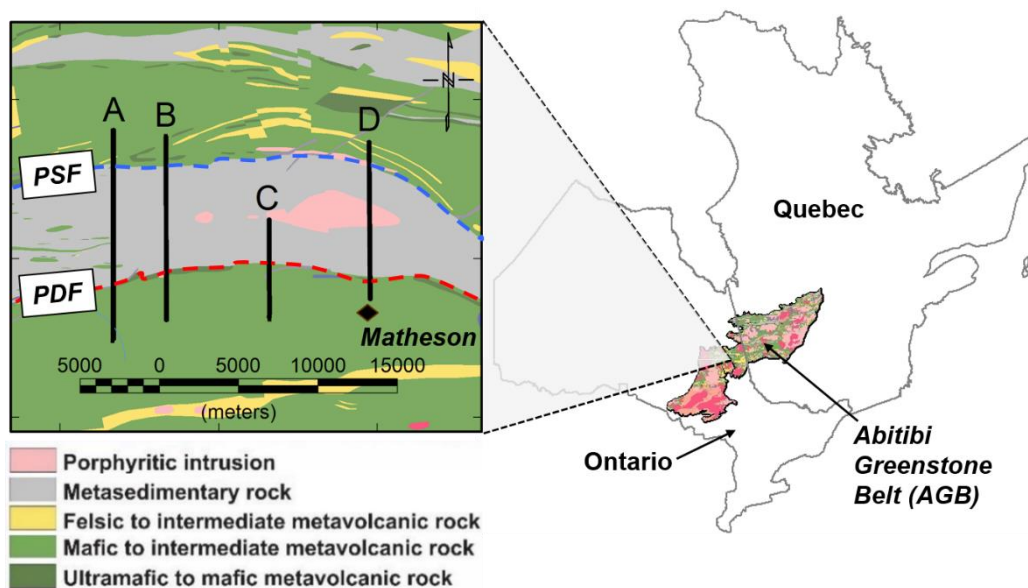


Figure 4.1. The location of the Abitibi greenstone belt on the Ontario and Quebec map on the right and the geological map of the study area on the left. The black lines are the location of seismic transects where the gravity data have been modeled (A - Shillington line, B - Val Gagné line, C – Watabeag line, and D – Matheson line). The Porcupine-Destor (PDF) and Pipestone (PSF) faults are shown with red and blue dashed lines respectively. (Modified after Montsion et al., 2018).

4.2. Model Constraints

In order to minimize the non-uniqueness of the models, petrophysical data, the bedrock geology map, as well as high-resolution seismic sections were used to constrain the models. Non-uniqueness occurs because the fundamental characteristics of an anomaly, *i.e.* amplitude and wavelength that together control the gradients of the flanks of the anomaly, can be reproduced by many different combinations of the source's location, geometry and its physical property contrast (Dentith and Mudge, 2014). Hence being able to specify as many of these parameters as possible will reduce the non-uniqueness.

4.2.1. Petrophysical Data and Surface Geology Map

The study area is largely covered with glacial overburden, so the geological map is a compilation (Montsion et al., 2018) of the bedrock geology and the densities are from a database compiled as part of the Metal Earth project (Eshaghi et al., 2018).

Even though a more detailed bedrock geology map is available in the study area as shown in Figure 4.1, a simplified map (Ayer et al., 2005) that reflects the large-scale changes in rock density was used to constraint the geology immediately below the overburden, hereafter termed the “surface geology” (Figure 4.2).

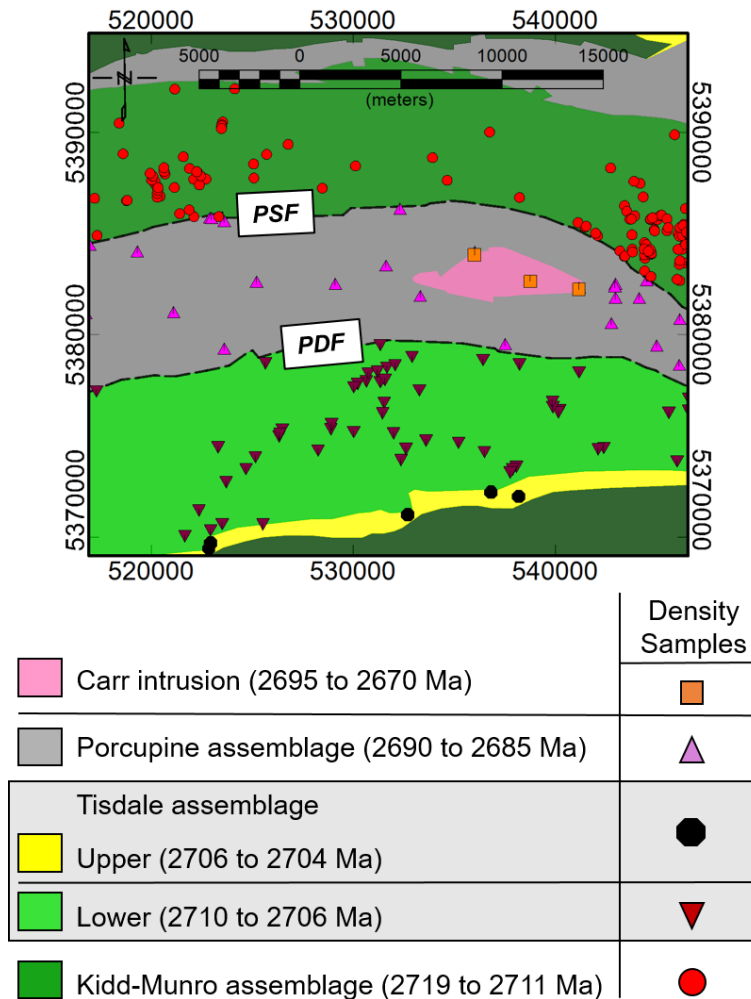


Figure 4.2. Simplified surface geology map (modified after Ayer, 2005), using slightly different colors than Figure 4.1. Also shown are the locations of samples with associated density measurements. Different location symbols are used for each geological unit, as shown in the legend. Some symbols might be indicating the location of more than one sample.

As aforementioned, the three main geological units present in the Porcupine assemblage study area (PASA) are the Lower Tisdale, Kidd-Munro, and Porcupine assemblages (Figure 4.2). Nonetheless, there are at least two more units, which have a significant gravitational effect on some of the models, and therefore should be take into

account. These two units are the Carr intrusion and the upper part of the Tisdale assemblage (Upper Tisdale), shown in pink and yellow on Figure 4.2. The dark green unit to the extreme south is ignored, as it has minimal effect on the gravity response.

The upper part of the Tisdale assemblage (Upper Tisdale) ranges in age from 2706 to 2704 Ma. It is dominated by calc-alkaline felsic to intermediate volcanic rocks including amygdaloidal flows, heterolithic debris flows and volcanoclastic sedimentary rocks (Ayer et al., 2005). The upper Tisdale assemblage conformably overlies the lower Tisdale assemblage.

The Metal Earth (ME) petrophysical compilation provided 35 density samples for the Upper Tisdale assemblage. They are geographically distributed as shown in Figure 4.2 with black circles. The mean density value for all the samples in this assemblage is equal to $2.76 \pm 0.05 \text{ g/cm}^3$ (see Figure 4.3), where the error is one standard deviation from the mean.

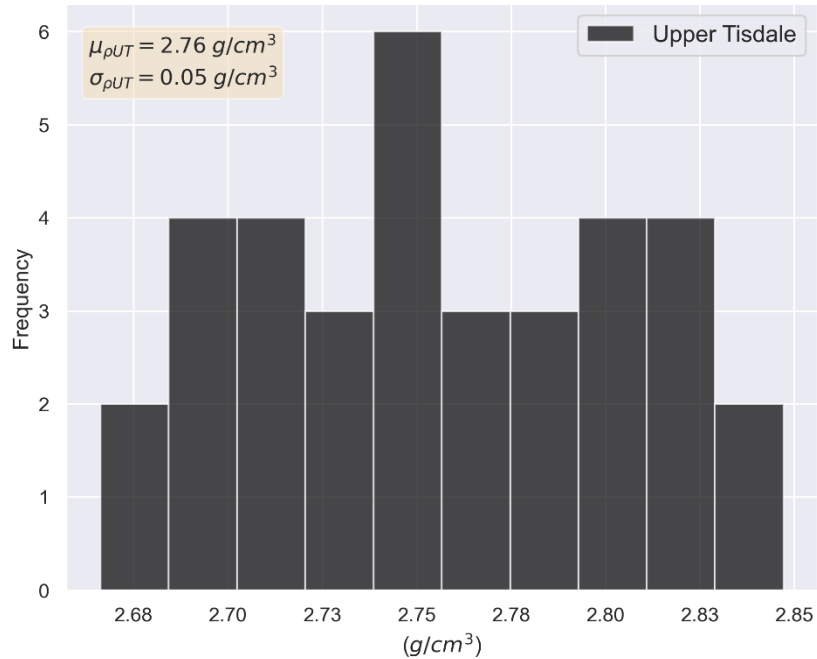


Figure 4.3. Histogram of the measured density values of the upper part of the Tisdale assemblage with the mean ($\mu_{\rho UT}$) and the standard deviation ($\sigma_{\rho UT}$) on the top left of the figure.

The Porcupine sedimentary assemblages are intruded by the Carr complex (Vaillancourt, 2001), which is predominantly comprised of tonalite to granodiorite (Ayer et al., 2005) as shown in the Figure 4.2. Although the ME compilation has only 11 density samples for this intrusion, the measured values seem to show a low variance, as shown in Figure 4.4, with the mean and standard deviation estimated being $2.69 \pm 0.02 \text{ g/cm}^3$.

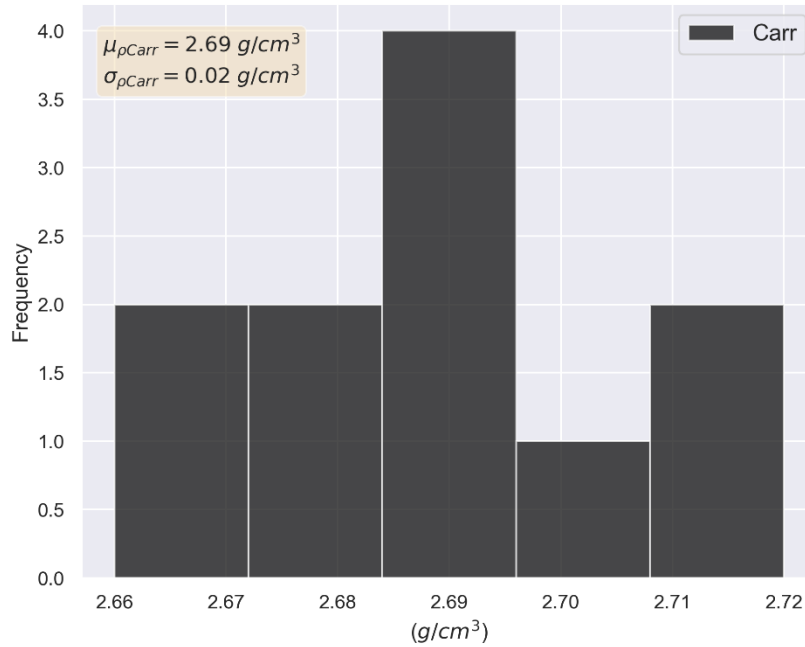


Figure 4.4. Histogram of the measured density values of the Carr intrusion, with the mean ($\mu_{\rho_{Carr}}$) and the standard deviation ($\sigma_{\rho_{Carr}}$) shown top left.

The densities for the Kidd-Munro assemblage were also not discussed in Chapter 3. This assemblage has an especially large number of density measurements in the project compilation (red circles in the Figure 4.2). It contains 343 samples, with a mean and standard deviation of $2.90 \pm 0.13 \text{ g/cm}^3$.

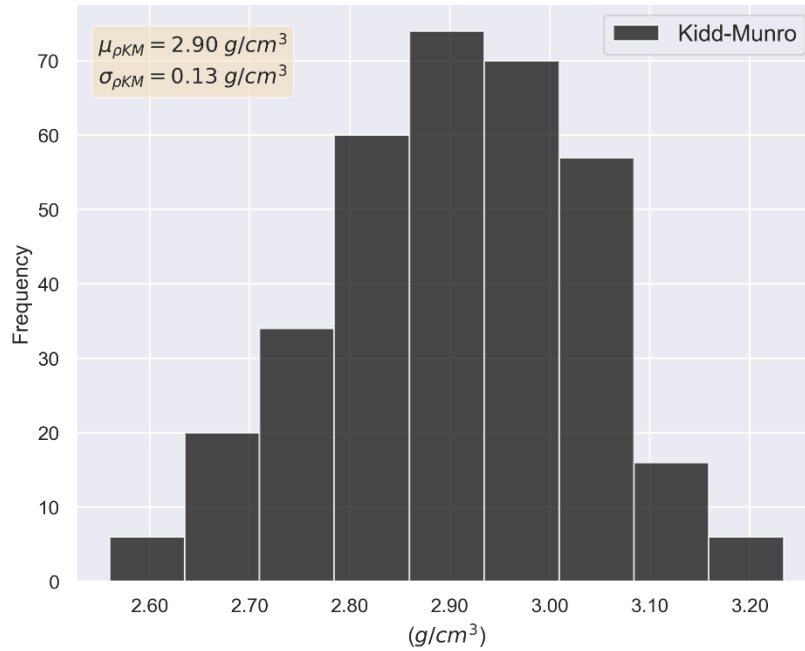


Figure 4.5. Histogram of the measured density values of the Kidd-Munro assemblage, with the estimated mean ($\mu_{\rho_{KM}}$) and standard deviation ($\sigma_{\rho_{KM}}$) shown in the top left.

The Table 4.1 summarizes the representative density values used in this study. The values have been reported either in Chapter 3 or in this current chapter.

Table 4.1. Data summarizing the density measurements: the mean, standard deviation from the mean, as well as the number of samples.

Assemblage/Intrusion	Mean Density (g/cm ³)	Standard deviation (g/cm ³)	N ^o of samples
Carr	2.69	0.02	11
Porcupine	2.73	0.04	46
Upper Tisdale	2.76	0.05	35
Lower Tisdale	2.89	0.10	90
Kidd-Munro	2.90	0.13	343

4.2.2. High Resolution Seismic Sections

Four high-resolution seismic reflection profiles were utilized to help construct the initial model (Figure 4.6), as these provide high-resolution images of the reflective structures of shallow dipping within the crust. The Shillington seismic line (traverse A) data was acquired during the Discover Abitibi initiative and the other three: Val Gagné, Watabeag, and Matheson (traverse B, C, and D, respectively), were part of the Metal Earth project (Snyder et al., 2009; Naghizadeh et al., 2019). All the seismic profiles were acquired using Vibroseis sources. The specifications of the Metal Earth high-resolution seismic surveys are provided in Chapter 3, but the Shillington high-resolution line was not discussed in that chapter. This line used converted-wave (P–S) processing as it contained shallow, laterally continuous structures defined by high-amplitude reflections (Snyder et al., 2009). The geophones for this line were spaced every 12.5 m and the sources were spaced every 25 m; the frequency sweep for the data was 10 to 160 Hz (Reed et al., 2005).

Figure 4.6 shows the four seismic sections, converted to depth sections assuming an average rock velocity of 6000 m/s (Reed et al., 2005; Naghizadeh et al., 2019). In addition, the surface geology is displayed on the top of the sections using the colors specified in Figure 4.2. As Figure 4.2 does not show the location of the lines, the simplified geology and line locations are shown in Figure 4.7.

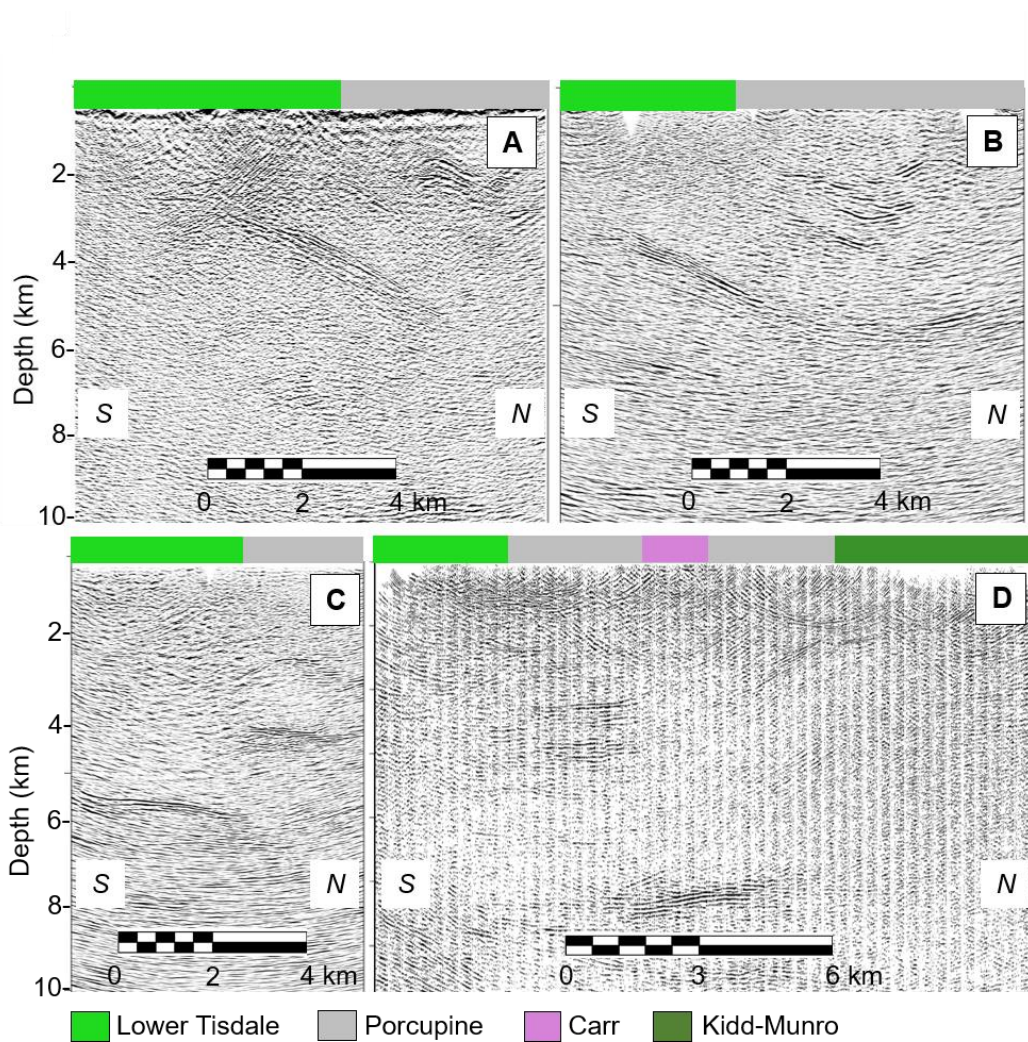


Figure 4.6. Seismic sections to guide construction of the density model for traverses A (Shillington line), B (Val Gagné Line), C (Watabeag line), and D (Matheson Line). On the top of the seismic sections, the color indicates the surface geology using the legend of Figure 4.2.

The length of the Discover Abitibi Shillington line is 10 km, while the length of ME seismic lines is roughly 10 km, 6 km, and 15 km for Val Gagné, Watabeag and Matheson, respectively.

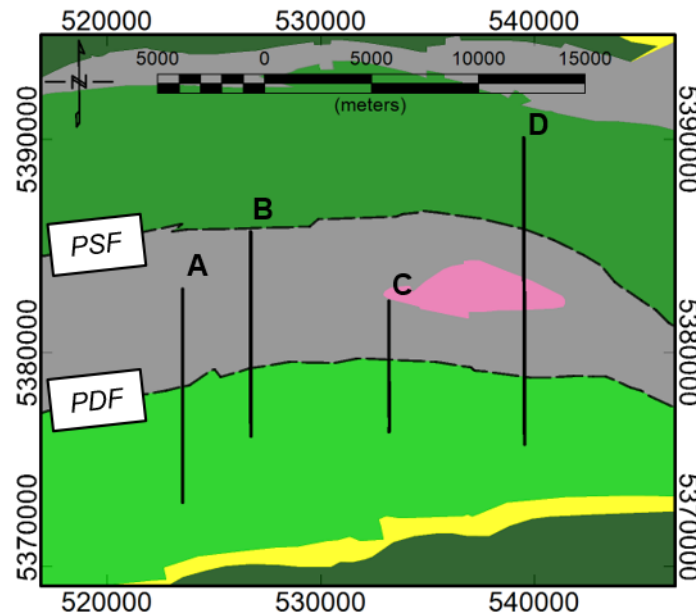


Figure 4.7. Location of the seismic lines, the sections from which are shown in Figure 4.6, overlain on the simplified geology. For the color legend, see Figure 4.2.

4.3. Gravity and Magnetic Data

Gravity data and magnetic data have been acquired/compiled as part of the geophysical component of the Metal Earth (ME) project.

4.3.1. Gravity Data

The ME gravity data was acquired in the 2018 field season along the Val Gagné (traverse B), Watabeag (traverse C), and Matheson seismic lines (traverse D).

The specifications of the ME gravity survey were described in the Chapter 3. The gravity data along the Shillington line (traverse A) and areal coverage in the rest of the PASA was obtained from the CGDB gravity compilation (Natural Resources Canada, 2016).

The data acquired by ME and the CGDB compiled measurements were processed and corrections were applied to remove unwanted variations associated with changes in latitude and elevation and then a terrain correction was made to calculate the final “complete Bouguer anomaly”. These corrections were applied using Oasis Montaj® (geosoft.com/products/oasis-montaj). These point gravity data were used to generate the gravity grid for the PASA, shown in Figure 4.8-*i*. Figure 4.8-*ii* shows the same gravity map, however the grid values were classified qualitatively into high medium and low ranges and indicated as partially transparent black, grey and white shaded areas on the map. Underneath these shaded areas is the simplified geology and there is clearly a correlation between the lows and the Porcupine assemblage.

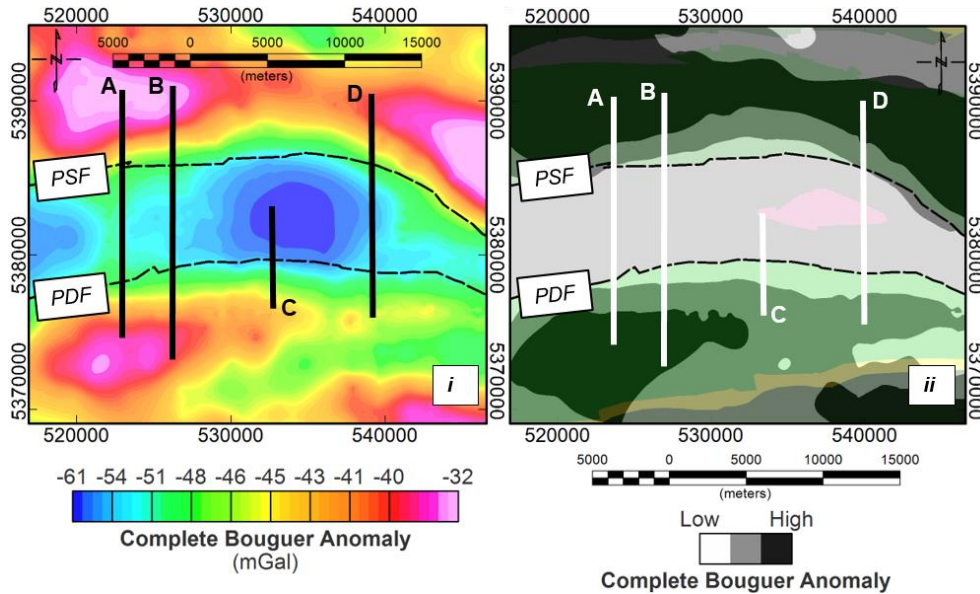


Figure 4.8. Gravity grids and the four gravity profile traverses (A to D). On the left (i), the complete Bouguer anomaly map is displayed as a color image, while on the right (ii) it is shown as a qualitative transparent greyscale image with the geology map underneath. The data was obtained for the Metal Earth project and from the Canadian Gravity Database compilation.

The ME data uncertainties were estimated for the measurements and the data reduction steps using the error propagation equation as described in the previous chapter. The final uncertainty in the complete Bouguer anomaly for Metal Earth data was 0.120 mGal.

Figure 4.9, shows the locations of the ME stations as blue inverted triangles and the locations of the stations in the CGDB are shown with black diamonds. The station spacing for the CGDB is variable, being as close as 100 m along the Shillington line (rectangle A), a few hundred meters along other roads and 1.5 km or more in the surrounding areas. The uncertainty of the data in the CGDB compilation data is not

provided and therefore 1 mGal error was used to avoid underestimation. The ME data have been extended further to the north and south using the CGDB data where appropriate, with the brown rectangles enclosing all the data included in the modeling

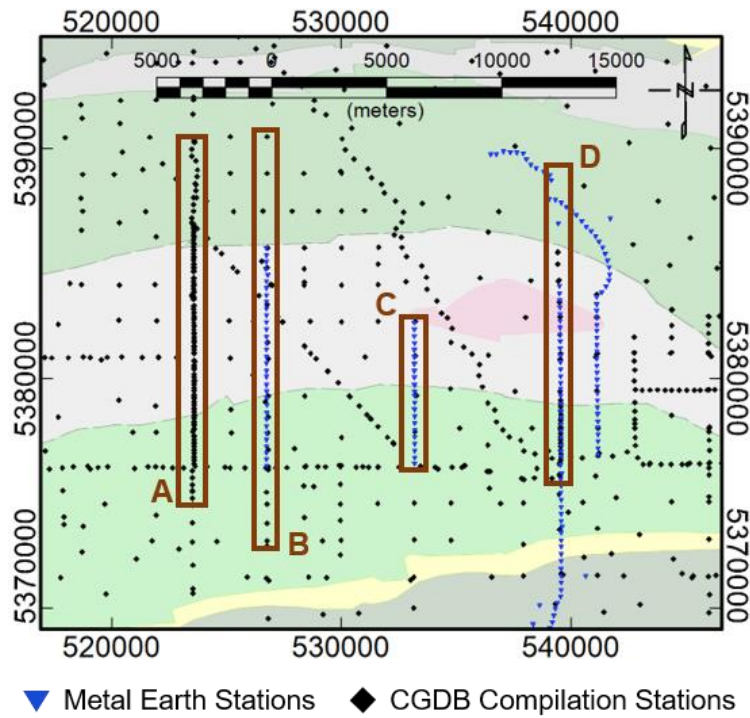


Figure 4.9. Gravity station locations, showing ME data (in blue) and CGDB data (in black), overlaying the surface geology map in the PASA. The locations inside the brown rectangles are the gravity stations, which were used when modeling the data.

4.3.2. Magnetic Data

The magnetic data were compiled from two Ontario Geological Survey (OGS) data sets: Geophysical Data Set 1055 (Ontario Geological Survey, 2005) and Geophysical Data Set 1102 (Ontario Geological Survey, 2000) and merged to create a single magnetic grid over the study area (Figure 4.10). Although these two data sets are from different airborne surveys, the specifications are similar: the flight line spacing was 200 m, the nominal terrain clearance was about 70 m, and the nominal aircraft speed was about 70 m/sec, which provided 1 sample every 7 meters as the sensor sample rate in both cases was 10 samples per second.

The magnetic data (Figure 4.10) does not clearly show all the lithological contacts in the PASA, with most of the magnetic anomalies present in the area interpreted to be associated with mafic dikes, either Matachewan, Biscotasing, or Abitibi dike swarms (Berger et al., 2010).

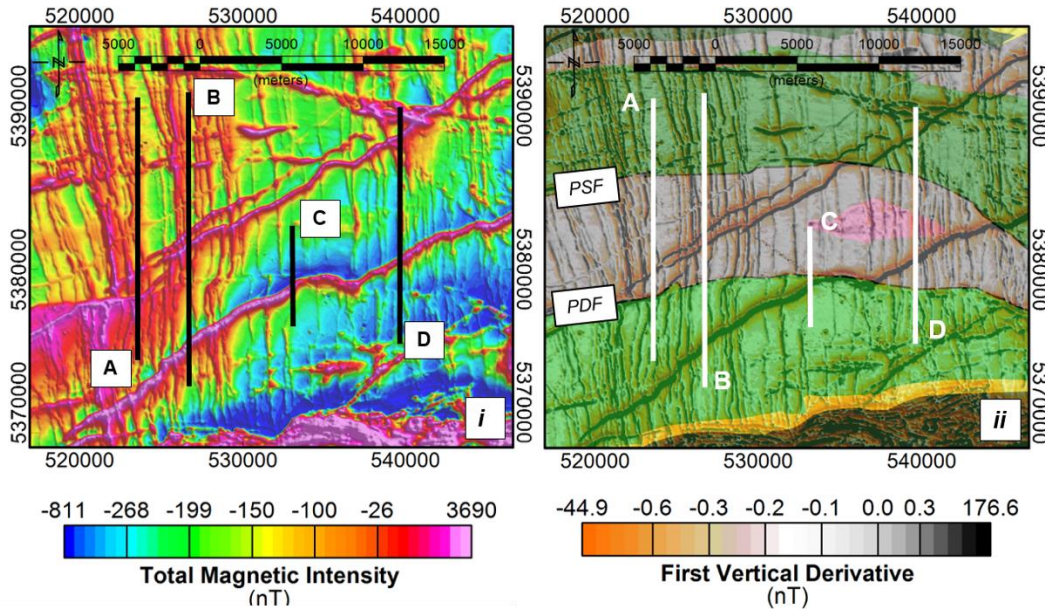


Figure 4.10. Total magnetic intensity (TMI) grid of the PASA. The left is a color image, with the lows cool (blue) colors and the highs hot (red). On the right, the surface geology map is overlaid by the first vertical derivative of the TMI grid, strong negatives red and strong positives black. The data was obtained from the two Ontario Geological Survey data sets mentioned in the text.

The Matachewan and Biscotasing Paleoproterozoic mafic intrusive dikes are composed of gabbro and quartz gabbro (Berger et al., 2011). The Matachewan swarm is dated about 2476 Ma, whereas the Biscotasing swarm has been dated at 2166 Ma (Osmani, 1991). The Matachewan dike swarm occurs in a north-striking direction, while the Biscotasing dike swarm has been mapped as northeast striking.

Halls et al. (2005) indicated that Matachewan dikes are dominantly Fe-rich tholeiites with relatively low zirconium content and they cannot easily be discriminated geochemically from the other dike swarms. Geological studies have suggested the Matachewan dikes occur in two phases (Berger et al., 2011). The older phase is aphyric

and generally weathers dark green, black or orange brown and has minor quartz, magnetite and/or ilmenite, and secondary white mica and chlorite. The younger phase of the Matachewan dike swarm contains prominent white or light green plagioclase phenocrysts that comprise 1 to 50% of the rock and are from 5 to 50 mm in size.

The Biscotasing dikes are poorly exposed and hence they are poorly documented and understood and are easily confused with dikes of the Matachewan swarm. Although the strike is usually different, the best way of distinguishing between the two swarms is through geochronology (Berger et al., 2011).

The Abitibi dike swarm, dated at approximately 1140 Ma, is also northeast striking and crosscuts all the supracrustal rocks in the study area. These Mesoproterozoic mafic intrusive rocks are composed of medium to coarse-grained olivine gabbro to monzodiorite (Osmani, 1991). Halls et al. (2005) indicated the Abitibi dikes are compositionally distinct from other dikes presents in the study area, containing less than 45% SiO₂, low nickel, chrome and significantly higher TiO₂ plus high Zr/Y and La/Yb ratios compared to other dike swarms. Olivine and pyroxene define the essential mineralogy, whereas magnetite, apatite and rare biotite are accessory minerals (Berger et al., 2011).

Although the Biscotasing and Abitibi dike swarms have been mapped as northeast striking, only the latter is believed to be crosscutting the model profiles. One Biscotasing dike is located a few kilometers south of the Matheson traverse and is highlighted with a light blue line in Figure 4.11. Some of the Abitibi dikes have a strong magnetic signal (highlighted in black in Figure 4.11), while another dike, indicated with a dashed black line, has a weaker magnetic signal.

There are several other magnetic lineaments evident in the PASA. In Figure 4.11, these lineaments are not identified; however, numerous north-striking features are apparent in the western portion in the map. The first vertical derivative of the magnetic data clearly delineates these features and they might be associated with the Matachewan dike swarms. As these structures are located parallel to the model profiles, and are not apparent in the gravity maps (Figure 4.8) they have been excluded during the gravity modeling.

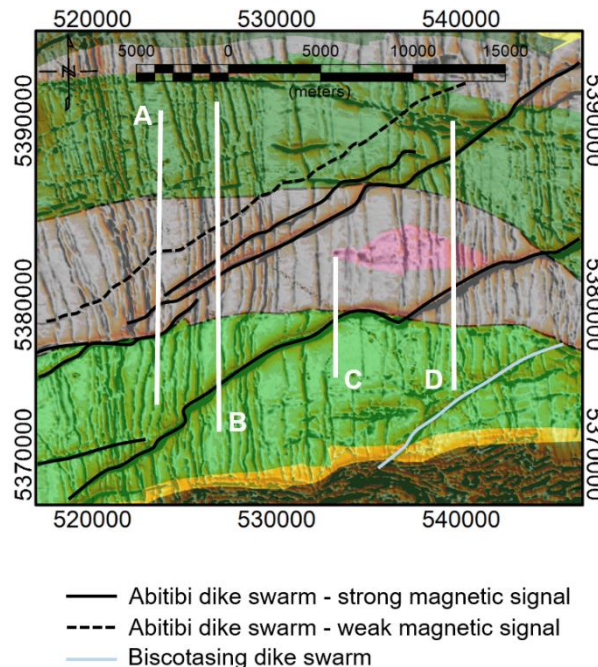


Figure 4.11. Interpreted dikes from the magnetic grid based on Berger (2010). The magnetic grid and geological map are the same as those shown in Figure 4.10-ii.

4.4. Forward Modeling

Gravity data along the profiles were modeled with the 2D forward modeling program GM-SYS. This process involves the user manually adjusting the model

parameters until the predicted data and the measured data agree to within the uncertainty level of the data. Magnetic data were solely used to locate the mafic dikes and their dip were not estimated. High-resolution seismic sections (shown at the bottom of Figures 4.13-iii, 4.15-iii, 4.17-iii, 4.19-iii,) were interpreted and used to help construct the initial model. Only profiles C and D have seismic data along the complete profiles; profile A only has seismic data in the southern part and profile B only has data in the central part. The parts of the profiles with seismic data are shown with the blue rectangle and white infill on Figure 4.12, while those parts with no seismic data are shown as solid blue. The profiles locations (and length) were selected bearing in mind the gravity and seismic data coverage and the geological features that are to be resolved.

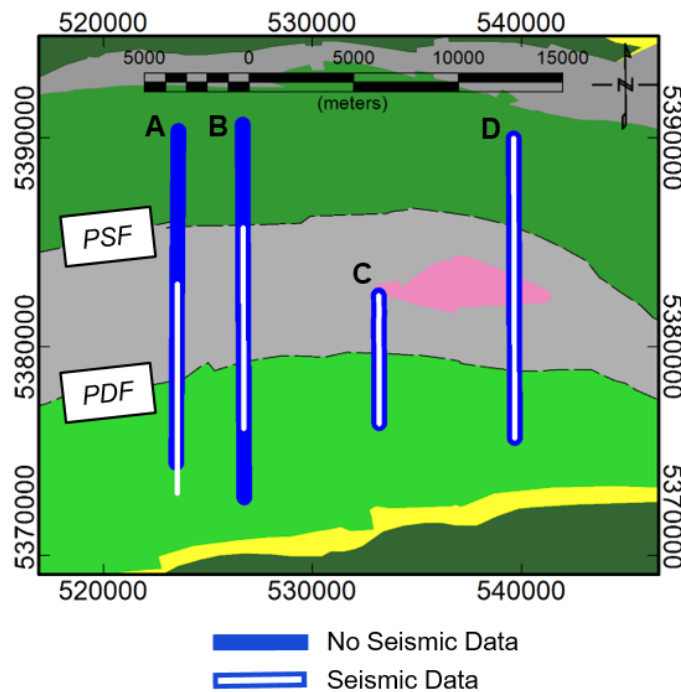


Figure 4.12. Location of the forward-modeling profiles highlighting the locations of the seismic sections (blue with white infill). While in C and D the seismic lines entirely cover the model lengths, in A and B there is only partial coverage.

4.4.1. Shillington Line Model (Profile A)

On this profile, three different lithologies are resolved (Figures 4.13-*ii* and 4.14) based on the gravity (Figure 4.13-*i*) and magnetic response. Gray colors indicate the metasedimentary unit (the Porcupine assemblage); light and dark green depicts the mafic to intermediate volcanic units (the Lower Tisdale and Kidd-Munro assemblages respectively) and black shows two of the Abitibi mafic dikes. Due to the low magnetic contrast between the geological units (See Figure 4.10), the magnetic data was only used to model the dikes, which have strong anomalies on the magnetic grid (Figure 4.14).

On the seismic section, the strongest reflector is indicated with a dashed line dipping to the north. This has been interpreted as the contact at the base of the Porcupine assemblage, with the Lower Tisdale below. The two main faults in the study area, the Porcupine-Destor Fault (PDF) and Pipestone fault also have been interpreted in this modeling. The reflector interpreted as the PDF is weakly evident in the seismic section dipping southward 30 – 40 degrees. The PSF is north of the Shillington seismic profile. Nevertheless, using the potential-field data the PSF has been modeled as a sub-vertical fault, which is identifiable due to the density contrast between the Porcupine and Kidd-Munro assemblages. However, due to the non-uniqueness of gravity modeling, there is some uncertainty in the precise angle of the dip.

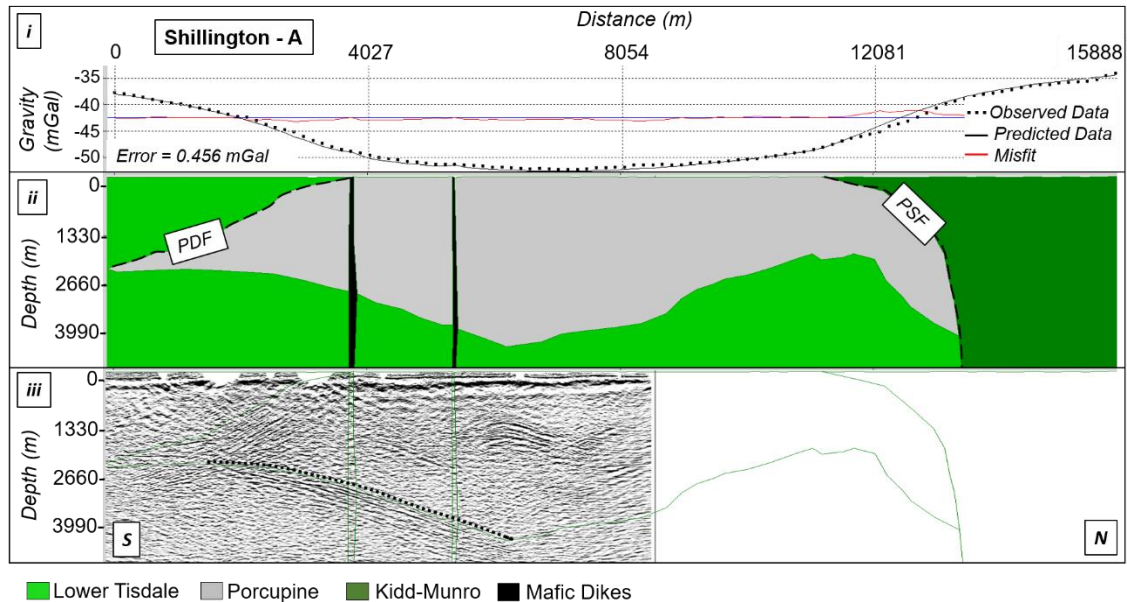


Figure 4.13. The Shillington line modeling showing the measured and predicted gravity data and the difference between these (red line) (i), the geological model with the units indicated by the color legend at the bottom of the figure and the modeled fault localizations shown with dashed lines (ii), which are also shown in green on the interpreted seismic section (iii). South is to the left, north to the right.

In Chapter 3, the fault was assumed to be linear, which can result in an increase in the misfit if the fault is not linear. In this chapter, with the aim of getting as small a misfit as possible, the fault is broken into a number of smaller piecewise linear sections, by adding vertices between the linear sections. This is possible as in Chapter 3, only profiles 2 or 3 km in length were modeled, but in this chapter, the profiles are longer. Using this approach, the Porcupine-Destor fault at the Shillington line had 16 vertices added and the

dip angle in the linear sections between the vertices varies with depth, ranging from 19 to 37 degrees southward. The average dip of the PDF is 30 degrees. The root-mean-square misfit is 0.456 mGal for the forward gravity modeling (with the point-by-point misfit being shown with the red line on Figure 4.13-*i*).

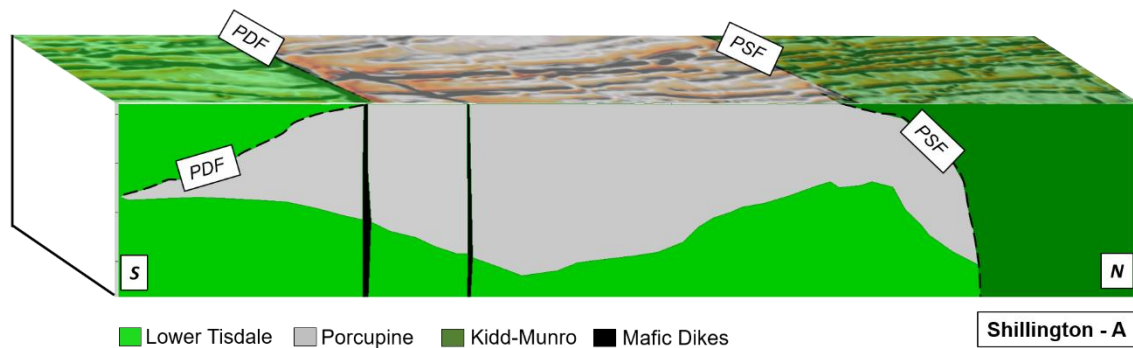


Figure 4.14. The 3D visualization of the Shillington line model (profile A), also shown in 2D in Figure 4.13-*ii*. The first vertical derivative of TMI, which is overlaying the surface geology, is displayed on the top to highlight the dikes at the surface.

4.4.2. Val Gagné Line Model (Profile B)

The same three lithologies are resolved in the Val Gagné model (Figures 4.15-*ii* and 4.16) based upon the gravity (Figure 4.15-*i*) and magnetic response (Figure 4.16): these lithologies are the Porcupine, Lower Tisdale and Kidd-Munro assemblages. However, due to the proximity of the Upper Tisdale assemblage, part of this unit was also incorporated (yellow unit in Figures 4.15-*ii* and 4.16) to explain the reduction in the gravity data at the southern most part of the line (Figure 4.15-*i*).

The geometry of the Porcupine obtained from profile B modeling is similar to that on profile A, except the geometry at the base of the Porcupine is different. This difference

is based on an interpretation of the seismic data (Figure 4.15-*iii*), which shows two strong reflectors (marked with dashed lines), which have been interpreted as the contact between the Porcupine and Lower Tisdale assemblages. These two reflectors present a contact-discontinuity. Other reflectors above these are interpreted as interfaces within the Porcupine assemblage

Unlike the Shillington seismic data, the Val Gagné seismic section shows no reflector that could be associated with the PDF. Like Shillington, the seismic data does not cross the PSF. Hence, the gravity data across these two faults have been modeled to infer south-dipping and sub-vertical structures for the PDF and PSF, respectively.

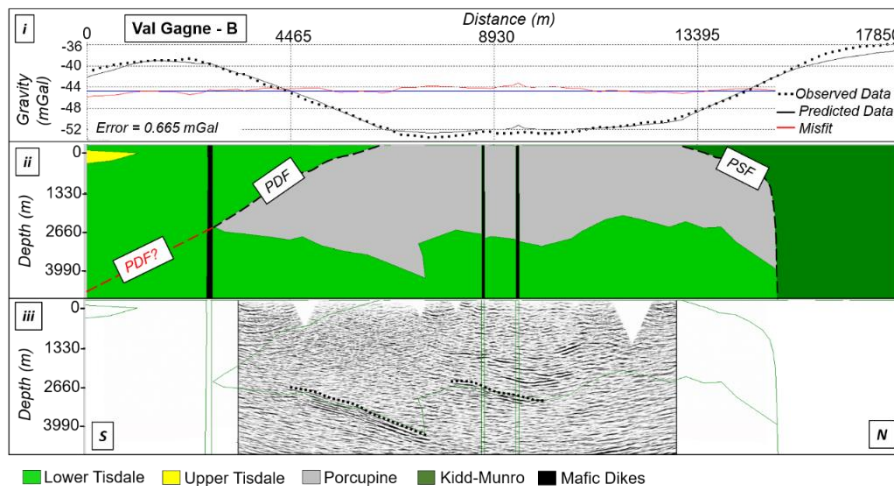


Figure 4.15. The Val Gagné line modeling showing the measured and predicted gravity data and the difference (red line) (*i*), the model itself showing the lithologies (colors are shown on the legend at the bottom of the figure) and the modeled fault localizations are shown with dashed lines (*ii*), and the interpreted seismic section (*iii*).

The dip of the Porcupine-Destor fault obtained from the gravity modeling for profile B varies from 24 to 37 degrees southward with 11 vertices added to resolve the fault geometry. The average value of the dip is equal to 30 degrees and the root mean square misfit is 0.67 mGal from the gravity forward modeling. The red line on Figure 4.15-*i* shows the point-by-point misfit).

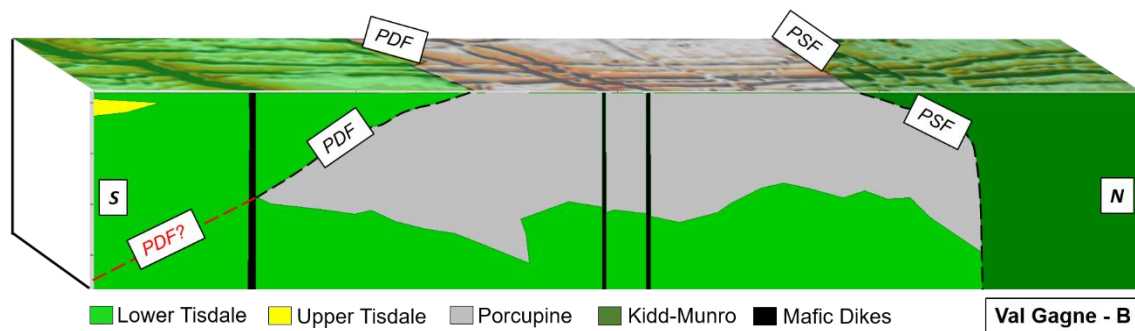


Figure 4.16. The 3D visualization of the Val Gagné line (profile B) model also shown in 2D in Figure 4.15-*ii*. The first vertical derivative of TMI, which is overlaying the surface geology, is displayed on the top to highlight the dikes at the surface.

4.4.3. Watabeag Traverse Model (Profile C)

The Watabeag model is shorter, due to the shorter length of the seismic section and the gravity profile coverage. Consequently, it is only able to resolve the PDF and the base of the southern part of the Porcupine assemblage. Hence only two assemblages have been resolved (the Porcupine and the Lower Tisdale), as well as the Abitibi dike (Figures 4.17-*ii* and 4.18). Again, the magnetic data was only used to model the dike, which has a strong anomaly on the magnetic grid (Figure 4.18).

Like the Val Gagné seismic data, any reflector that could be associated with the PDF, is not visible in the Watabeag seismic section (Figure 4.17-*iii*). A strong horizontal reflector has been interpreted as the base of the Porcupine. Incorporating this into the starting gravity model, the PDF fault has been modeled as dipping to the south.

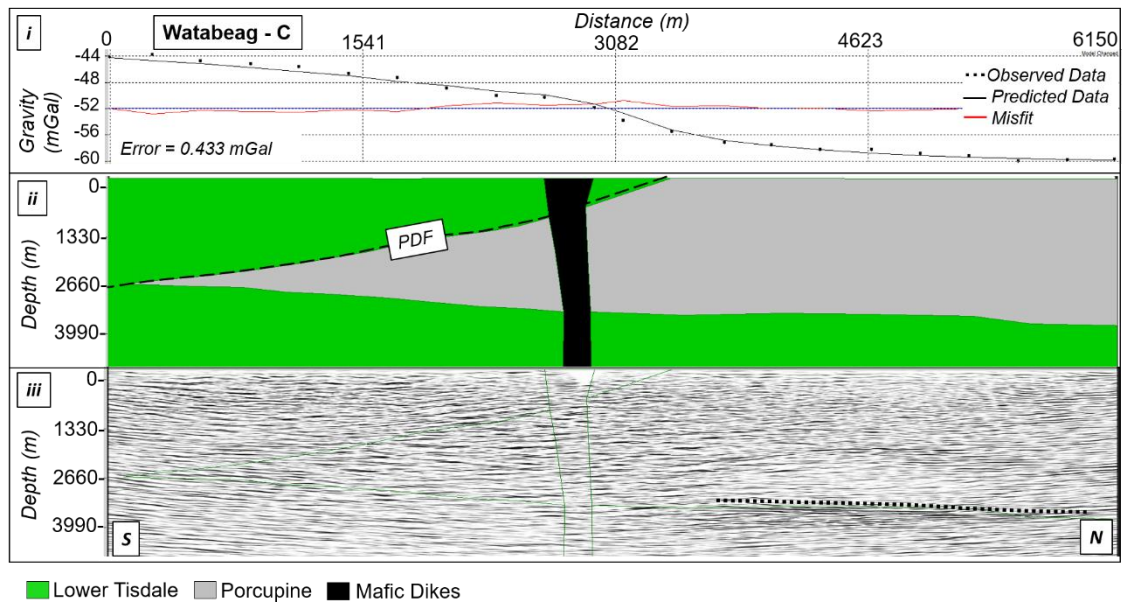


Figure 4.17. The Watabeag line modeling showing the measured and predicted gravity data and the difference (red line) (*i*), the model itself (with the lithologies indicated by the colors shown in the legend at the base of the figure) and the modeled PDF fault location is shown with the dashed line (*ii*), and the interpreted seismic section (*iii*).

The dip of the Porcupine-Destor fault obtained from the gravity modeling for profile C varies from 41 to 56 degrees southward using 12 vertex points. These points were added to resolve the fault geometry, which on average is equal to 49 degrees. The root

mean square misfit is 0.433 mGal for the forward gravity modeling. (See Figure 4.17-*i* for the misfit at each point shown with the red line).

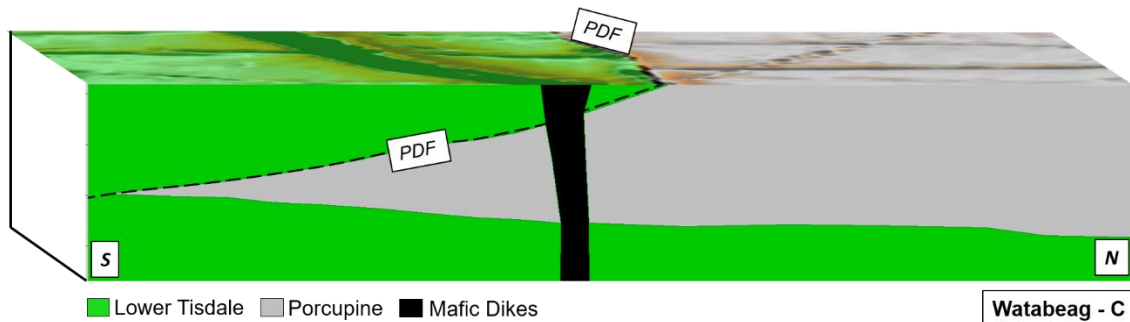


Figure 4.18. The 3D visualization of the Watabeag line model (profile C) also shown in 2D in Figure 4.17-*ii*. The first vertical derivative of TMI, which is overlaying the surface geology, is displayed on the top to highlight the dikes at the surface.

4.4.4. Matheson Traverse Model (Profile D)

In the Matheson model, four different lithologies have been resolved (Figures 4.19-*ii* and 4.20) based upon the gravity (Figure 4.19-*i*) and magnetic response. These are the Porcupine, Lower Tisdale, Kidd-Munro assemblages, and the Carr intrusion. As with the other three profiles, the magnetic data was only used to model the dikes, with two Abitibi mafic dikes being identified and shown in Figures 4.19-*ii* and 4.20.

The geometry of the Porcupine assemblage obtained on profile D is broadly similar to that on profile A and B, however the Porcupine assemblage's is thinner in this region of the PASA in comparison to the other models. This conclusion is based on two constraints. 1) The gravity low is roughly -9 mGal amplitude, compared with lows of about

-14 mGal on the Shillington and Val Gagné profiles. 2) The two horizontal reflectors indicated with the dashed line on Figure 4.19-*iii* are much shallower at a depth of about 1500 meters. The interpretation of these reflectors is somewhat problematic, due to the presence of several seismic artifacts, possibly noise associated with the Matachewan dike swarm, which strikes parallel to the profiles. These two reflectors have been interpreted as the Lower Tisdale-Porcupine contact (dashed lines in Figure 4.19-*iii*).

The dip of the PDF and PSF fault were constrained by the gravity data. These two faults have been modeled as south dipping and sub-vertical, respectively.

The pink porphyritic intrusion (Carr) in the center of the Porcupine assemblage has been given a shallow depth, as it is shown on the geology map, but its depth extent cannot be determined from the geophysical data as there is not a strong susceptibility or density contrast with the surrounding Porcupine assemblage.

Unlike the other lines, the Matheson line has a clear positive gravity anomaly interpreted to be related to the dike (Figure 4.19-*i*), so the dike has a higher density than the surrounding metasedimentary unit does, and possibly has a greater thickness than elsewhere. Although this gravity anomaly is subtle on the profile, it is a 1 mGal anomaly and hence many times higher than the estimated uncertainty for the ME data, so it can be interpreted confidently.

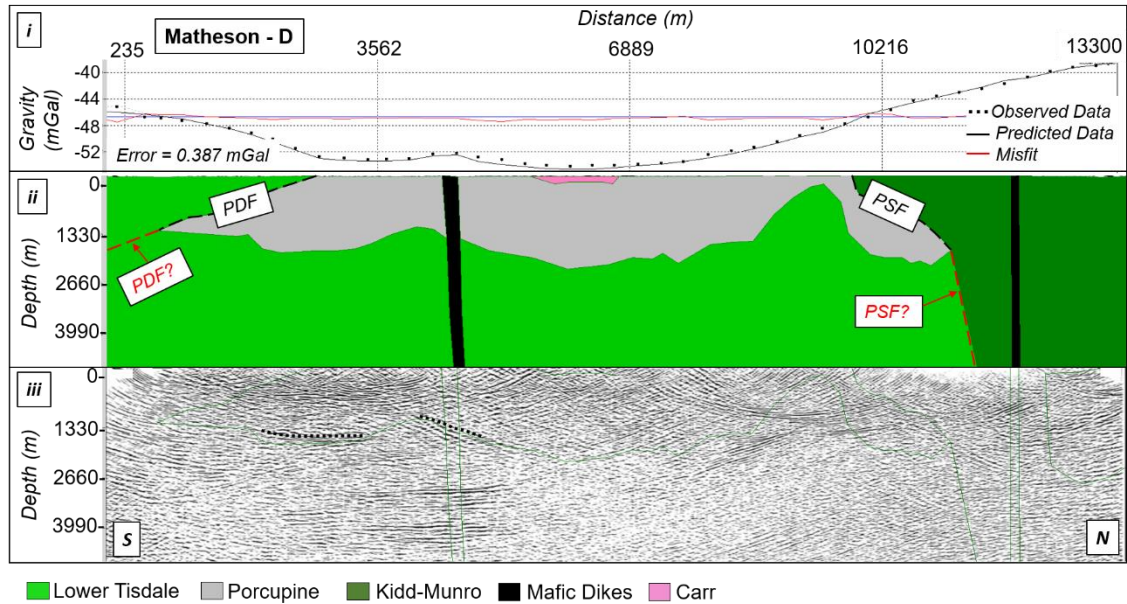


Figure 4.19. The Matheson line modeling showing the measured and predicted gravity data and the difference (red line) (*i*), the model itself (with the lithologies indicated by the colors shown in the legend at the base of the figure) and the modeled fault localizations shown with the dashed lines (*ii*), and the interpreted seismic section (*iii*).

The dip of the Porcupine-Destor fault obtained from the gravity modeling for profile D varies from 34 to 40 degrees to the south, with 5 vertex points added to resolve the fault geometry. The average dip over the modeled length of the fault is 36 degrees. The root-mean-square misfit is the lowest in comparison to the other three models, being 0.39 mGal. The misfit at each point is shown with the red line on Figure 4.19-*i*.

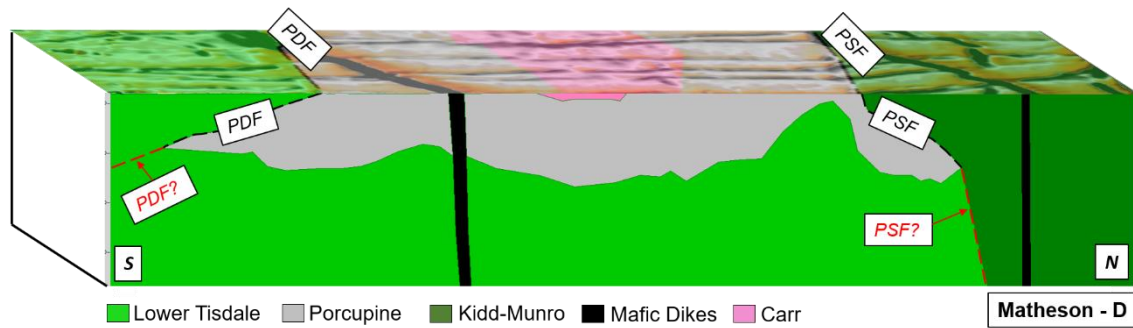


Figure 4.20. The 3D visualization of the Matheson line model (profile D) also shown in 2D in Figure 4.19-ii. The first vertical derivative of TMI, which is overlaying the surface geology, is displayed on the top to highlight the dikes at the surface.

4.4.5. 3D Visualization of the Models

By combining the final models for the Shillington line (section A), the Val Gagné line (section B), the Watabeag line (section C), and Matheson line (Section D) models, an orientated 3D view of the sections was generated (Figure 4.21). In this view, a holistic visualization of the interpreted and modeled Porcupine assemblage geometry is exhibited. This 3D perspective of the faults and dikes provides a better understanding of their spatial variation from profile to profile.

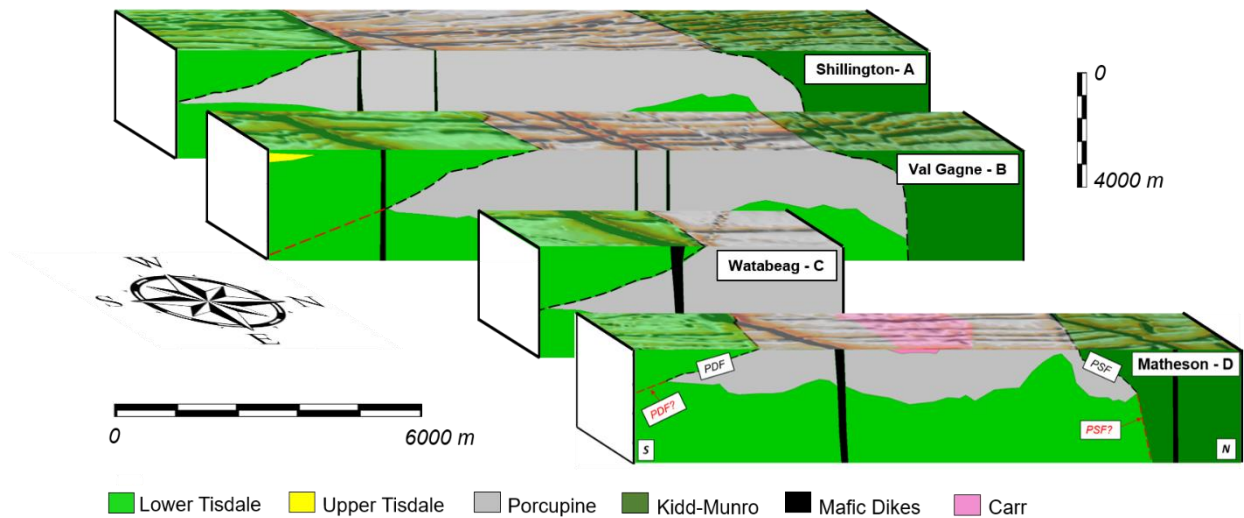


Figure 4.21. The 3D view of the parallel 2D models referred to the Shillington line (section A), the Val Gagné line (Section B), the Watabeag line (Section C), and the Matheson line (Section D).

4.5. Conclusions from the PASA profile models

The gravity modeling has provided a check on the validity of the seismic interpretation whenever the seismic interfaces are recognizable as reflection events. Specifically, the sub-horizontal contact between the base of the Porcupine assemblage and the underlying Lower Tisdale assemblages were evident in at least some part of all of the seismic sections. The potential-field modeling confirmed the dip ($30 - 49^\circ$ southward) and geometry of the Porcupine-Destor fault, which is economically important, as several gold deposits have been associated with this fault zone. The dip angles described in this chapter are qualitatively in agreement with the values reported in Chapter 3. In the Watabeag model, the PDF fault is dipping at the steepest angles (both in Chapter 3 and in this chapter), while in for the Val Gagné model, the PDF fault is dipping

south in the shallowest angle (Chapter 3 and this chapter). The results for the three profiles modeled in Chapter 3 with a linear fault and in this chapter with a piecewise-linear fault are shown in Table 4.2. The two dip estimates on each traverse differ somewhat quantitatively, in some cases beyond the error bounds estimated using the gravity data uncertainties, but qualitatively the PDF dip angle on the Watabeag traverse is in both cases higher than on the Matheson traverse and this in turn is higher than on the Val Gagné traverse. This shows that model assumptions such as a single linear fault, or a piecewise-linear fault can give different results, so is an important geological constraint.

Table 4.2. Comparison of fault dips from Chapter 3 and this chapter.

Profile	Linear fault (Chapter 3)	Average dip of piecewise-linear fault (Chapter 4)
B - Val Gagné	$28 \pm 1^\circ$	30°
C - Watabeag	$54 \pm 1^\circ$	49°
D - Matheson	$45 \pm 2^\circ$	36°

For interfaces that are not noticeable on the seismic sections due to either sub-vertical orientation or weak acoustic impedance contrast, our modeling can also be used to infer the dip. Specifically, the contact between the Porcupine and Kidd-Munro assemblages was not visible in any of the seismic profiles that crossed the contact (sections A, B and D), but modeling has suggested this contact should be sub-vertical, which explain why it is not visible in the seismic sections.

On the Matheson line only, the response of the mafic dikes was recognizable on the gravity data. This is likely because 1) the width of the intersected dike is about 300

meters (Montsion, 2018), which is similar to the gravity-station spacing, and 2) the low density of the surrounding metasedimentary unit results in a stronger contrast and a stronger anomaly. On sections C and D, the dike intrudes rock that has a density value closer to the dike, so the contrast is too weak to result in an observable anomaly. On section A, the uncertainties in the gravity data are larger, so it will be more difficult to see a dike anomaly. On the other hand, multiple dikes are evident on the gridded magnetic data.

The 3D visualization in Figure 4.21 shows that the model varies from profile to profile. The assumption of a 2D model (which does not vary along strike) is therefore not strictly valid. This suggests 3D modeling might be appropriate.

Chapter 5: 3D Gravity Inversion of the Matheson Area

Inverse modeling is frequently used to obtain density models from gravity data. The most straightforward type is the unconstrained inversion, which is a computational process used to find a model that solely satisfies the geophysical data. The model derived from these inversions can then be interpreted. If the model does not seem realistic, then an easy computational method to adjust the model and perhaps make it more realistic is to adjust the model smoothing (Li and Oldenburg, 1996; 1998). This type of smoothing is called a model smoothness constraint. In these types of inversions, other geophysical/geological information is not taken into account in the modeling. However, potential-field data may be explained by more than one model, and therefore an unconstrained or smoothness-constrained model might not provide a realistic explanation of the geology. If the model is constrained by some aspect of the known geology, then the model will become more realistic, Williams (2009) constrained a gravity inversion using the mapped surface geology and an estimate of the densities of each of the surface lithologies. Deeper information can also be used to improve the model at depth. For example, Kekana et al. (2017) constrained gravity inversions by adding drill-hole density information. Another approach, taken by Mahmoodi et al. (2017) was to use an extensive geological model derived from lithological information in 950 drillholes and assign the units with physical property information that were derived from 6 drill holes. This model was used as a reference model and any changes from this model were required to fit the gravity data. Other work that describes constrained gravity inversions include Sun and Li (2015), Astic and Oldenburg (2018), Geng et al. (2019), Darijani et al. (2020), Maag-Capriotti and Li (2021), Zhong et al. (2022)

In this work, we will be undertaking 3D inversions using constraints from geological mapping, physical property measurements and previous 2D models. These 3D inversions provide a reasonable model at shallow depth. We also investigate the impact of incorporating constraints from the deeper seismic information on some of the lines and show how this can be used to map the depth variation over the whole area, away from the seismic lines.

In the previous chapter, the study was focused on the Porcupine Assemblage Study Area (PASA), shown with the dashed rectangle on Figure 5.1. In this chapter, the modeling will be expanded to cover a larger area, the Matheson Study Area (MSA), which includes the low-resolution R1 Matheson seismic line. The MSA covers the full extent of the map shown in Figure 5.1 including the PASA and a comparable area to the south.

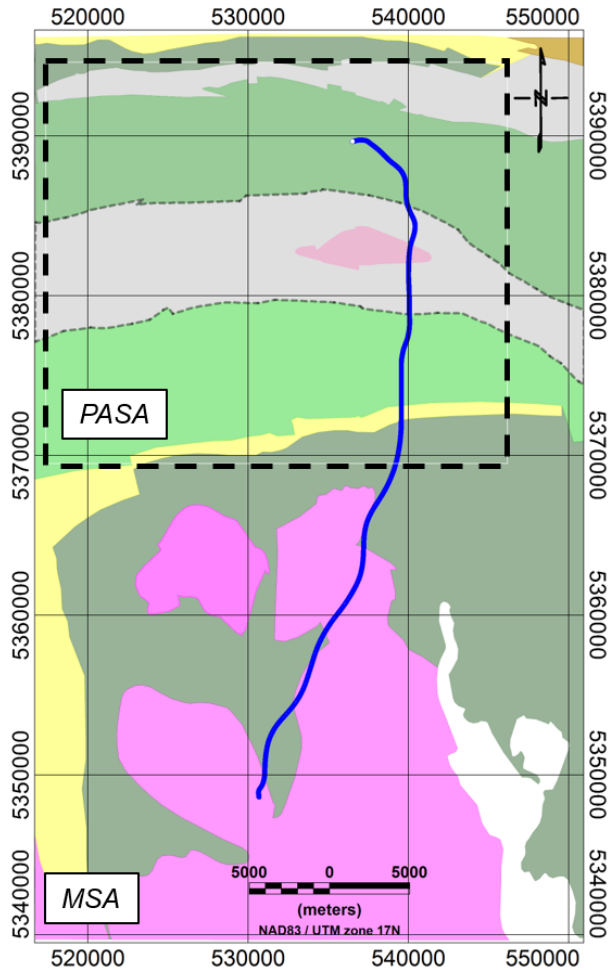


Figure 5.1. Simplified surface geology map showing the full extent of the Matheson Study Area or MSA (modified after Ayer, 2005). The area delimited by the dashed rectangle refers to the PASA described in Chapter 4. The blue line represents the location of the low-resolution Matheson seismic line (R1).

5.1. Geology of the MSA

Most of the geological units present in the study area were described either in Chapter 3 or in Chapter 4, but four geological units on Figure 5.2 have not been described yet: The Stoughton-Roquemaure (SR), and the Blake River assemblages, as well as the Watabeag Lake batholith and the Huronian supergroup.

The SR assemblage consists of metavolcanic rocks, which are composed predominantly of massive and pillowed mafic flows and occur along the north contact of the Kidd-Munro assemblage. The SR assemblage ranges in age from 2723 to 2720 Ma (Ayer et al., 2005). Examined outcrops show dark-green to brown weathering and are classified as fine-grained mafic flows (Berger et al., 2011). The study area, however, only covers a small part of this assemblage in the far northeast (Figure 5.2).

The Blake River assemblage, which predominates in the MSA, ranges in age from 2704 to 2696 Ma, and consists predominantly of flows of calc-alkaline basalt and andesite, locally with bimodal tholeiitic basalt and rhyolite (Ayer et al., 2005).

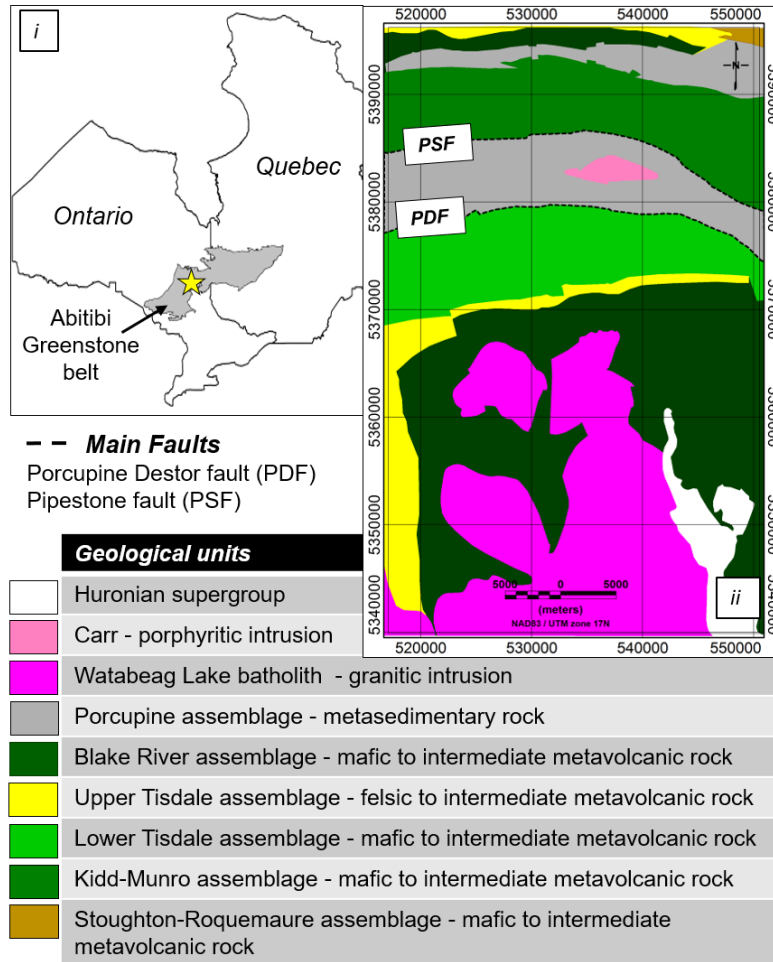


Figure 5.2. The study area location map on the top-left (*i*), the geological map (modified after Ayer et al., 2005) of the Matheson area on the right (*ii*). The legend for the geological map is shown in stratigraphic order, with the youngest at the top.

The Watabeag Lake batholith is intruded into the volcano-sedimentary assemblages in the MSA. The Watabeag intrusive rocks comprise massive to foliated granodiorite to granite, which ranges in age from 2695 to 2670 Ma (Ayer et al., 2005).

The Huronian supergroup is subdivided in four groups: The Elliot Lake, the Hough Lake, the Quirke Lake, and the Cobalt Groups (Baumann et al., 2011). This supergroup

consists predominantly of siltstone, argillite, sandstone, and conglomerate, which range in age from 2455 to 2222 Ma (Ayer et al., 2005).

5.2. Density Properties

Like the general geological description, the density values associated with the geological units in the PASA have been described in the previous chapter. Figure 5.3 shows the spatial location of samples that are used to estimate the density of the three additional units. These samples occur in the south part of the MSA and are described in Section 5.1. The SR assemblage sample locations are not shown in this map, as they are located outside of the MSA. The density database used in this study is described by Eshaghi et al. (2018).

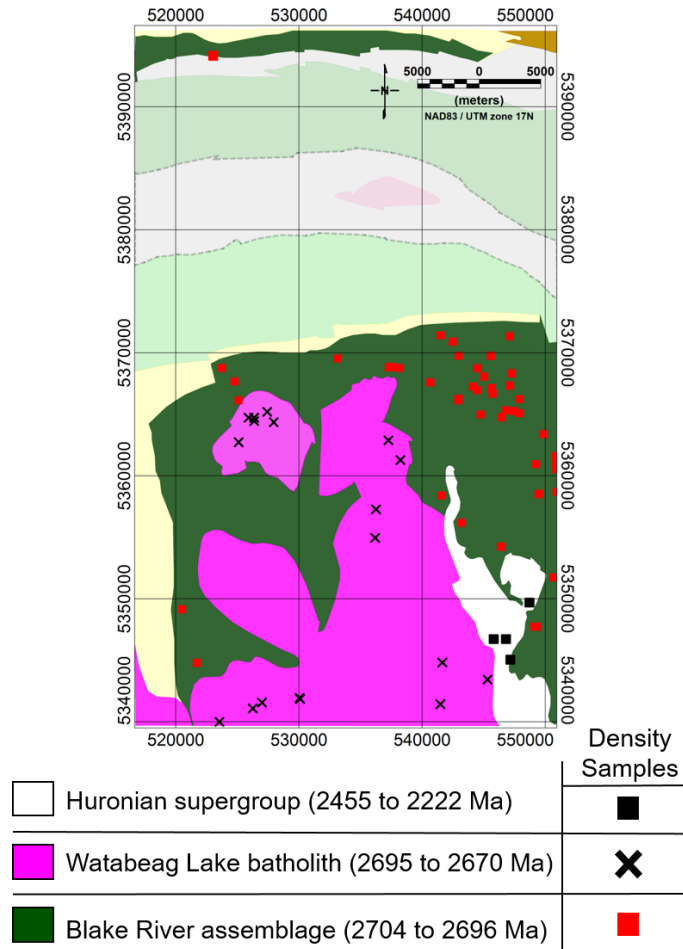


Figure 5.3. Location of samples that have associated density measurements for the geologic units that are in the MSA, but not the PASA (which have already been described in Chapter 4). Different location symbols are used for each geological unit, as shown in the legend. Some symbols might be indicating the location of more than one sample.

The SR assemblage, located in a small area in the extreme northeast part of the MSA, has a mean density of $2.99 \pm 0.06 \text{ g/cm}^3$. This estimate is based on just 14 samples acquired outside of the MSA, so the statistical estimates are less than ideal. The histogram for these 14 samples is shown on Figure 5.4. Because the SR assemblage takes up such a small volume in the study area, a poor estimate will not adversely influence the results.

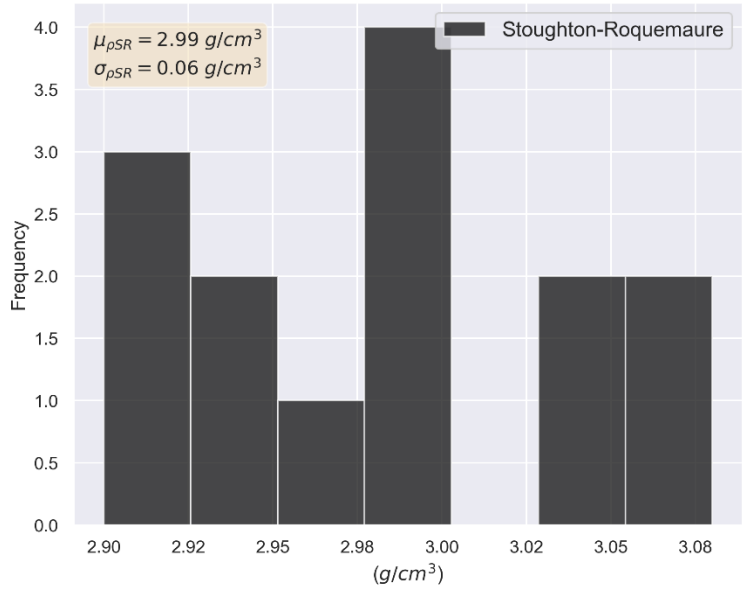


Figure 5.4. Histogram of the measured density values of the Stoughton-Roquemaure assemblage with the mean ($\mu_{\rho_{SR}}$) and the standard deviation ($\sigma_{\rho_{SR}}$) on the top left of the figure.

It is possible to obtain better estimates of the density for the Blake River assemblage, as there are 86 samples in the MSA. The mean density was estimated to be $2.94 \pm 0.11 \text{ g/cm}^3$ (see Figure 5.5).

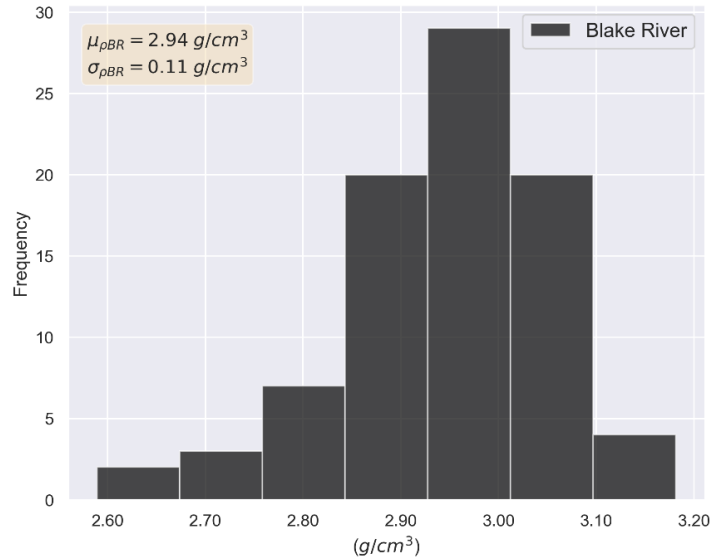


Figure 5.5. Histogram of the measured density values of the Blake River assemblage with the mean ($\mu_{\rho_{BR}}$) and the standard deviation ($\sigma_{\rho_{BR}}$) on the top left of the figure.

The mean density for the Watabeag Lake intrusion was estimated to be $2.63 \pm 0.02 g/cm^3$, using 28 samples (see Figure 5.6).

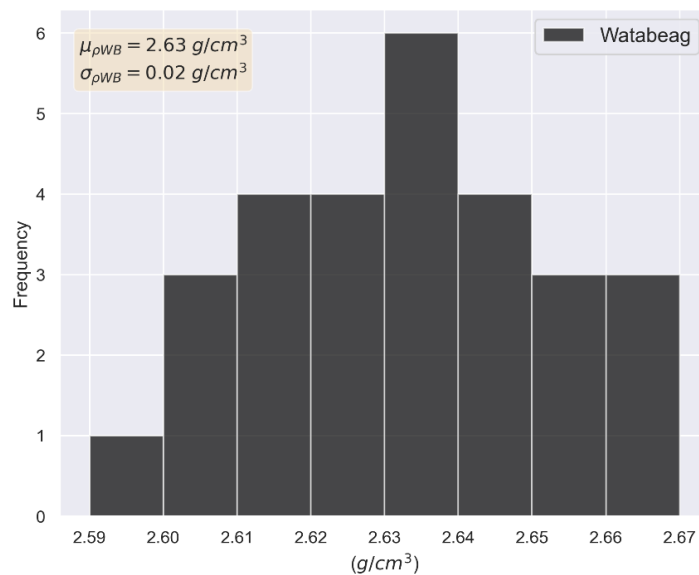


Figure 5.6. Histogram of the measured density values of the Watabeag Lake intrusion with the mean ($\mu_{\rho_{WB}}$) and the standard deviation ($\sigma_{\rho_{WB}}$) on the top left of the figure.

Lastly, for the Huronian supergroup the mean density was estimated as $2.71 \pm 0.03 \text{ g/cm}^3$. This value was estimated based on 15 samples that crop out inside and outside of the MSA

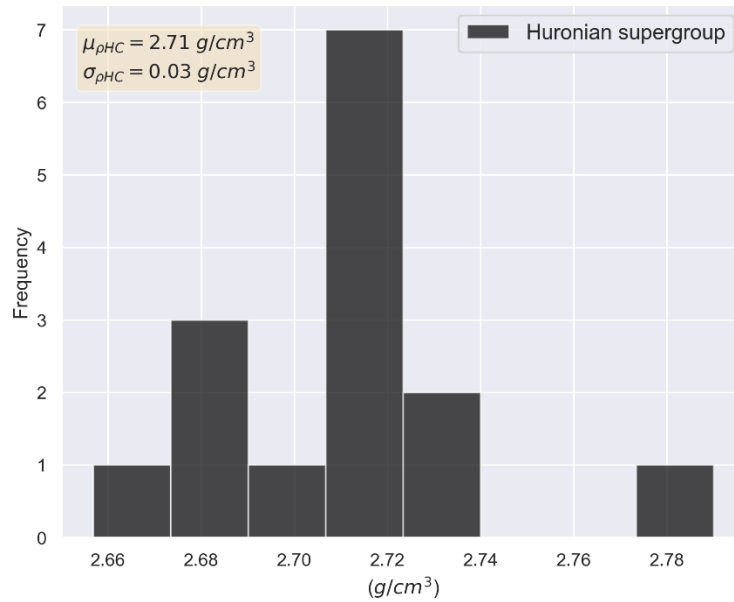


Figure 5.7. Histogram of the measured density values of the Huronian supergroup with the mean ($\mu_{\rho_{HC}}$) and the standard deviation ($\sigma_{\rho_{HC}}$) on the top left of the figure.

Compiling all the estimated mean density values described in this chapter and in the previous chapters, the mean density values for the MSA vary from 2.63 g/cm^3 (Watabeag Lake batholith) to 2.99 g/cm^3 (Stoughton-Roquemaure). All the values are tabulated in Table 5.1 and shown graphically in Figure 5.8.

Table 5.1 - Data summarizing the density measurements: mean, standard deviation from the mean, as well as the number of samples. Including those already reported in Chapter 4.

Unit (listed from youngest to oldest)	Mean density (g/cm ³)	Standard deviation (g/cm ³)	N° of samples
Huronian supergroup	2.71	0.03	15
Carr intrusion	2.69	0.02	11
Watabeag Lake batholith	2.63	0.02	28
Porcupine assemblage	2.73	0.04	46
Blake River assemblage	2.94	0.11	86
Upper Tisdale assemblage	2.76	0.05	35
Lower Tisdale assemblage	2.89	0.10	90
Kidd-Munro assemblage	2.90	0.13	343
Stoughton-Roquemaure assemblage	2.99	0.06	14

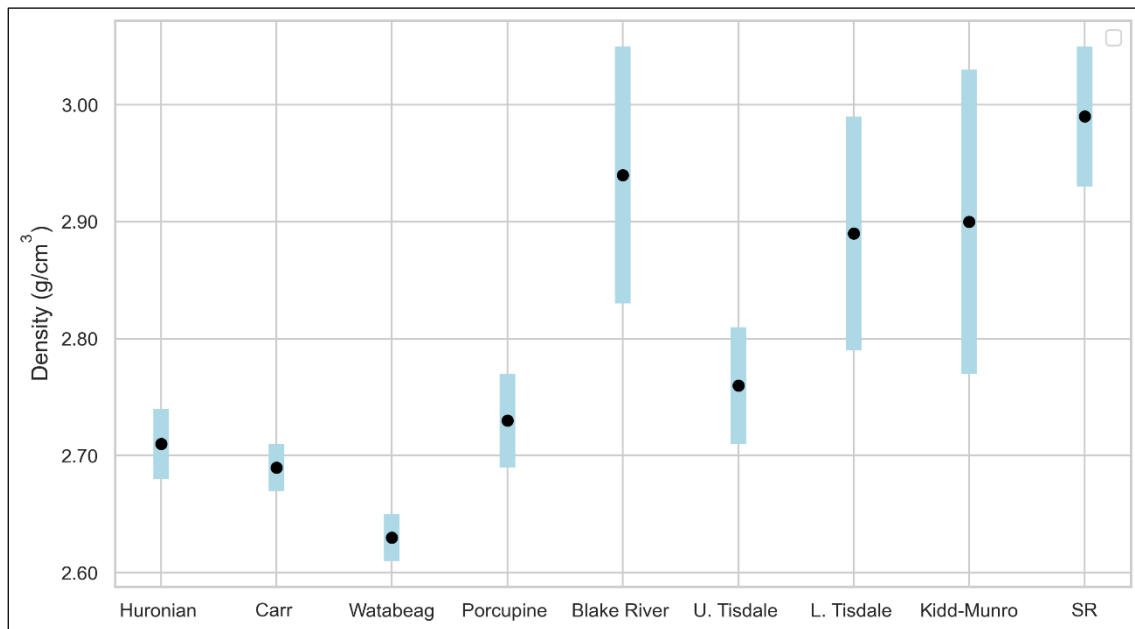


Figure 5.8. Graph showing the density measurements: mean (black circles), and standard deviation from the mean (blue bars) for each geological unit.

5.3. Gravity Data

The MSA is well covered by gravity stations as shown on the left of Figure 5.9. Combining the CGDB stations (in black) with the ME stations (in blue), provides 1144 gravity stations. Even though there is a good coverage at the study area, the stations are not uniformly distributed. On the right of Figure 5.9 is a colored map of the minimum spacing to the nearby gravity stations across the whole study area. The color scale varies from red, where the gravity stations are close to each other, to blue, where they are sparser. Generally, the gravity stations are closer proximal to the main faults area, except those along the ME R1 seismic line, which traverses most of the geological units from the bottom (south) to the top (north) of the MSA.

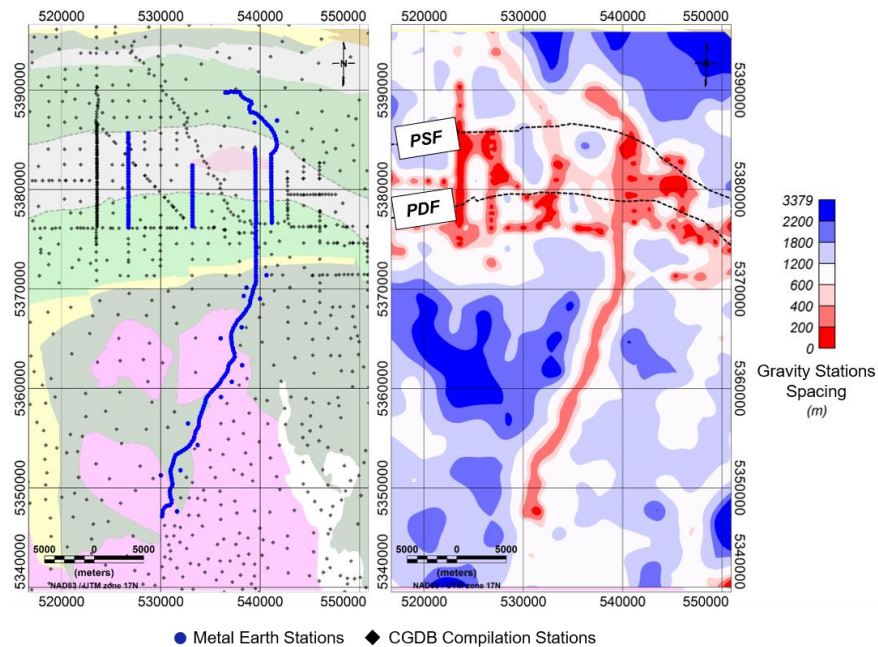


Figure 5.9. The gravity stations location (on the left), where blue circles refer to the ME data, and the black diamonds represent the CGDB data. On the right the estimated minimum spacing of the gravity stations.

Whereas the spacing mean is 665 meters for the entire study area, the spacing median is 393 meters. This difference between the mean and median is expected due to the fact that the data along road traverses (such as the ME survey) were at about 300 m spacing, while the off-road spacing varied from 1 - 2 km.

The ME and CGDB datasets were compiled into one single dataset and all the corrections applied, obtaining the reduced gravity data. Figure 5.10 (right), shows the complete Bouguer anomaly map generated from this compiled data. Some of the gravity anomalies appear to correlate well with units on the surface geology map (Figure 5.10 on the left) such as the lows associated with the Porcupine assemblage and the Watabeag Lake batholith.

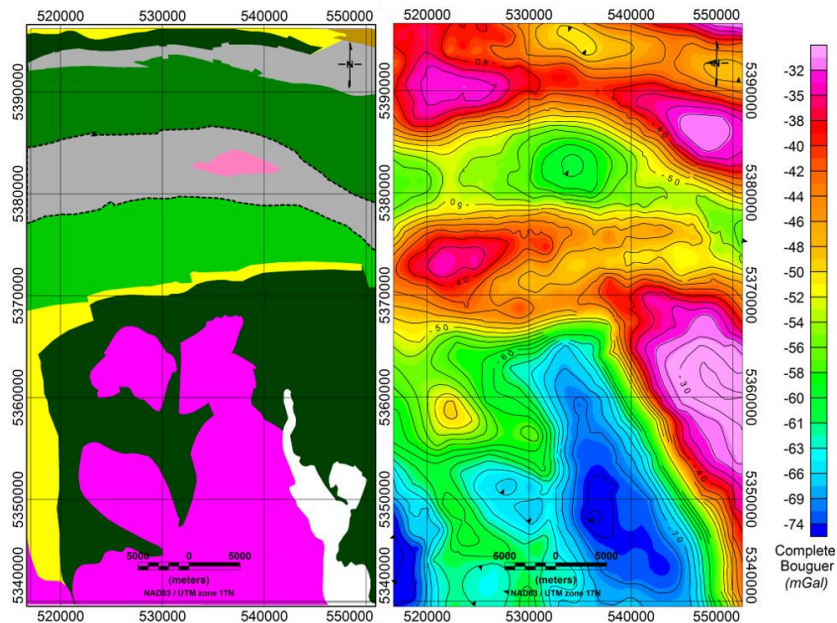


Figure 5.10. Complete Bouguer anomaly gravity grid on the right and the surface geology for the MSA (left). The gravity data was obtained from the Metal Earth project and the Canadian gravity data compilation. For the geological legend, see Figure 5.2. The grid cell spacing is 100 m, whereas the gravity station spacing can vary up to 2 km or more in some locations.

5.4. 3D Unconstrained to Constrained Inversions of the MSA Gravity Data.

The low-resolution seismic line (R1) traverses the majority of the surface geological units (Figure 5.1). Nonetheless, few coherent reflectors can be visualized in the R1 seismic section (Figure 5.11-*i* or 5.11-*ii*), with only three coherent reflectors: *a*, *b*, and *c* being evident. The reflections identified as *a* are located at about 15 km depth, assuming a velocity of 6 km/s in the interval from 0 to 15 km. Figure 5.11-*ii* shows the section plotted as a function of the two-way travel-time, which is the time for the reflected seismic wave to travel from the source at the surface, down to the interface, then back up to a given receiver at the surface. Assuming the same interval velocity, the reflectors *b* and *c* are roughly located at approximately 8 and 9 km depth, respectively.

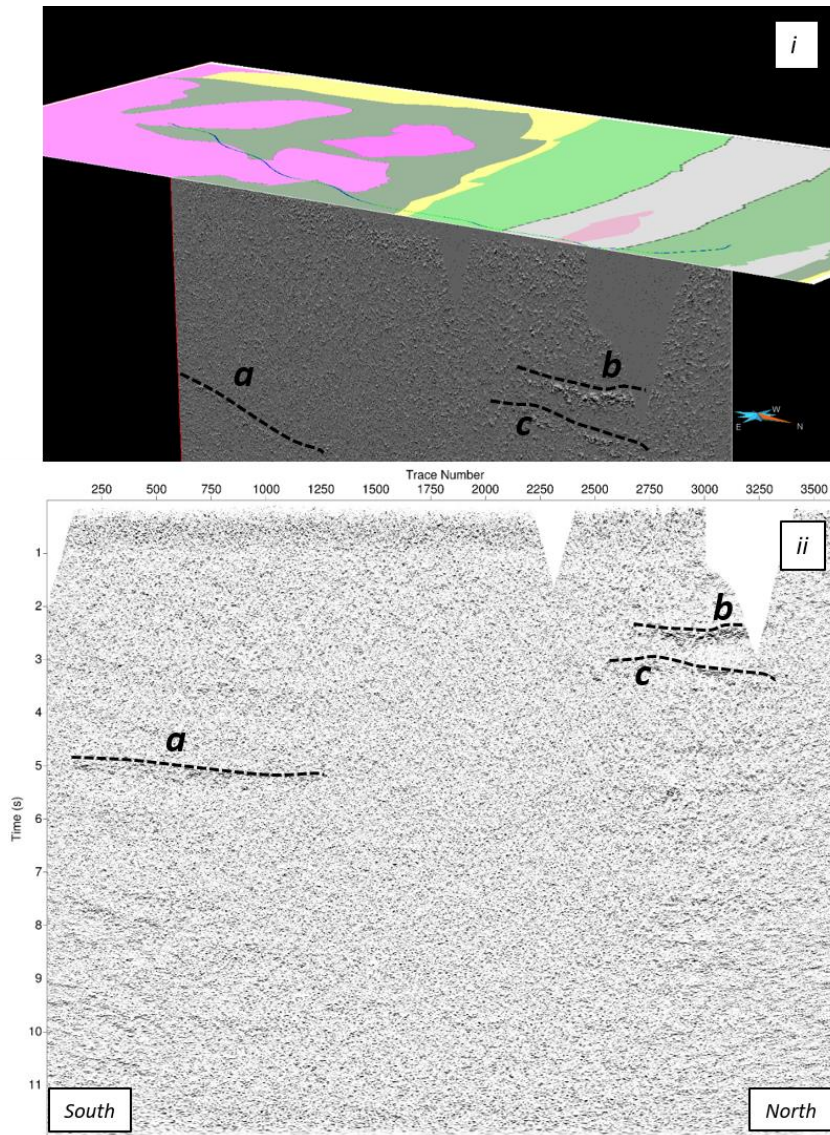


Figure 5.11. R1 Matheson seismic line section shown in perspective and overlaid by the MSA surface geology (*i*) and below as a function of two-way travel time (*ii*). On both views the main reflectors, *a*, *b* and *c* are marked.

Whereas the R1 seismic section cannot be used to identify features at shallow depth, the gravity data, in combination with the density compilation and geological constraints from previous studies may be used to help define a shallow geologic model.

The following sections will demonstrate how incorporating constraints, either geophysical or geological, can enhance the inverted final model and help reduce the non-uniqueness problem inherent in gravity data.

5.4.1. Inverse Modeling

In the inverse modeling procedure for interpreting geophysical data, the process is automated and done by a computer algorithm (Dentith and Mudge, 2014). For the forward procedure, the model parameters are estimated and the model response is calculated to see if it explains or fits the data. If the fit is poor, the modeller manually selects another set of model parameters and proceeds through multiple iterations until the fit is as good as possible. On the other hand, for the inverse problem, the algorithm is told the observed data and the computer systematically adjusts the model parameters until the model data fits the observed data (Menke, 2012). The process seems very different, but in some ways it is similar, as the algorithm also has to be told an initial model to start from and different initial models or constraints will usually give different final results. Hence, multiple runs are still required.

The inverse problem can be classified into two types: linear and nonlinear. The linear inverse problem can be represented with the explicit linear equation (Menke, 2012),

$$\mathbf{Gm} = \mathbf{d}, \quad (5.1)$$

where, \mathbf{G} is a matrix called the data kernel and it represents the relationship between data (\mathbf{d}) and model parameters (\mathbf{m}).

Inverse theory, broadly, is an organized set of mathematical techniques for resolving inverse problems (Menke, 2012).

In the simplest (linear) case, \mathbf{G} is independent of \mathbf{m} and the model parameters can be obtained by matrix inversion, $\mathbf{m} = \mathbf{G}^{-1}\mathbf{d}$. However, the inverse of \mathbf{G} may not be simple to calculate, or it may be non-linear and depend on \mathbf{m} , which is not yet known, so a variety of methods have been developed for solving the inverse problem, such as least squares, minimum length, maximum likelihood, Newton, simulated annealing, steepest descent, etc. (Menke, 2012).

The steepest descent method is a non-linear method and the matrix inversion is not required (Fullagar and Pears, 2007). From a starting guess, the model moves “downhill” on the topography of the misfit function (E) in order to find a solution with smaller misfit, some information about the derivatives of the misfit function (with respect to the model parameters) is required (Pratt, 2018),

$$\nabla E_m = \mathbf{G}^T \Delta \mathbf{d}, \quad (5.2)$$

where ∇E_m is the gradient of the misfit function.

Knowing the direction of the steepest gradient, the following algorithm can be used to improve the model misfit (Pratt, 2018),

$$\begin{aligned} \mathbf{m}^{i+1} &= \mathbf{m}^i - \gamma^i (\nabla E_m)^i, \\ &= \mathbf{m}^i - \gamma^i (\mathbf{G}^T \Delta \mathbf{d})^i, \end{aligned} \quad (5.3)$$

where γ^i is the step-length that minimizes the misfit in the direction $-\nabla_m^i E$ at the i th iteration. However, it is not immediately known how large the step-length should be. If the

step is too large, the minimum misfit may be skipped over; if it is too small, the convergence towards the minimum will be very slow. *Armijo's rule* might be used to provide an acceptance value for γ (Menke, 2012),

$$E(\mathbf{m}^{i+1}) \leq E(\mathbf{m}^i) + c\gamma \mathbf{v}^T (\nabla E_m)^i, \quad (5.4)$$

where

$$\mathbf{v} = -\frac{\nabla E}{|\nabla E|} \quad (5.5)$$

and c is an empirical constant in the range (0,1) that is usually chosen to be about 10^{-4} . In the VPmg algorithm, which is used for inversion modeling in this study, the steepest descent method is utilized, and for estimating the misfit a chi-squared, χ^2 , value is used. The fit is considered to be acceptable when $\chi^2 \sim 1$ (Fullagar and Pears, 2007). The chi-squared quantity is defined by

$$\chi^2 = \frac{1}{N} \sum_{n=1}^N \left(\frac{o_n - c_n}{\varepsilon_n} \right)^2, \quad (5.6)$$

where,

N = number of data,

o_n = observed data,

c_n = the calculated data,

ε_n = corresponding data uncertainties (estimated using the procedures defined in Chapter 2).

5.4.2. Unconstrained Gravity Inversion

Gravity inversions, either unconstrained or constrained, are used to create 2D or 3D models of the density consistent with the gravity data. In a VPmg unconstrained inversion, the final density distribution is obtained assuming that the earth is comprised of a number of cells, each with their own individual density. The initial guess is usually a uniform density for all cells and this model is improved iteratively by minimizing a model objective function subject to fitting the observed data (Li and Oldenburg, 1998). In other words, with unconstrained inversions, the algorithm aims to find an appropriate model that minimizes the mismatch between the observed and the calculated data. The inherent non-uniqueness is overcome by making one or more assumptions based on mathematical factors, such as depth weighting (to make the deeper cells more important), direction weighting, and the degree of smoothness of lateral variations in the physical properties in the resulting mesh model (Vallée et al., 2019).

Firstly, a purely unconstrained inversion was generated for the MSA. Since the algorithm computes the topographic variation, free-air data was used as the input. The initial 3D density model was built in a volume 56×34 km horizontally and 25 km vertically. The horizontal and vertical size of the cells were both 300 m and the starting model density was 2.67 g/cm^3 . Topographic information (Shuttle Radar Topographic Mission [SRTM] with a 30 m spacing) used for this inversion was downloaded from the Geosoft public DAP server (<http://dap.geosoft.com>). The free-air gravity data, gridded from the ME and CGDB compilation, had a 300 m cell-size and this was used as the data input (see Figure 5.12).

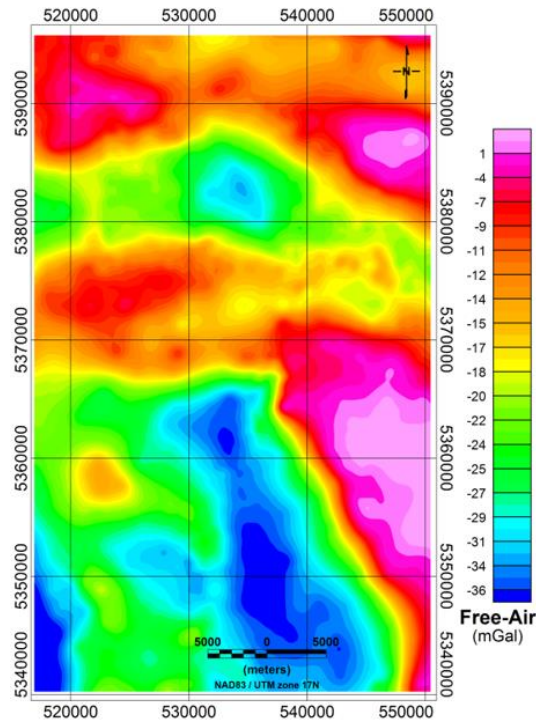


Figure 5.12. Free-air anomaly gravity grid in the MSA. The data was obtained from the Metal Earth project and the Canadian gravity data compilation (CGDB).

VPmg version 9.0 (Fullagar and Pears, 2007), which is linked to the Mira Geoscience GOCAD mining suite, was used to perform the inversions. The fit is deemed satisfactory when the misfit is comparable to the data uncertainties. A reasonable misfit was obtained in 34 iterations, returning a root mean square (RMS) misfit of 0.97 mGal as shown on Figure 5.13. A misfit of about 1 mGal is considered appropriate as the uncertainty for the CGDB dataset is not known, but 1 mGal seems reasonable and also looks to be as the lower limit of what can be achieved. The misfit as a function of position is seen in Figure 5.14, where the maps of the observed, predicted and residual data are also shown.

The purely unconstrained inversion final model is showed in Figure 5.15 (*i* and *iii*). As the surface geology is displayed on the top of the density model, some geological units can be associated with the specific model densities. At the south of the MSA, there is a large volume of low-density material that may be associated with the Watabeag Lake Batholith. To each side of this low, the horizontal section at 10 km depth shows a high-density area, which may explain the positive anomaly associated with the outcrop of the denser Blake-River assemblage. The larger density anomaly here implies the Blake-River might be thicker as is suggested by the inversion modeling.

The results for the Porcupine assemblage can be compared with the results from Chapter 4. The vertical N-S section of the model in Figure 5.15 (*i* and *iii*) was intentionally selected at the Shillington seismic section. Below the Porcupine outcrop is a zone of low density, as indicated with the dashed box in 5.15-*iii*. Previous interpretation of the Shillington seismic sections, has suggested that the Porcupine assemblage in this area is approximately 2 km thick (Snyder et al., 2008), which is close to the value obtained in the 2D modeling described in the previous chapter. However, the density model from the unconstrained inversion is showing a much deeper low-density region, which is inconsistent with the previous studies (see 5.16 – *i*).

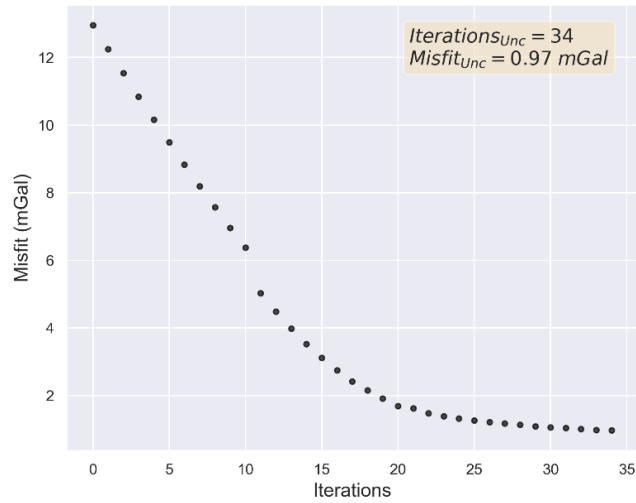


Figure 5.13. RMS misfit as a function of the iteration number for the unconstrained inversion (Unc). The maximum number of iterations and the achieved misfit are shown on the top right of the figure.

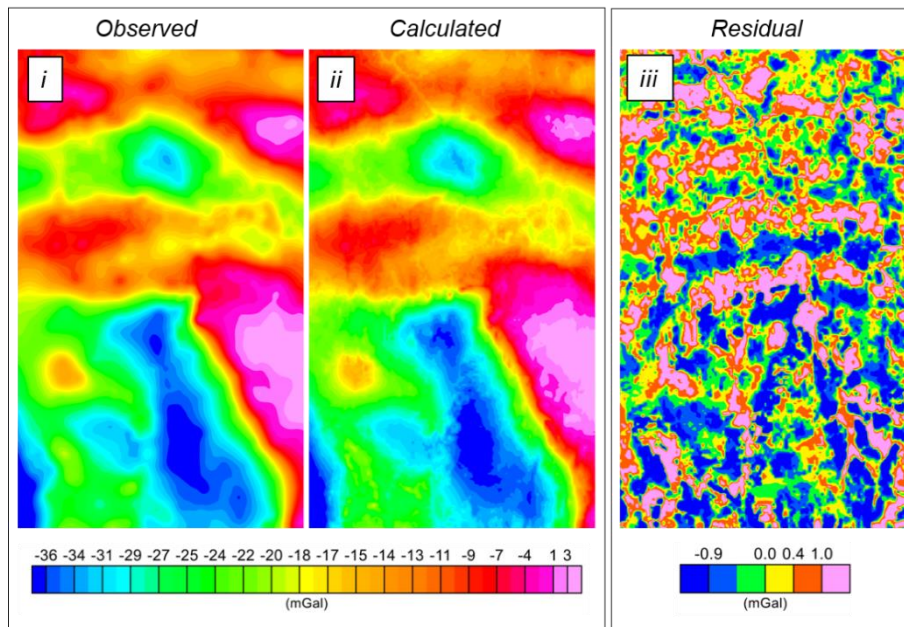


Figure 5.14. Observed free-air anomaly data grid (*i*), calculated data grid (*ii*), and the residual data grid (*iii*) computed from the unconstrained inverse model shown in Figure 5.15.

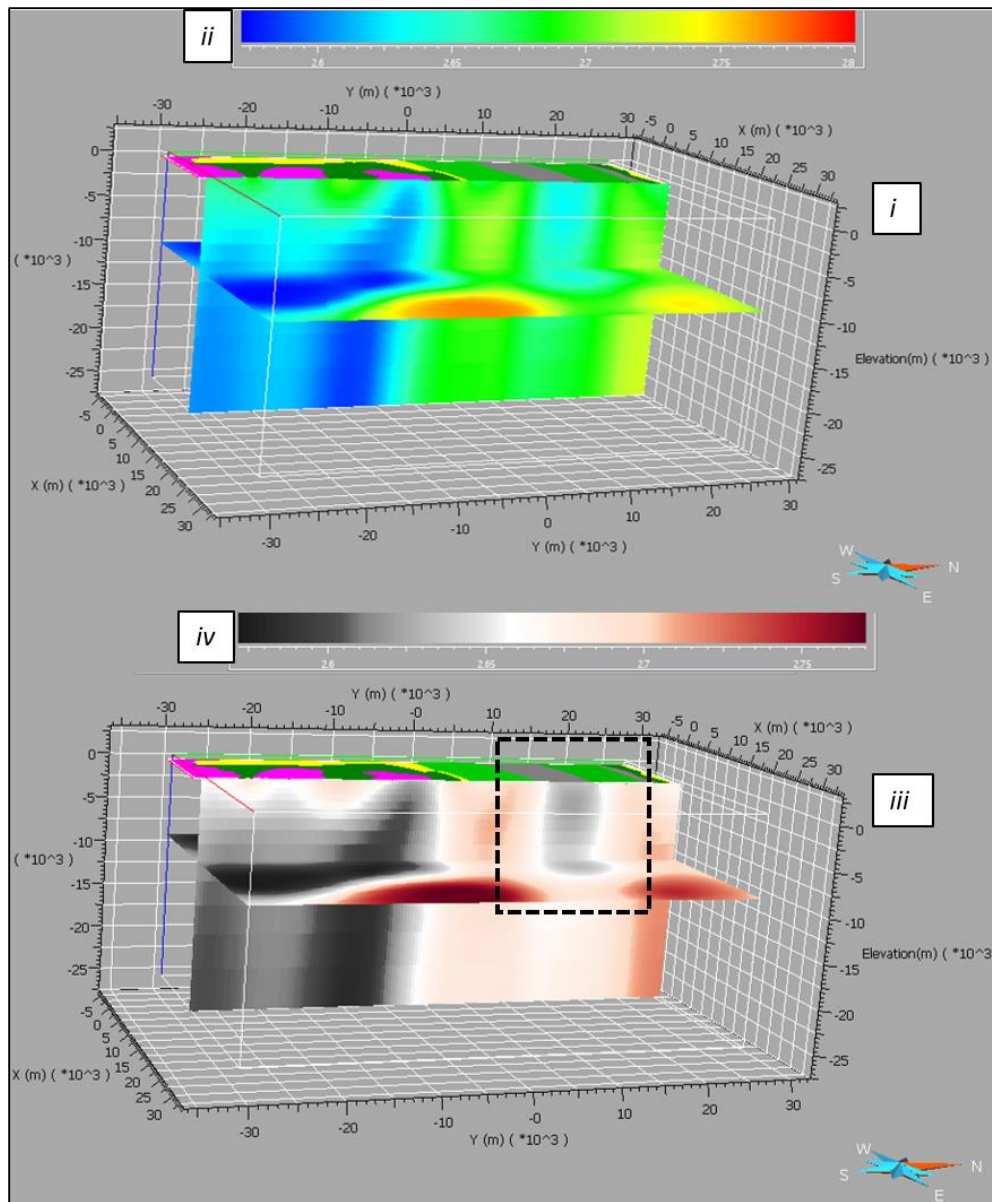


Figure 5.15. S-N vertical and horizontal sections of the unconstrained inverse density model overlaid by the surface geology map (*i* and *iii*). They represent the same density model differing solely by the color palette (*ii* and *iv*). In *iii* the feature associated with the Porcupine assemblage is highlighted by the dashed square.

Figure 5.16-*i* zooms into this inconsistent area and here the gray colors in the model correspond with the dark gray on the geological map that is associated with the

Porcupine assemblage. This gray zone in the model is thicker (~10 km) than suggested by the previous studies. In addition, the density values derived from the inversion are light grey and light grey on the color bar corresponds to densities of 2.63 g/cm³, as shown in Figure 5.16-*iii*, which is lower than the density mean of 2.74 g/cm³ compiled for this assemblage (see Table 5.1).

Unlike on the 2D modeling described in the Chapter 4, in the 3D model showed in Figures 5.15 and 5.16, features extend to greater depth and show smooth transitions, which in many cases are geologically unrealistic. Such features are common in inversion where there is no geological, petrophysical, or geophysical constraints. The lack of any prior information, leads to a corresponding lack in control over depth/geometry of the source or over the density distribution (Dentith and Mudge, 2014). The histogram of the density of cells in the final unconstrained model is shown on Figure 5.17. This ranges from 2.55 to 2.77 g/cm³, which is very roughly the same range of densities spanned by the numbers in the density property compilation (2.6 to 2.9 g/cm³ (Table 5.1). As the starting model was 2.67 g/cm³, the inversion has decreased some values to by as much as 0.12 g/cm³ and increased other values by up to 0.10 g/cm³.

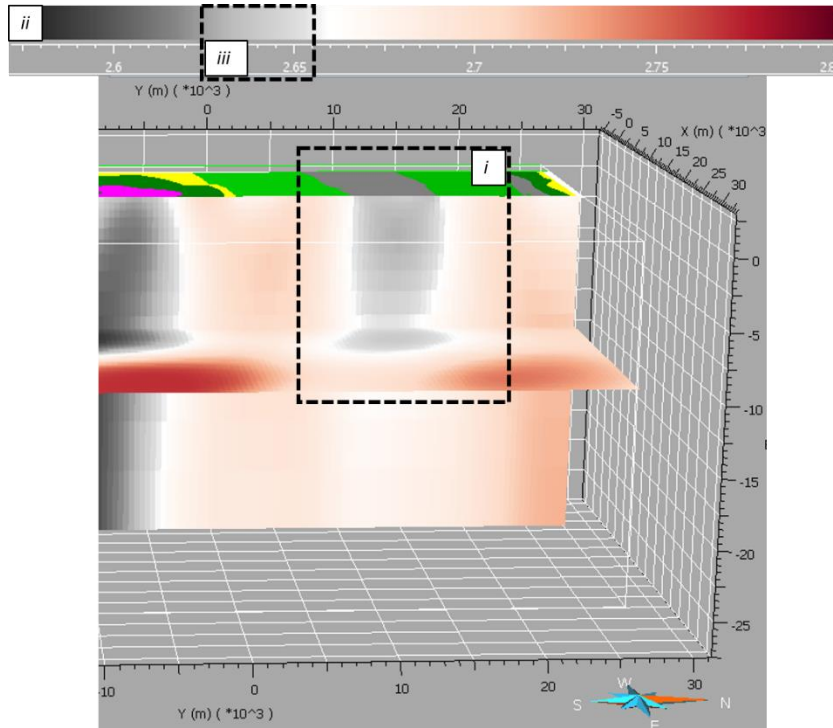


Figure 5.16. Zoomed in view of the unconstrained model. The dashed rectangle (*i*) highlights the feature that might be associated with Porcupine assemblage. The density color bar is shown in panel (*ii*) and the smaller dashed rectangle on the color bar (*iii*) shows that the light grey densities that have been associated with the Porcupine (2.65 to 2.67 g/cm³).

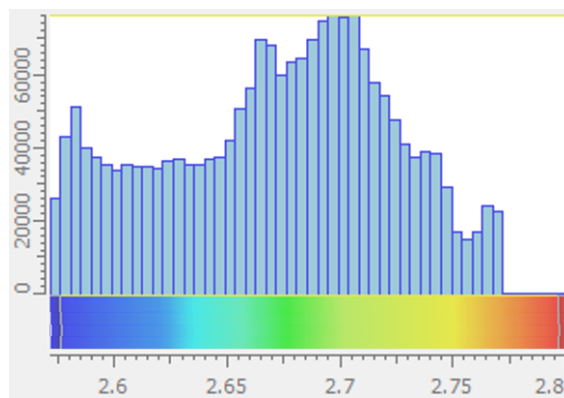


Figure 5.17. Histogram of the inverted density values from the unconstrained model. The X axis displays the density values, while in the Y axis shows the frequency of the density values.

5.4.3. Constrained Gravity Inversion I: Resolving the Source's Location for the Porcupine assemblage

In Section 5.4.2, the density model was obtained without considering any prior information/data. The consequence of this is that the thickness of the Porcupine is too deep in comparison to the estimates from other studies, such as the estimate of 2 - 2.5 km on the Shillington line, which is based primarily on the seismic data (Chapter 4).

A simple mathematical way to control the depth of features is to use a depth-weighting factor. This factor was introduced as in early inversion experiments by Li and Oldenburg (1996, 1998) they found that inversion models tended to place large variations in physical properties close to the surface regardless of the true depth of the causative bodies. They argue that this happens because the constructed model is a linear combination of kernels that decay rapidly with depth. The depth weighting that Li and Oldenburg (1996, 1998) introduce counteracted the natural decay of the kernels. The general expression for the weighting function (Li and Oldenburg, 1996) is given by

$$W(z) = \frac{1}{(z - z_0)^{\beta/2}}, \quad (5.7)$$

where

z = it is the observation height,

z_0 = is the depth of the cell to which the weight is being applied and depends upon the cell size and the model discretization, and

β = is the decay exponent.

Conceptually similar but somewhat variant expressions and techniques might be found in the literature (Fullagar and Pears, 2007; Vitale and Fedi, 2020).

The VPmg algorithm, which has been used to obtain the inversion model in this study, however is computed using the following variant equation (Fullagar, 2013)

$$W(z) = 1 - \left(\frac{z_0 + offset}{MD + offset} \right)^{\beta/2}, \quad (5.8)$$

where MD is the maximum depth of the computed model, z_0 is the depth of the cell to which the weight is being applied, and $offset$ is a parameter calculated from a nominated *maximum weight*. The VPmg cell weights are normalized values between 0 and 1 (0 is completely free and 1 absolutely fixed). This parameter allows the user to specify a maximum constraint (maximum weight) to be assigned.

The VPmg algorithm user, therefore, has to provide the maximum weight and the decay exponent (β). In the case these parameters are not provided, the algorithm uses default values, which was the case for the computed model described in Section 5.4.2. These defaults are a maximum weight = 0.9 and $\beta = 2.0$. Li and Oldenburg (1998) suggested that gravity inversion using a weighting function defined by β in the range of $1.5 < \beta < 2.0$ produces satisfactory results. Hence, the default decay exponent was maintained and just the *maximum weight* was adjusted so that the thickness of the Porcupine assemblage at the Shillington line was as close as possible to the previous interpretation in Chapter 4.

Using a *maximum weight* of 0.5 results in what is called a “slightly” constrained model, which is presented in Figures 5.18 (either *ii* or *iv*) and 5.20. Although the maximum weight was different, the number of iterations to achieve a desirable misfit (1 mGal) was about the same (35 iterations). It is important to highlight that the *maximum weight* value was obtained by trying different values until the desired thickness of the feature associated with the Porcupine assemblage, was obtained from the gravity inversion.

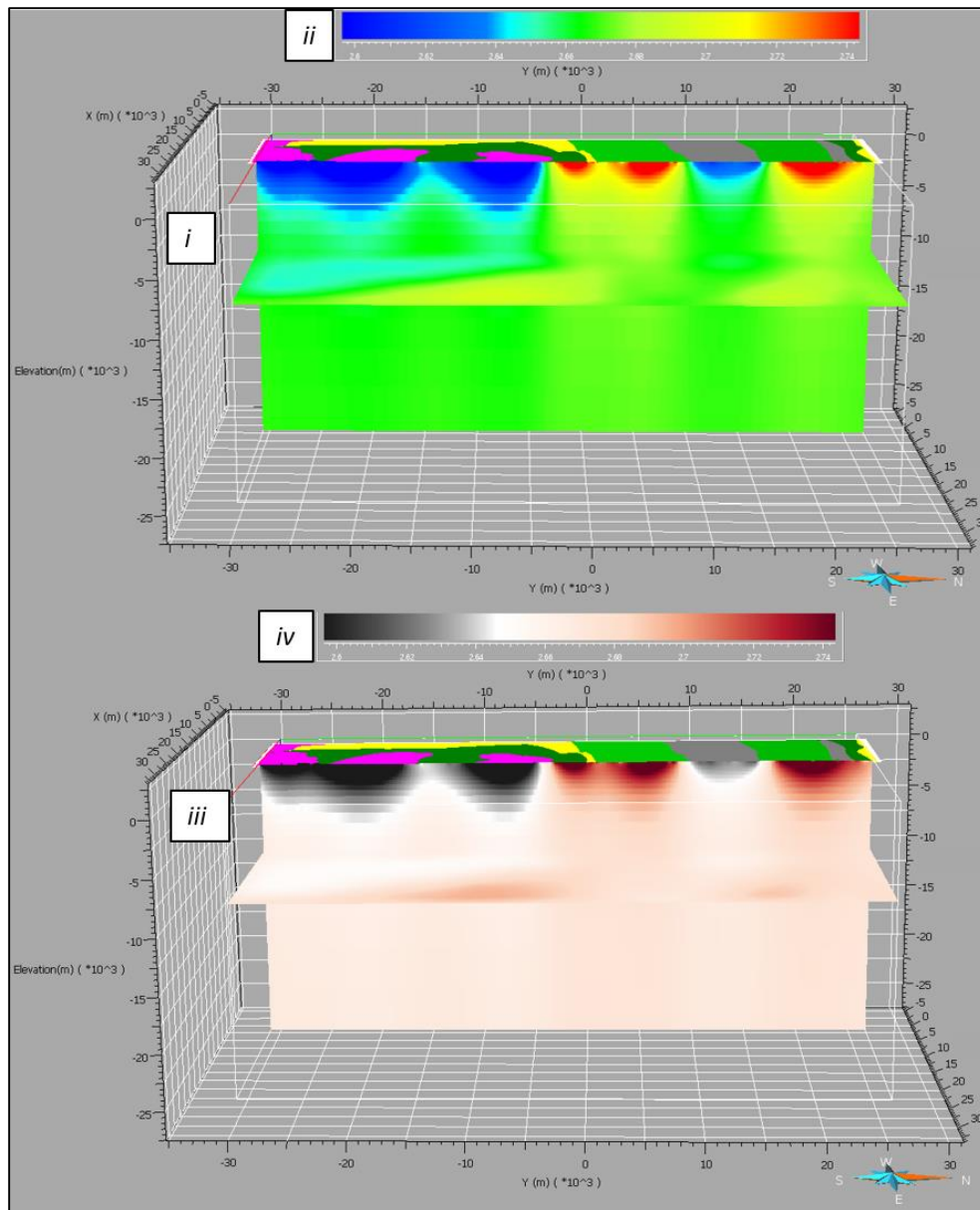


Figure 5.18. S-N vertical and horizontal sections of the depth-weighted or slightly constrained smoothed inverse model overlaid by the surface geology map (*i* and *iii*). The vertical section is at the location of the Shillington transect. The model is the same, but different color palette (*ii* and *iv*) are used for *i* and *iii* respectively.

As desired, the feature associated with the Porcupine assemblage became thinner, but so do the features associated with all the other units, such as those

associated with the Watabeag Lake batholith, the Blake River and the Kidd-Munro assemblages. As well, the model density values became more tightly concentrated around the starting model density value 2.67 g/cm^3 as shown in Figure 5.19. In addition, there is a second smaller peak around 2.63 g/cm^3 . The range of density values is even less consistent than seen on Figure 5.17 with the measured range of values in Table 5.1.

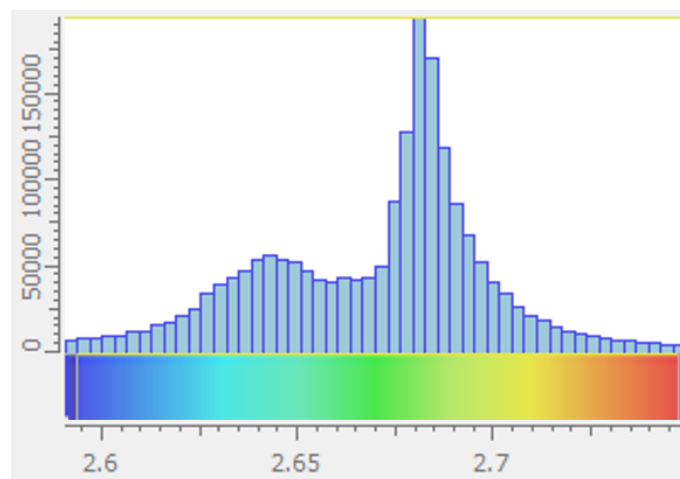


Figure 5.19. Histogram of the inverted density values from the depth-weighted or slightly constrained model. The X axis is the density values, while the Y axis is the frequency of the density values.

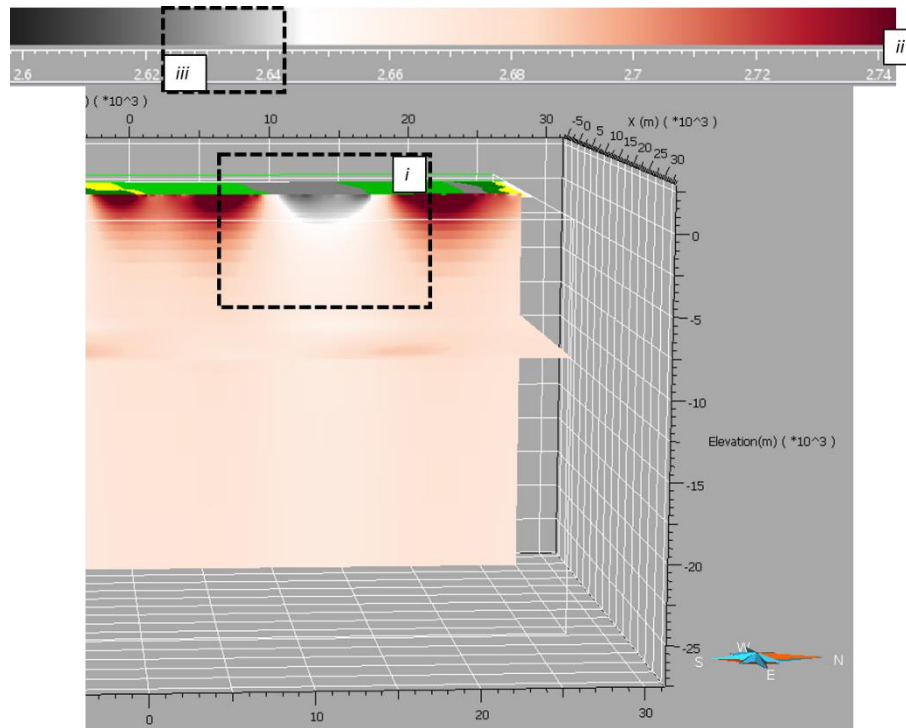


Figure 5.20. Zoomed unconstrained model highlighting the feature that might be associated with the Porcupine assemblage (*i*) with the corresponding density values (*iii*) shown in the color legend (*ii*). The vertical section is at the location of the Shillington transect.

When the most appropriate depth weighting for the Shillington line is applied to other parts of the MSA, it is possible to see an indication of variations in the thickness of the Porcupine. In Figure 5.21-*i*, the vertical section coincides to the Matheson traverses. Assuming that the porcupine is characterized by densities in the interval (2.62 – 2.64 g/cm³), then the thickness of the Porcupine assemblage in Figure 5.21 is thinner, and therefore is in agreement with the results obtained either in Chapter 4 or in Haugaard et al. (2021).

Even though using the density interval 2.62 – 2.64 g/cm³ has helped to infer the Porcupine assemblage thickness, it has not helped to resolve the inconsistency between

the petrophysical values from the inversion and the measured values. As mentioned in Chapter 4, the mean density for the Porcupine assemblage from the data compilation is 2.73 g/cm^3 , which is higher than the value obtained from the ‘slightly’ constrained inversion. Another issue is that the other features on the section all appear to be shaped like a bowl and shallow, with few structures persisting to depths greater than 5 km.

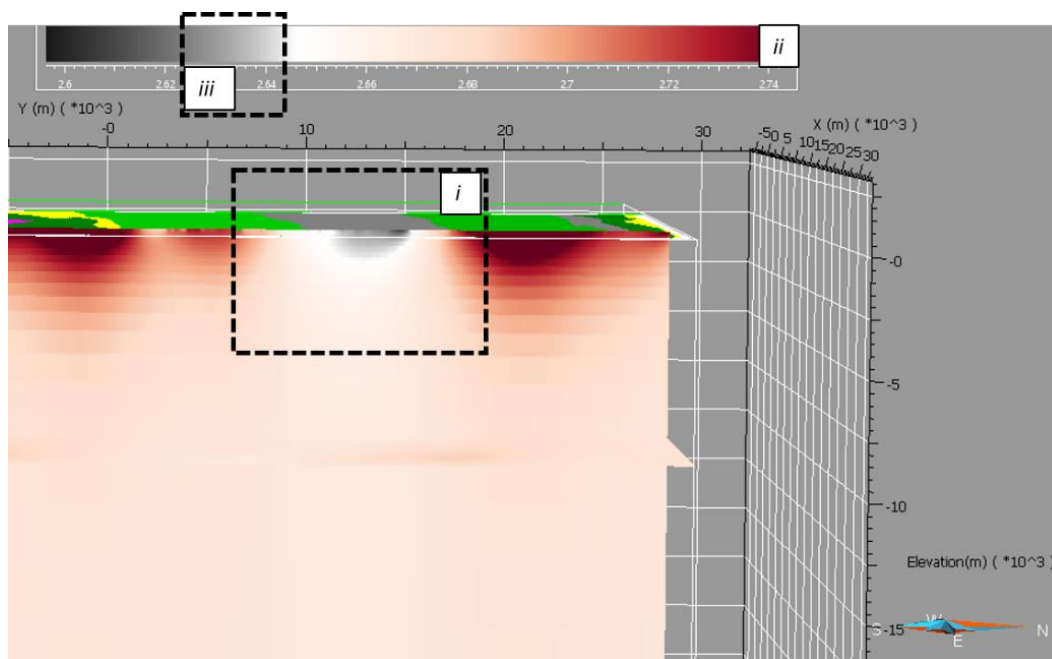


Figure 5.21. Zoomed view of the unconstrained model highlighting the feature that might be associated with the Porcupine assemblage, in this case the vertical section corresponds to the Matheson transect, which is further towards the east and the Porcupine assemblage is thinner, in agreement with other studies (i). The color legend is shown in (ii), with the range of density values for the Porcupine shown in the dashed rectangle (iii).

In the previous section (5.4.3) the density values associated with the Porcupine assemblage were approximately, 0.10 g/cm^3 (see Figure 5.21) lower than the mean

density obtained from the compilation. This discrepancy could be resolved by adding the difference in the density value in the starting model.

5.4.4. Constrained Gravity inversion II: Resolving the Source's Location and Solving the Density Problem for the Porcupine Assemblage

Figures 5.22 and 5.24 show the final model, using a depth weighting function and adding 0.10 g/cm^3 to the starting model. The depth of the Porcupine assemblage at the Shillington line is still the same (compare Figures 5.20-*i* and 5.24-*i*), with its density now being closer to the density obtained in the density property compilation (2.73 g/cm^3) as shown in Figure 5.23 and 5.24-*iii*.

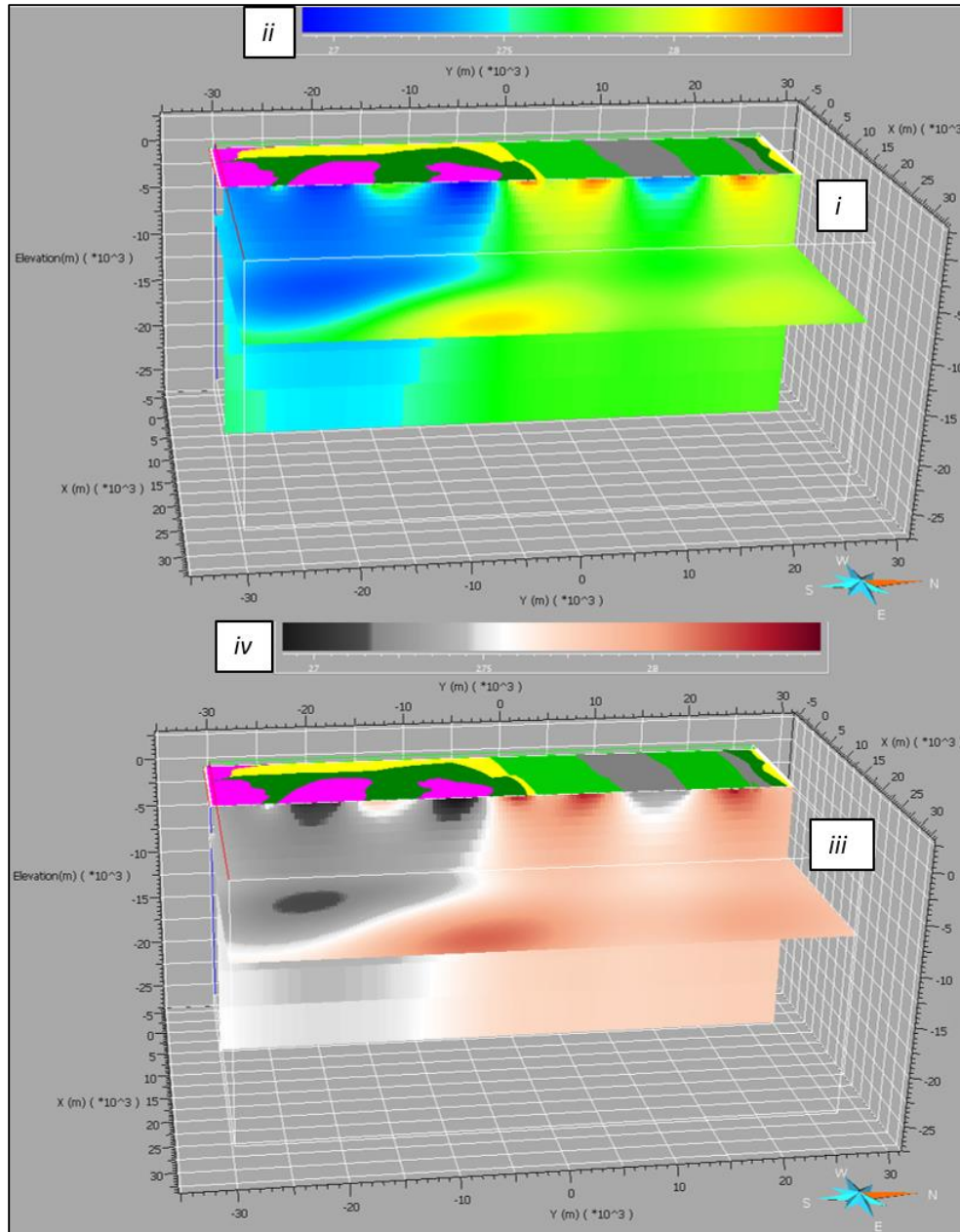


Figure 5.22. S-N vertical and horizontal sections of the depth-weighted smoothed inversion model after the density has been incremented by 0.1 g/cm^3 . The vertical section for Matheson is displayed below the surface geology map (*i* and *iii*). The model is the same as that in Figure 5.21, differing solely by the color palette (*ii* and *iv*).

The density distribution for the model of Figure 5.22 is shown in the histogram in Figure 5.23, and the distribution is the same, however the values are shifted by 0.10 g/cm^3 . The histogram still presents a bimodal pattern, with one high peak centred around the new starting model density (2.77 g/cm^3) and a second smaller peak around 2.73 g/cm^3 , which is related (but not exclusively) to the Porcupine assemblage.

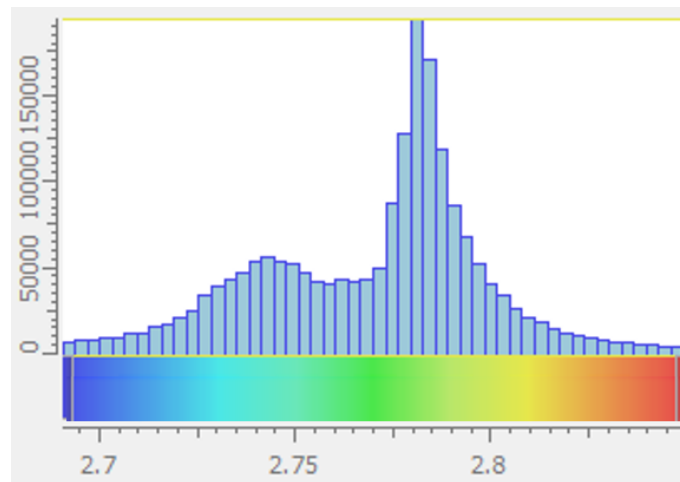


Figure 5.23. Histogram of the inverted density values with a more dense initial guess and depth-weighting and smoothing applied to the inversion model. The X axis is the density, while in the Y axis is the frequency at each density.

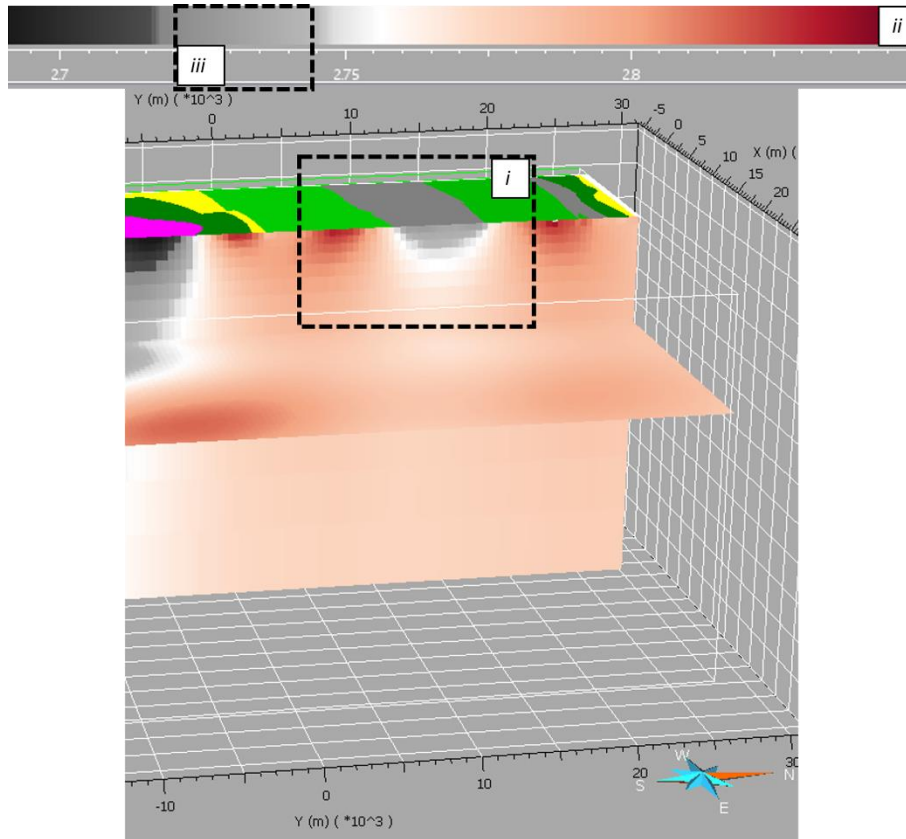


Figure 5.24. Zoomed view of the adjusted density model applied to the depth-weightened smoothed inverse model highlighting the feature that might be associated with the Porcupine assemblage (*i*) and the corresponding density values (*iii*) in the color legend (*ii*). The vertical section is for the Matheson transect.

5.4.5. Constrained Gravity inversion III: Resolving the Density Problem, the Source's Location, and the Source's Geometry for All Units – Geometry Inversion

Whereas the procedures described in the Sections 5.4.3 and 5.4.4 were able to resolve the density shift and the shallow nature of the Porcupine assemblage, they have not helped to resolve the actual shape of this assemblage. It is known from previous studies (Chapter 3 and 4) that this assemblage is bordered by two main faults, and the dip on these faults has not been quantified in the unconstrained inversions, nor has its depth been estimated with confidence.

Adjusting the initial guess did shift the Porcupine assemblage density (Section 5.4.4), but the density values for the other geological units are not in agreement with the density compilation values. For example, the ME density compilation, shows densities varying from 2.63 g/cm³ (Watabeag Lake batholith) to 2.99 g/cm³ (SR assemblage), which is a much broader range of values than seen on Figure 5.23, where the range is restricted to 2.69 g/cm³ to 2.89 g/cm³.

Considering that the procedures described to achieve the models of sections 5.4.3 and 5.4.4 was focused on resolving the Porcupine assemblage thickness, and it was not able to resolve its geometry, it would not be expected to resolve the geometry of the other units as well. Nevertheless, the depth-weighting factor perhaps might help to resolve the thickness of the other units in the MSA, since part of the model is constrained to the Porcupine assemblage thickness. Recent studies, however, have suggested the use of the same depth-weighting function parameters applied for the entire model might not be the best practice. In Cella and Fedi (2012), the depth-weighting exponent is not constant for the whole area but varies across the area depending on a structural index value

interpreted for smaller areas. In Vitale and Fedi (2020), the weight function is determined from an analysis of the spatial variability of the field. By using variable depth-weighting functions parameters in these aforementioned studies, superior results have been obtained.

All this suggests that unconstrained inversions are not adequate for obtaining inversions that will be consistent with known petrophysical, seismic and geological information. Hence, we move to constrained inversions.

5.4.5.1. 3D Geometry Inversion: Constraining the Surface Geology and Density Properties.

In the previous sections, the prior information emphasized the density and thickness of the Porcupine assemblage. In this section, the density compilation and surface geology of the entire MSA will be used to constraint the gravity inversion in what is here called Geometry Inversion A (GIA). In geometry inversions, the assigned density values of the specified units are fixed, contacts at surface are also fixed (when known), while unknown contact locations, such as those at depth, are free to move.

The starting model for the MSA, shown in Figure 5.25 is based on the ME density compilation and the mapped surface geology. The bottom of the surface geological units was defined at -500 m below sea level, which due to the elevation in the study area means that the thicknesses of the units at the surface vary from 740 to 932 meters. The assigned density underneath these units was 2.67 g/cm^3 , a value commonly used as the mean density of the crust. All contacts are initially vertical. Using known physical properties and the mapped surficial geology is similar to the approach of Williams (2009), except the VPmg algorithm is used, not the UBC-GIF algorithm.

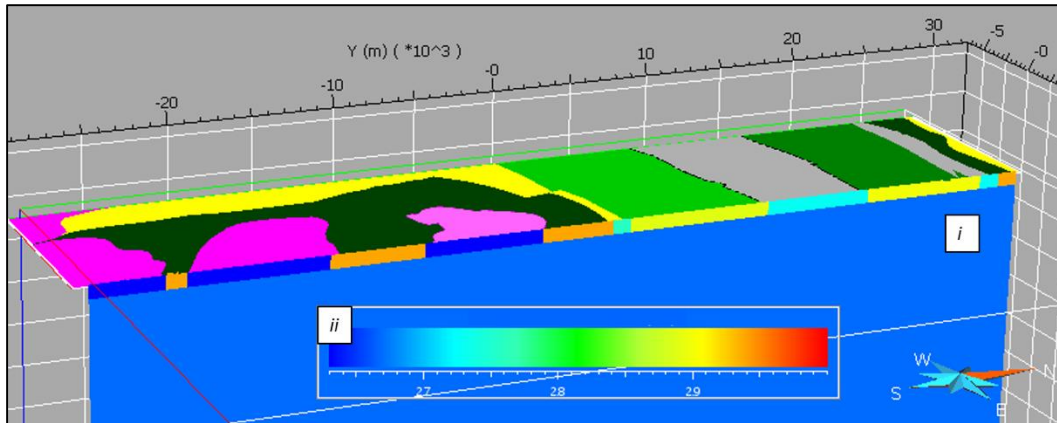


Figure 5.25. Starting density model (Model GIA) and its assigned density values associated with the assemblages and intrusions overlaid by the surface geology map (i) and the density model color legend (ii).

The GIA however stopped at the 38th iteration as shown in Figure 5.26 with a misfit as high as 18.38 mGal. The discontinuities at 10, 20, 30, and 36 iterations occurs because in these iterations, the algorithm used an L_1 norm to calculate the misfit rather than L_2 norm as used in the other iterations. An L_2 norm implies that the error follows a Gaussian probability density function, but an L_1 norm is designed to give less weight to outliers (Menke, 2012). The VPmg algorithm computes L_1 norms either every 10 iterations or whenever there is no decrease in the misfit (Fullagar, 2013), which is what is seen in Figure 5.26.

The corresponding final model is exhibited in Figure 5.27. This model is poor for a number of reasons: the misfit is poor, the Porcupine assemblage is too thick and most contacts are vertical down to 10 km depth. Allowing more iterations in the inversion does not result in a significant improvement – it simply allows the Porcupine to get a lot thicker.

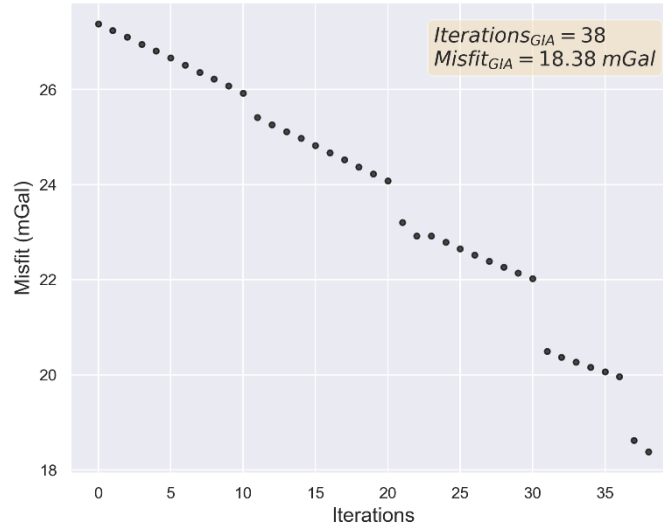


Figure 5.26. RMS misfit as a function of the iteration number for the Geometry Inversion A (GIA). The maximum number of iterations and the achieved misfit is shown on the top right of the figure.

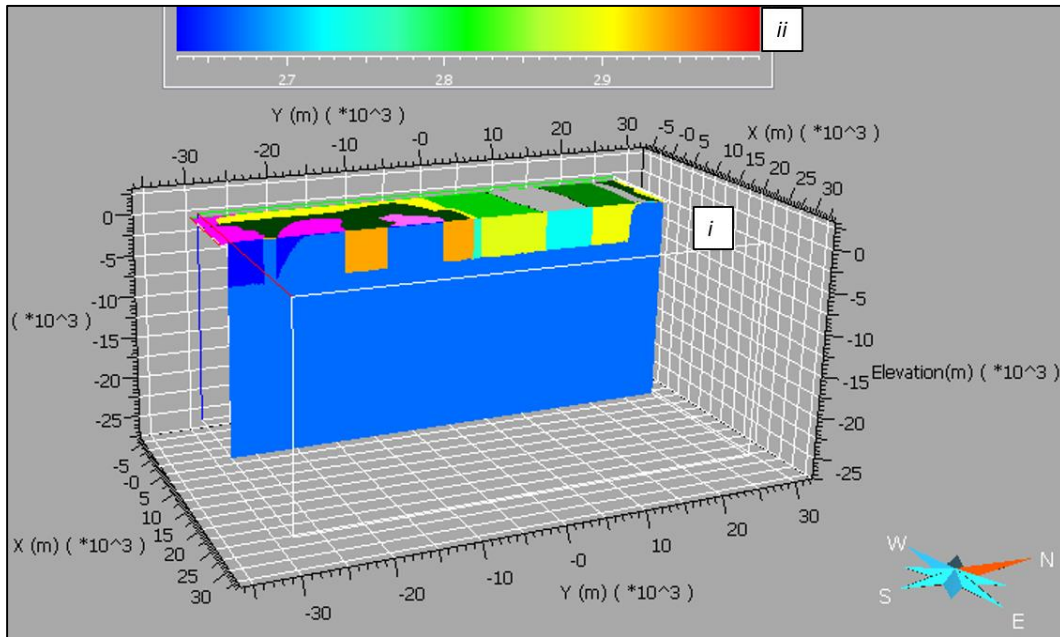


Figure 5.27. Final density model obtained from the geometry inversion A (i) and the color legend bar (ii).

5.4.5.2. 3D Geometry Inversion: Maintaining the Contacts of the Porcupine Assemblage Fixed During the Inversion for Obtaining Superior Results

One way to enhance the results from the previous section is by fixing the contacts of one unit during the inversion. In this case, the chosen one is the Porcupine, since 2D models within the PASA computed in Chapter 4 have thicknesses that are considered geologically reasonable and are consistent with the seismic data.

The PASA models of Chapter 4 do not cover the east and west parts of the Porcupine assemblage within the MSA as defined in Figures 5.1. Hence, three 2D models were added to cover the entire East-West extent of the Porcupine assemblage within the MSA. They are shown in Figures 5.28 (Section E), 5.29 (Section F), and 5.30 (Section G). Their locations are shown in Figure 5.31-*i*. Section E is located in the west of the MSA, while Sections F and G are located in the east. It is important to emphasize that these models, unlike models of the Sections A, B, C, and D, did not have seismic sections to help to constrain the depth of the Porcupine assemblage. Therefore, they might have higher uncertainty than the ones where seismic data are available.

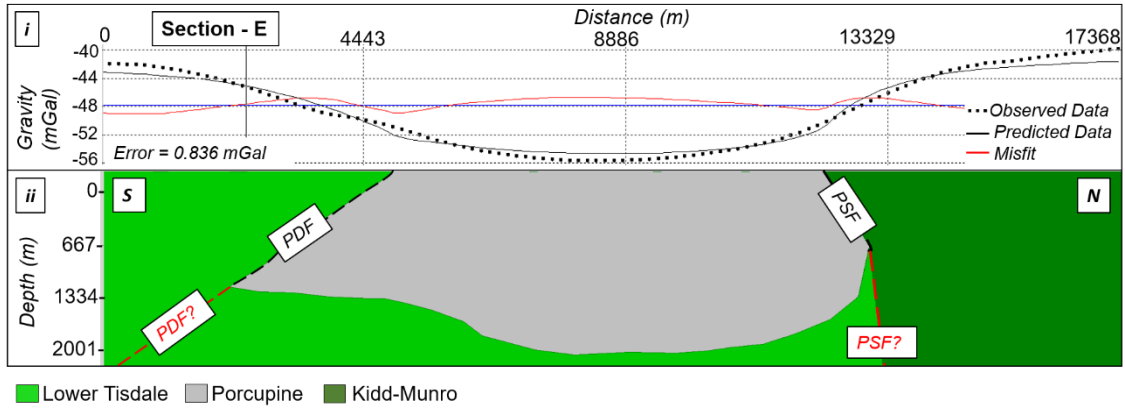


Figure 5.28. The Section E modeling showing the measured and predicted gravity data and the difference (red line) (i). The model itself providing faults localizations and the depth of the Porcupine assemblage (ii).

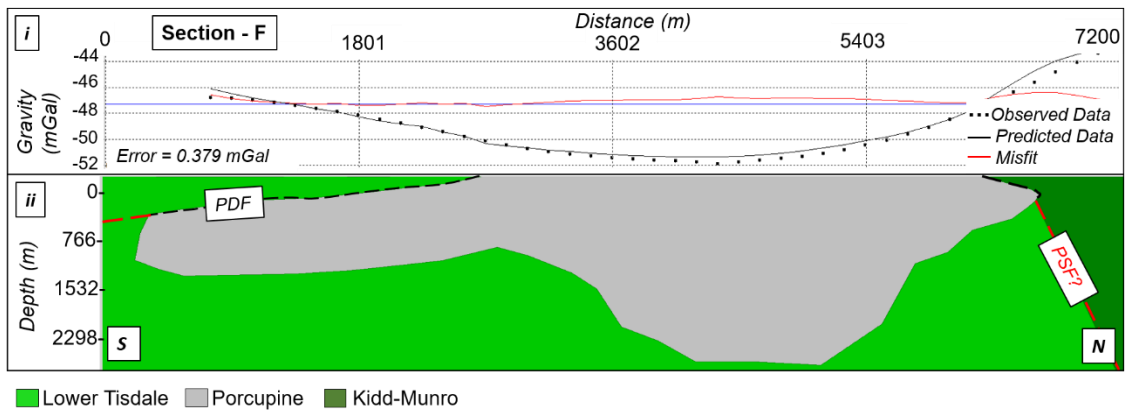


Figure 5.29. The Section F modeling showing the measured and predicted gravity data and the difference (red line) (i). The model itself providing faults localizations and the depth of the Porcupine assemblage (ii).

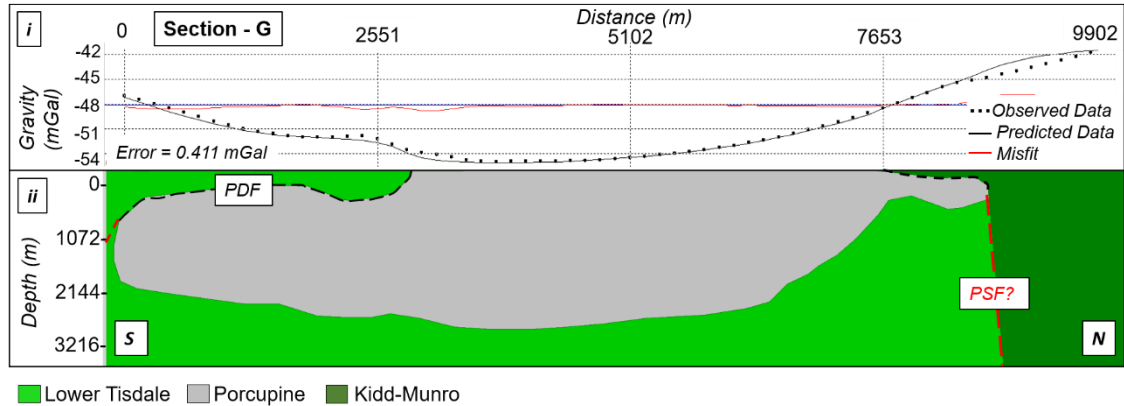


Figure 5.30. The Section G modeling showing the measured and predicted gravity data and the difference (red line) (i). The model itself providing faults localizations and the depth of the Porcupine assemblage (ii).

Combining the sections: A, B, C, and D from Chapter 4 with sections E, F, and G (see Figure 5.31-i), a 3D model of the Porcupine assemblage was constructed, as shown in Figure 5.31-iii. The 3D model was created by joining the 2D contacts of the Porcupine assemblage (Figure 5.31-ii). Moreover, as the 2D curves were geometrically simple, it was not necessary to add links to constrain the triangulation. This 3D model was computed using GOCAD software.

Obtaining a 3D gravity model by joining 2D models might introduce uncertainties in the region between the sections. This might be minimized by allowing the contacts in these regions to move in a geometry inversion. Ideally, this strategy could be used for resolving the Porcupine assemblage contacts between sections. However, as the Carr intrusion is located within this assemblage, an inversion would have difficulty positioning the contact between two sections, as two density boundaries would be allowed to move, and this would create an ambiguity or an underdetermined problem (Menke, 2012). For this reason, the 3D model of the Porcupine assemblage was solely build by joining its

contacts linearly from the 2D sections. The locations of these contacts are fixed in all subsequent work.

The Porcupine-Carr contact (inner contact) in Figure 5.31-*iii* were generated using only the surface geology as reference. The bottom of the Carr intrusion was defined as having the same shape as the top and its depth was at -500 meters. It was built in this arbitrary manner because reflectors that could be associate with this bottom contact could not be identified in section D, which is the only seismic data that traverses the Carr intrusion.

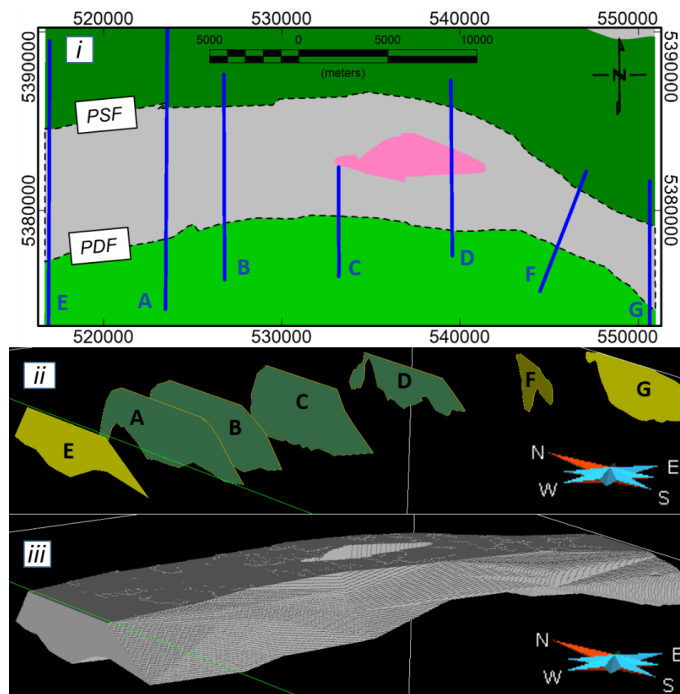


Figure 5.31. The locations of the cross sections of the Porcupine assemblage (*i*) and the 2D models on these sections distinguishing between the sections where the 2D modeling could benefit from available high-resolution seismic sections (darker green) and those where they could not (lighter green) (*ii*). At the bottom (*iii*), the created 3-D surface from the cross sections (i). The hole in the Porcupine between section C and D is the Carr intrusion.

5.4.5.3. 3D Carr Intrusion Geometry Inversion

As aforementioned, the geometry of the Carr intrusion modeling could not be addressed in the 2D modeling. In this section, we attempt to obtain more information regarding its geometry model using inversion modeling.

The Carr Intrusion Area (CAI) was delimited to the east by Section D, and to the west by Section C and the north and south boundaries were a few kilometers from the Carr surface contact. The CAI location can be seen in Figure 5.32-*ii*.

The CAI initial model was built using the Porcupine 3D model described in the previous section (Figure 5.31-*iii*). Vertically the model extends from the surface to -4000 meters as shown in Figure 5.33. Since this model is thicker than the Porcupine assemblage, it contains three geological units, the Carr, the Porcupine and the Lower Tisdale assemblages, which is below the Porcupine.

The CAI model was incised within a larger and thicker model (~ 12 000 m thick) as shown in Figure 5.34. Having a larger model surrounding the CAI includes more gravity data that can be used to give more confidence to the estimates of the density of the deeper material in the half-space. This larger model was built based on the sections A, B, C, and D, and because it covers a larger area, the Kidd-Munro assemblage to the north was included.

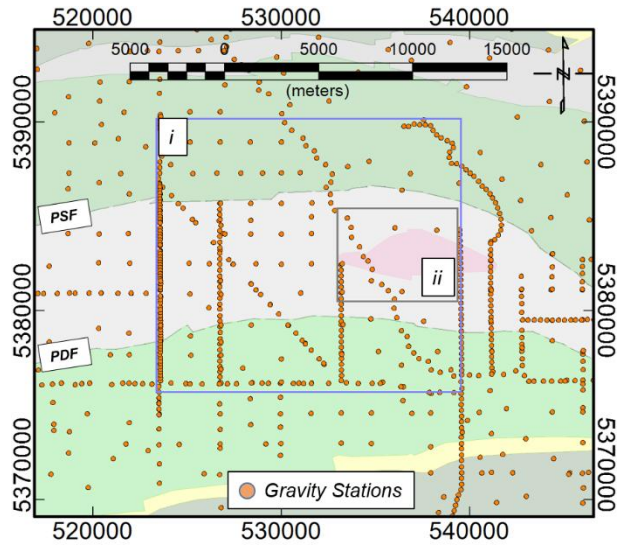


Figure 5.32. Gravity stations location in the CAI (*ii*) and in the larger model (*i*), which CAI was incised from.

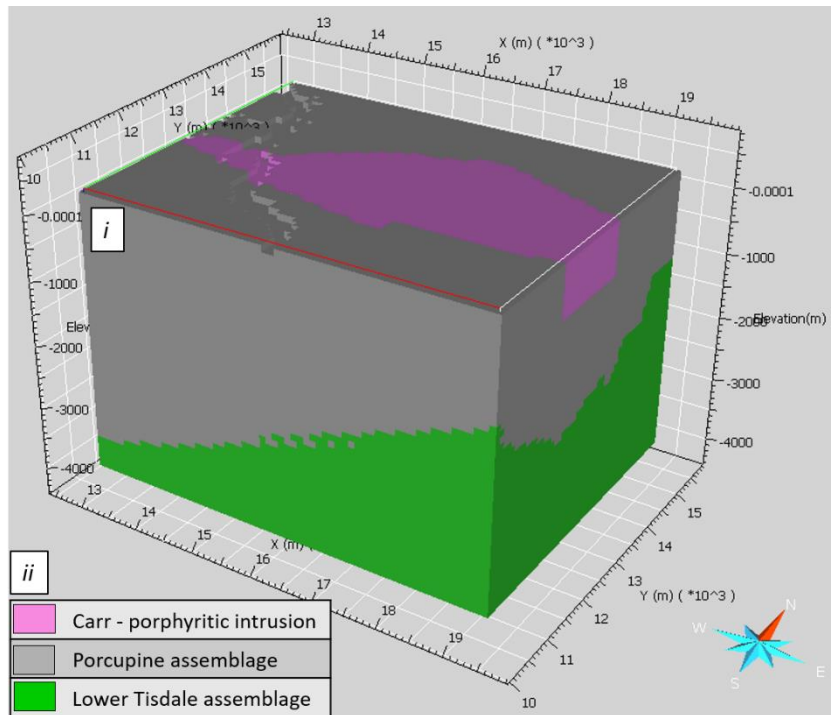


Figure 5.33. 3D CAI initial model (*i*) and the legend of the geological units (*ii*).

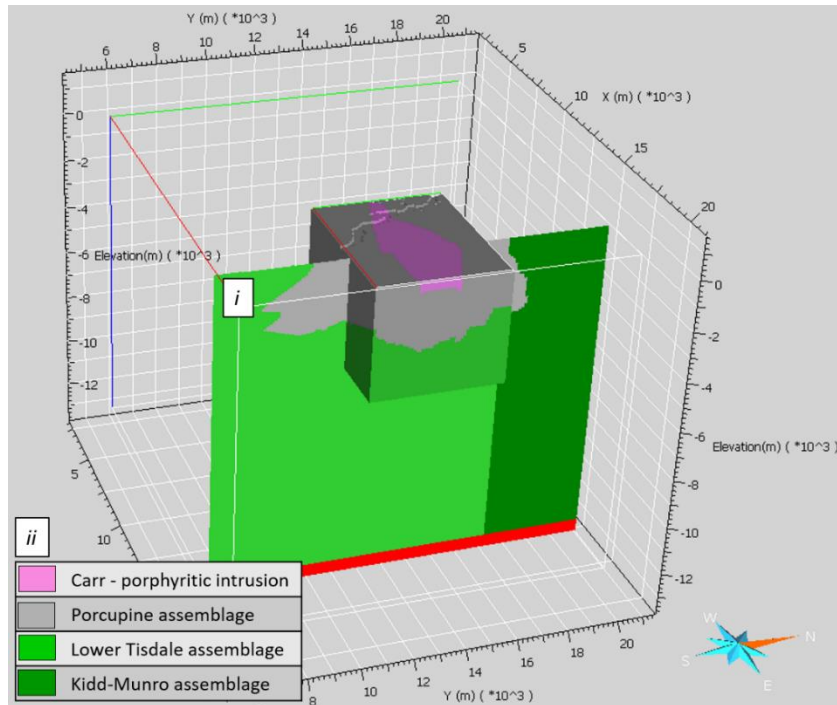


Figure 5.34. 3D CAI model embedded by a S-N cross-section of the larger model (*i*) and the legend of the geological units (*ii*).

Assigning the mean density for the Porcupine assemblage, Lower Tisdale assemblage and Carr intrusion (see Table 5.1) in the CAI starting model, and maintaining the Porcupine-Lower Tisdale contact fixed, a new geometry for the Carr intrusion was obtained. This new model might be seen in Figure 5.36-*ii*. After 17 iterations, the desirable 1 mGal RMS misfit was reached as is shown Figure 5.35. The observed and predicted data as well as the residual data are visualized in Figure 5.34. Figure 5.36, on the other hand, is comparing the shape of the Carr intrusion in the starting model (5.36-*i*) to its shape in the final model (5.36-*ii*). It is noticeable that this intrusion becomes thicker in the west and thinner to the east to match the predicted data (5.37-*ii*) to the observed data (5.37-*i*).

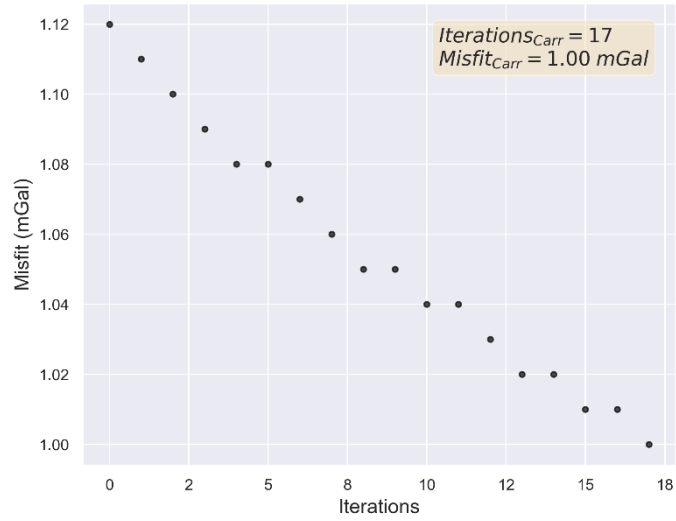


Figure 5.35. RMS misfit as a function of the number of iterations for the geometry inversion of the Carr intrusion. The number of iterations and the achieved misfit on the top right of the figure.

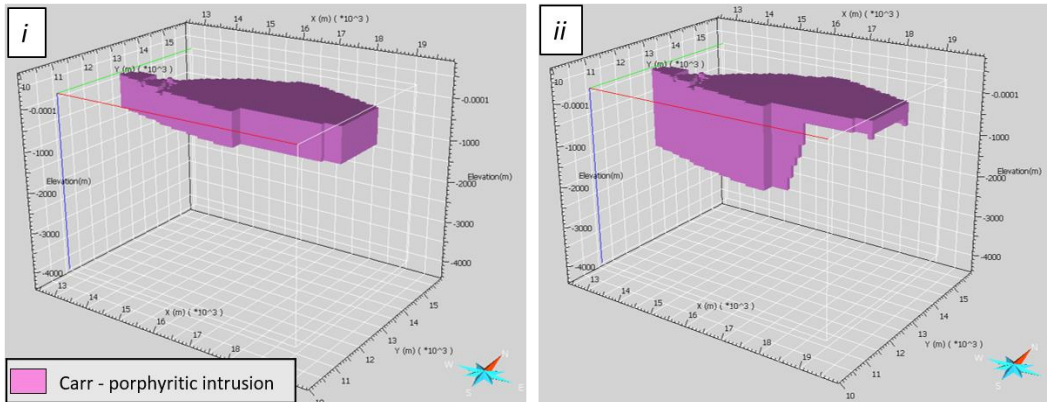


Figure 5.36. Starting (i) and final model (ii) computed for the Carr intrusion.

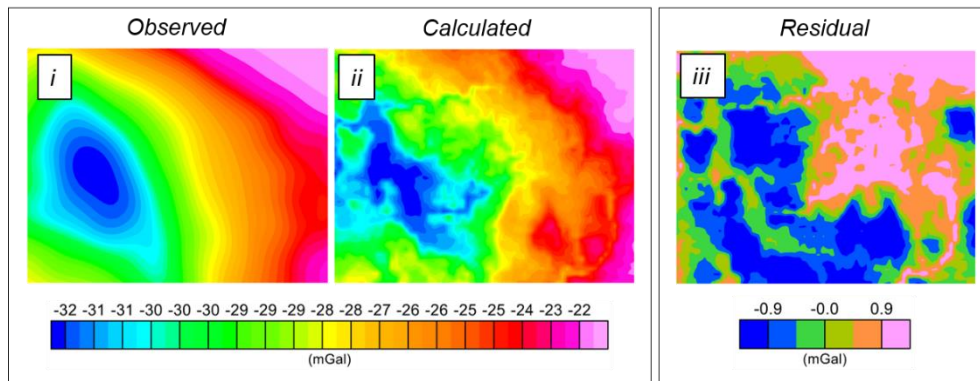


Figure 5.37. Observed data grid (i), calculated data grid (ii), and the residual data grid (iii) computed from the Carr intrusion geometry inverse model.

Despite being able to compute a model with the desirable misfit of 1 mGal, short-wavelength effects can be notice in the calculated and residual data grid in Figure 5.37. This occurs because of the combination of close spacing of the grid and rapid topography variation. This topic will be discussed in more detail in the final section of the chapter.

5.4.5.4. 3D Porcupine Assemblage Starting Model

Unlike the starting model described in the Section 5.4.5.1, where all the surface units have their bottom at -500 meters, in this section, the starting model has the geometry of the Porcupine and Carr units determined from previous modeling and fixed, as shown in Figure 5.38.

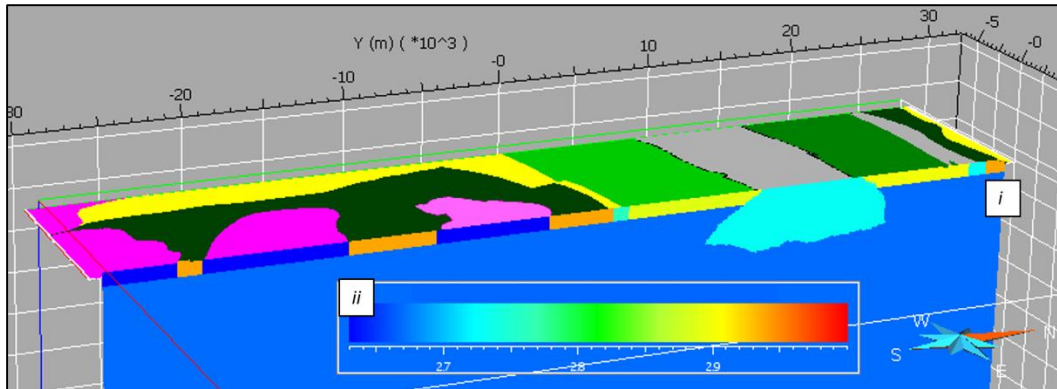


Figure 5.38. Modified starting density model and the assigned density values associated with the assemblages and intrusions overlaid by the surface geology map (i). The density model color legend is in the inset (ii). The Carr intrusion is not shown, being further to the east than this section.

5.4.5.5. Maintaining the Contacts of the Porcupine Assemblage and Carr Intrusion Fixed During the Inversion

From the starting model, described in the Section 5.4.5.4, the gravity inverse model B (GIB) was computed by adjusting all the contacts except those of the Porcupine and Carr assemblages during the inversion.

At the 76th iteration, the algorithm stopped the inversion, as it was unable to decrease the RMS misfit to be significantly less than 2.43 mGal (see Figure 5.39), which is nonetheless significantly smaller than the RMS misfit of the GIA (18.38 mGal).

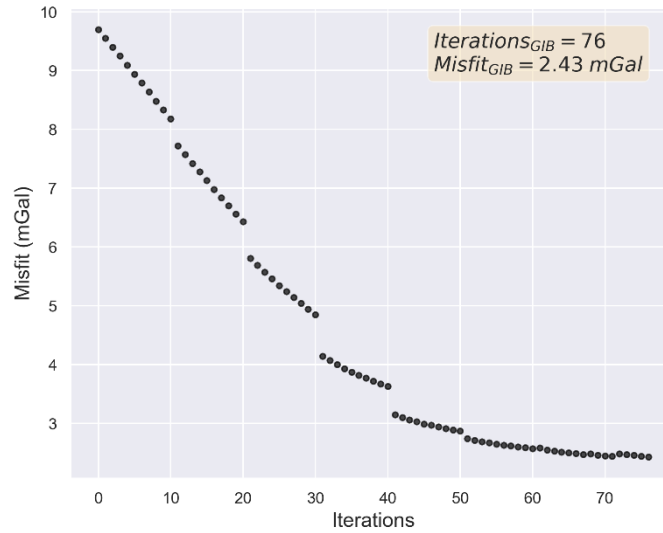


Figure 5.39. RMS misfit as a function of the number iterations for the geometry inversion B. The maximum number of iterations and the achieved misfit are shown on the top right of the figure.

Figures 5.40 and 5.41 show the final model obtained for geometry inversion B. Figure 5.40 shows the mean density of each unit, with a mean density of 2.67 g/cm^3 being used for the basement. Figure 5.40, on the other hand, is showing the geological units associated with these densities, using the same colors as the geological map.

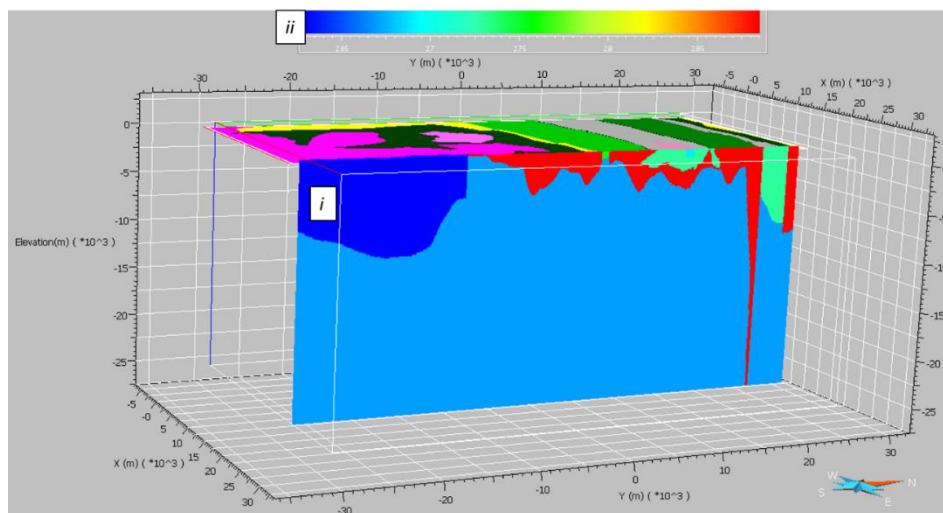


Figure 5.40. Final density model (*i*) obtained by maintaining the Porcupine assemblage and Carr intrusion contacts fixed during the inversion. Label (*ii*) highlights the density color legend bar.

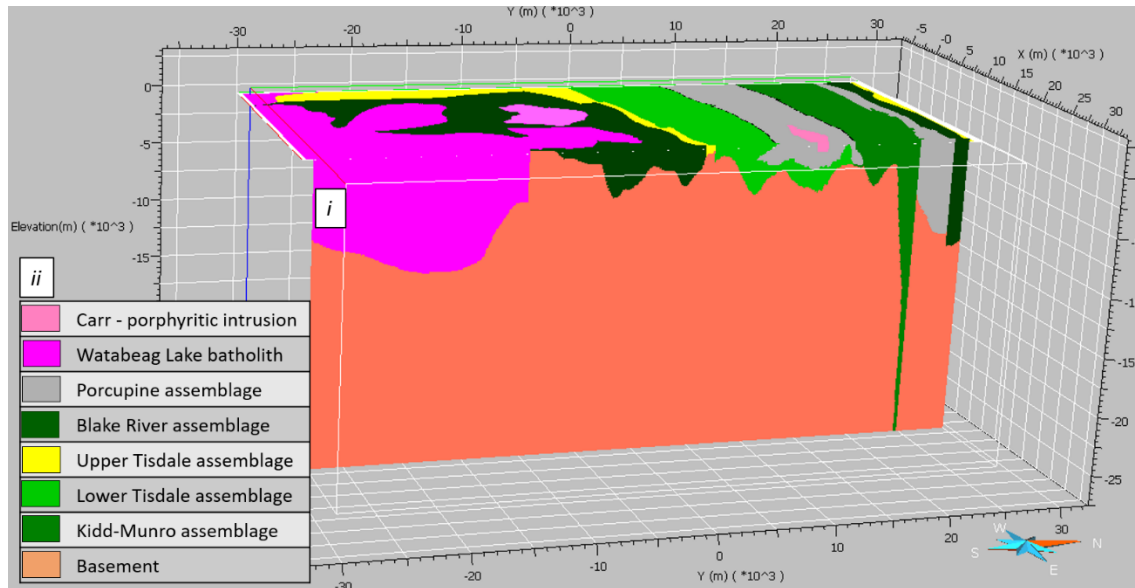


Figure 5.41. Final geological model (*i*) associated with the density model shown in Figure 5.39.

In *ii* is displayed the geology legend.

As Table 5.1 shows in the standard deviation column, there is a variability of density values for every geological unit. This suggests that the units are not homogeneous, as assumed in model GIB, but heterogeneous.

Fixing the geometry, but allowing the density within each unit to vary within a range specified in each row of Table 5.1, results in what is termed in this context a smoothed model, here designated GIBS. After this inversion, the RMS misfit was 1.84 mGal (see Figure 5.42). Figure 5.43 shows the final density model, with subtle changes in the densities evident (compared with Figure 5.40).

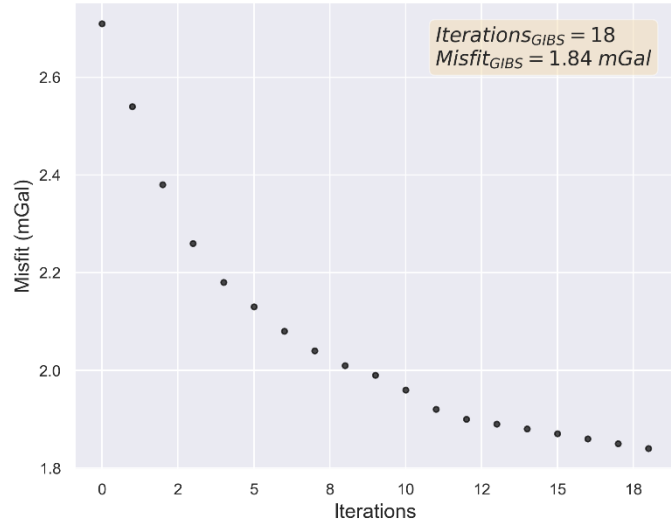


Figure 5.42. RMS misfit as a function of the algorithm iterations for the geometry inversion BS (GIBS). The maximum number of iterations and the achieved misfit on the top right of the figure.

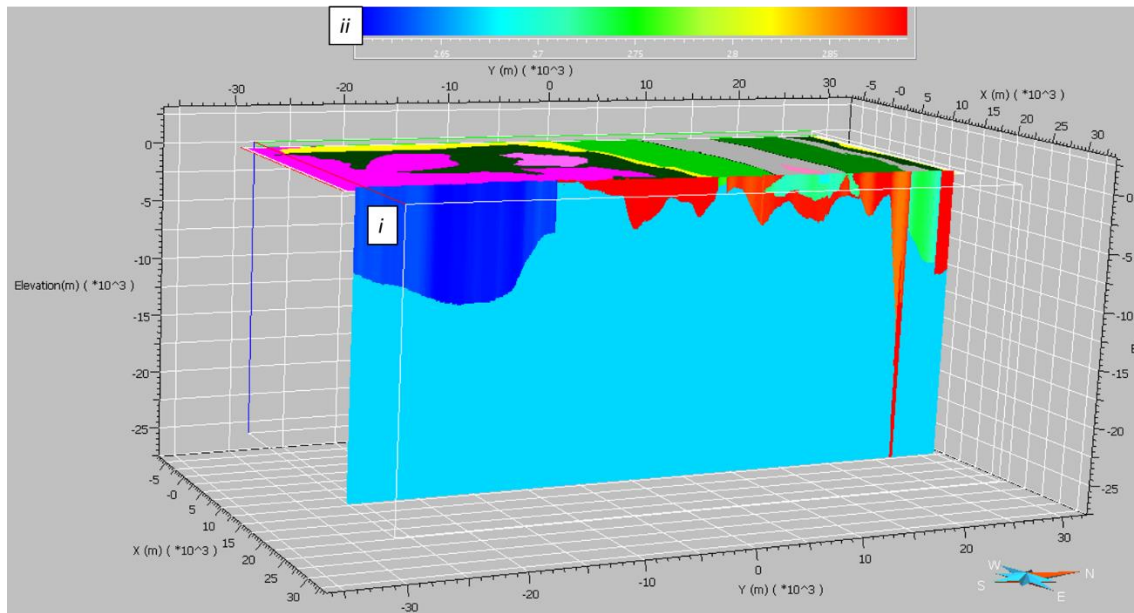


Figure 5.43. Final density model GIBS (*i*) and the density color legend bar (*ii*).

Figure 5.44 is comparing the observed data (*i*) to the calculated data (*ii*) as well as showing the residual data (*iii*). The main features, which might be thought as larger

wavelength in the grid, are very similar. However, in the calculated and as a consequence in the residual data as well, a high-frequency variation is noticeable. The absence of this variation in the observed data is because the gravity data has not been acquired in a regular grid. On the other hand, the calculated data is predicting the gravity measurement for every grid cell location (at 100 m spacing). The cause of this high-frequency variation is a consequence of rapid changes in the topography. In Figure 5.45, a smaller area (*ii*) from the MSA (*i*) is selected to show how the changes in the topography, where the gravity stations are sparser, can introduce high frequencies into the calculated data grid. The green arrows in (*iii*) are pointing to a SW-NE feature, which can be associated with the rapid changes in the topography as highlighted with a dashed line in (*iv*). This effect is removed when the grid is only sampled at the location of the gravity stations (inverted triangles) and a new calculated data grid is generated as shown in (*v*). Panel (*vi*) is exhibited the observed data for comparison. Computing the calculated data grid at the gravity stations position removed the short-wavelength effect. It is noticeable by comparing in (*v*) and (*vi*) regardless of the misfit between the observed and calculated data grids.

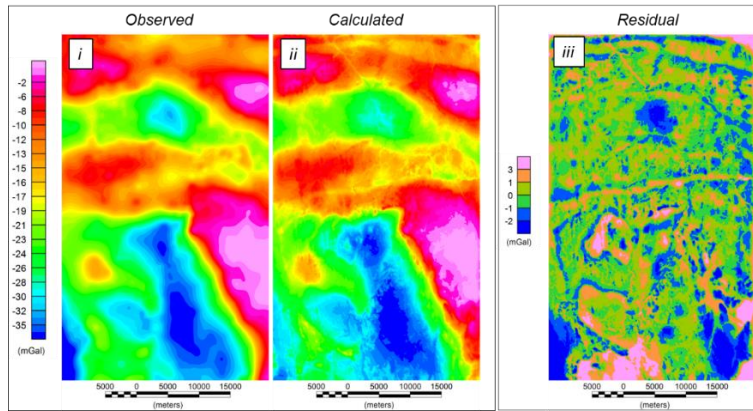


Figure 5.44. Observed data grid (*i*), calculated data grid (*ii*), and the residual data grid (*iii*) computed from the final density model BS.

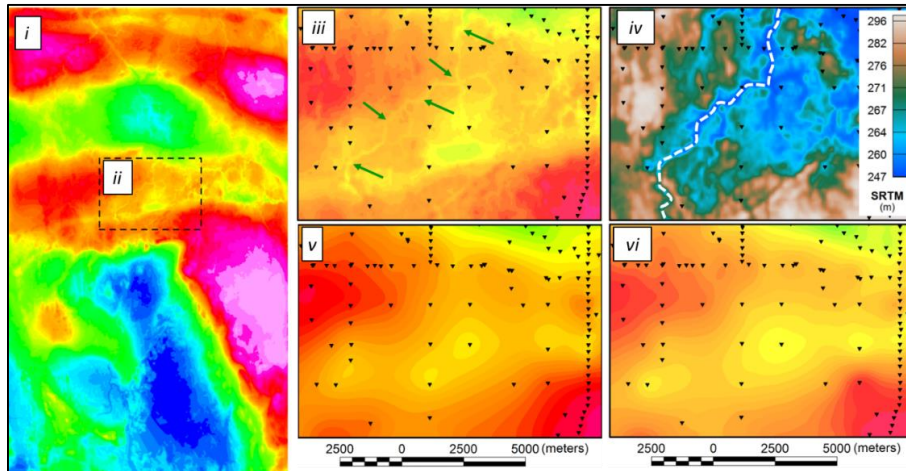


Figure 5.45. Smaller area (*ii*) selected from the MSA (*i*) to illustrate in greater detail the topographic effect in the calculated data grid (*iii*) in places where there are rapid changes in the topography (for example the lows shown with green arrows). On the topographic map (*iv*), this corresponds to the location of the incised valley marked with the dashed white line. Note as well that the gravity stations (inverted triangles) are sparser than the topographic variations. For comparison, panel (*vi*) shows the observed data grid, which is similar in wavelength to panel (*v*), which shows the calculated data (*iii*), but only sampled at the gravity station locations (inverted triangles).

Sampling the calculated grid at the gravity station location (shown on Figure 5.9) and computing a new grid using the same grid cell size as the observed grid (which is 100 m), the high-frequency topographic effect is removed. The new calculated data grid (Calculated GIBS), shown on Figure 5.46*ii* generates a map much closer to the observed data (Figure 5.46*i*). Moreover, the RMS misfit (Figure 5.46*iii*) decreases from 1.84 mGal to 1.58 mGal.

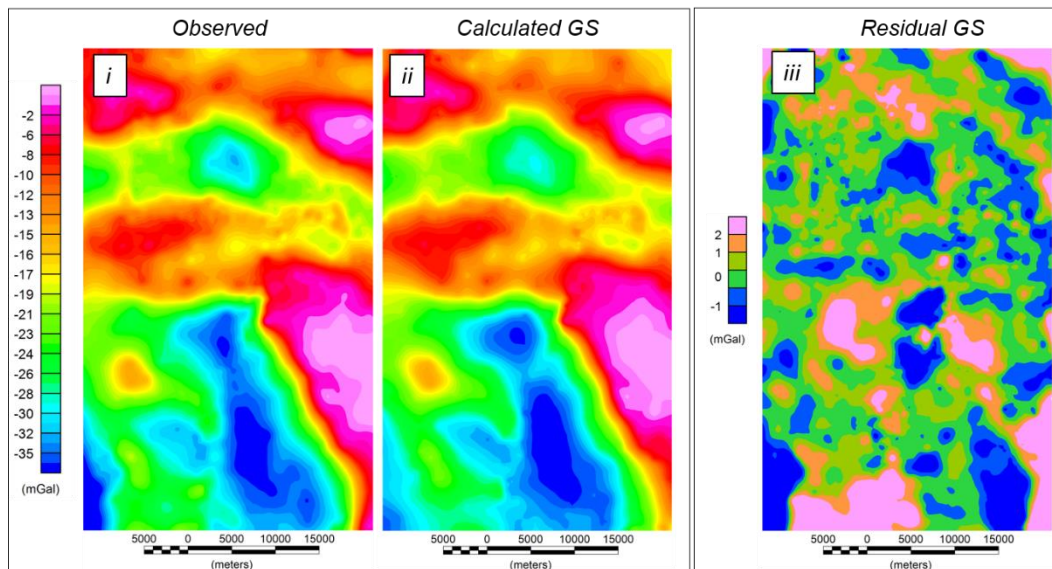


Figure 5.46. Observed data grid (*i*), calculated data grid (*ii*), and the residual data grid (*iii*) computed from the final density model GIBS when the gravity data are gridded from data only at sampled at the gravity station locations.

In all types of 3D inversion (geometric, unconstrained, property inversions), the irregularity of the gravity data spacing plays a role in the data misfit. Because the CGDB gravity stations are irregularly distributed, the final RMS misfit should only be calculated at the locations where there are actual gravity stations. If the inversion is working on an

interpolated grid, then the RMS misfit calculated by the inversion should be considered an intermediate product for use only by the inversion.

5.5. Conclusions

The results in this chapter illustrate how the characteristics of the model and the RMS misfit changes as more constraints are added. The added constraints and changes to the model are summarized in Table 5.2 and discussed below.

The first computed model (Figure 5.15) was an unconstrained smoothed model, with the target RMS misfit goal of 1 mGal being achieved at the 34th iteration (Figure 5.13). It was anticipated that the unconstrained model might provide an idea of the three-dimensional geological setting. However, the smoothed model seems to provide unrealistic results for geological features, at least for those features that can be compared with existing information. For example, previous studies suggest that the Porcupine assemblage is significantly thinner than this model indicates. In addition, the density range is only very roughly the same as the range of densities spanned by the physical property compilation (Table 5.1), indicating that the densities of the model is unrealistic.

The second model, which is still a smoothed model, also has a depth weighting function applied during the inversion. The weighting function parameters were adjusted such that the thickness of Porcupine assemblage on the Shillington line was consistent with the estimates from the previous study. This model still seems lacking in resolving

the density property since its variability is lower in comparison to the density property values. In addition, the geometry of the sources still does not seem realistic. The one possible improvement is to resolve the Porcupine assemblage's thickness at different locations, but this is also inconsistent with the known dip in the south edge at the Porcupine-Destor fault. The misfit and number of iteration were very similar to those obtained for the first model. However, the average density of the Porcupine assemblage was unrealistically small.

The third model was to account for the incorrect density of the Porcupine assemblage, by adding 0.10 g/cm^3 to the density of the starting model. This resulted in density values closer to the values obtained in the density compilation of 2.73 g/cm^3 . In this way, the density property was resolved for the Porcupine assemblage. The depth of the Porcupine was similar, as with the second model, the depth weighting was adjusted to give the expected depth. However, the depths of other features were all very similar to that of the Porcupine, which is unrealistic. Like the first and second model, the third model had a range of density values that was inconsistent with the known range.

The fourth model, called GIA, was computed by constraining the surface geological contacts and the density property for all units. Despite having these two valuable constraints applied in the inversion, the inversion algorithm could not obtain a RMS misfit lower than 18.38 mGal, which is 18 times larger than the estimated noise level. Moreover, the model itself is unrealistic since most of the units have the same thickness (see Figure 5.27) and most interfaces are vertical.

The GIA model was improved by adding seismic interpretation to constrain the contacts of the Porcupine assemblage. These seismic reflectors were also used to

constrain the contacts between the Porcupine and the Lower Tisdale and the Porcupine and the Kidd-Munro in the 2D forward modeling described in Chapter 4. The shape and depths of the contacts from the 2D modeling were used to specify the initial 3D model on the sections, with linear interpolation of the contacts being used between the sections. The contact between the Porcupine and the Carr intrusion was resolved by inverting the data of a small area containing the Carr (see Section 5.4.5.3). Keeping all these contacts of the Porcupine assemblage fixed during the inversion, a superior model was computed (called GIB). The RMS misfit obtained in this case was 2.43 mGal (Figure 5.39) and the geological features seem more realistic. In GIB, there is an enhancement in the variability of the units' thickness (Figure 5.40/5.41) since the density property compilation was also used as a constraint. However, in this model, only the density mean for each geological unit has been applied (Table 5.1).

The last model (GIBS) was computed by carrying out a property inversion with the starting model being GIB. This property inversion allowed the density of each cell within a unit to vary up to one standard deviation away from the mean (Table 5.1). As it was a property inversion, the geometry of the contacts of the units did not change, only the density of each cell was adjusted. The obtained RMS misfit for this inversion is 1.84 mGal (Figure 5.42) or 1.58 mGal if only the RMS misfit calculated at the gravity station locations are taken into account. In this model, the density in the units is heterogeneous, which is more realistic geologically.

Table 5.2 – Table of results showing the misfit and characteristics for each of the models.

Geological constraints applied	RMS misfit (mGal)	Character of resulting model
Unconstrained	0.97	<ul style="list-style-type: none"> • Porcupine assemblage too thick; • Unrealistic model - Features in the model have a bowl shape (unit geometry not preserved).
Depth weighting based on previous study	0.99	<ul style="list-style-type: none"> • Porcupine assemblage's thickness is appropriate; • Porcupine assemblage's density is inappropriate; • Unrealistic model - Many features in the model have a bowl shape.
Depth weighting and an appropriate density for the Porcupine Assemblage	0.99	<ul style="list-style-type: none"> • Porcupine assemblage's thickness is appropriate; • Porcupine assemblage's density appropriate; • Unrealistic model - Many features in the model have a bowl shape.
Density property and surface geological contacts (GIA)	18.38	<ul style="list-style-type: none"> • RMS misfit excessively high; • Unrealistic model - Features in the model have a rectangular shape.
Density property*, surface geological contacts, seismic data (GIB)	2.48	<ul style="list-style-type: none"> • Porcupine assemblage's geometry, depth and density properties consistent with constraints; • More realistic model but still homogeneous.
Density property**, surface geological contacts, seismic data (GIBS)	1.84/1.58	<ul style="list-style-type: none"> • Porcupine assemblage's geometry, depth and density properties consistent with constraints; • Realistic model and heterogeneous.

*Density mean of the compiled samples for each unit.

**Density bounds are one standard deviation from the mean.

The characteristics in Table 5.2 summarize how the quality of the model has changed as more data/information are added as constraints. However, this can make it a challenge to obtain a very low misfit. This is most evident when the density property and surface geological contacts were fixed, with the misfit increasing to 18.38 mGal. However, fixing the geometry of the contacts of the Porcupine assemblage according to the seismic constraints resulted in a significant decrease in the RMS misfit to 2.48 mGal. The most realistic model was obtained by preserving the geometry of these contacts, but allowing petrophysical variability consistent with the density compilation.

Even though the misfit might be used as a guide throughout the modeling workflow, it is not the only information that should be considered. The geological feasibility of the model should provide strong guidance towards a good quality model

Chapter 6: Deloro Assemblage Hypotheses

The modeling results indicate that it is possible to determine additional features if the features which have a strong impact on the gravity response (generally the shallower features) are modeled first and then fixed in subsequent modeling.

In the previous chapters, strong seismic reflections (*SR*) located at depths between 8 and 5 kilometers have been neglected in sections C and D (these are labelled *SR7* and *SR9* in Figure 6.1). In section B, there is also a strong reflector *SR5*, the south part of which was attributed to the base of the Porcupine assemblage, but might also be interpreted as the top of the Deloro, with no reflection at the base of the Porcupine being evident. Furthermore, the entire length of *SR3*, in section A, was interpreted and modeled as the bottom of the Porcupine assemblage. This interpretation makes the Porcupine quite thick on this section, so another interpretation is to have this reflector as the top of the Deloro. Although *SR3* and *SR5* are located in different depths, they are very similar geometrically. Therefore, in both cases it would be a more consistent explanation if they had a similar geological interpretation as the top of the Deloro.

Previous studies have suggested that the Deloro assemblage might be located underneath the Porcupine assemblage. For example, Haugaard et al. (2021) suggested that the deep reflector in section D might be the top of the Deloro assemblage. The Deloro assemblage (2730 to 2724 Ma) is composed of intermediate to felsic volcanic rocks and iron formations (Ayer et al., 2002). One hypothesis would be that the prominent reflector at the top of the Deloro assemblage that shallows to the west might be caused by the iron formation, since studies have suggested that the Deloro assemblage is capped by iron

formation (Ayer et al., 2002; Berger et al., 2011). Furthermore, the Deloro assemblage has been mapped at surface about 50 kilometers to the west of these sections, which would be in agreement with a Deloro that gets shallower, since the reflectors also shallow towards the west (see Figure 6.1).

This chapter tests the hypothesis that *SR3*, *SR5*, *SR7*, and *SR9* represent the top of the Deloro assemblage.

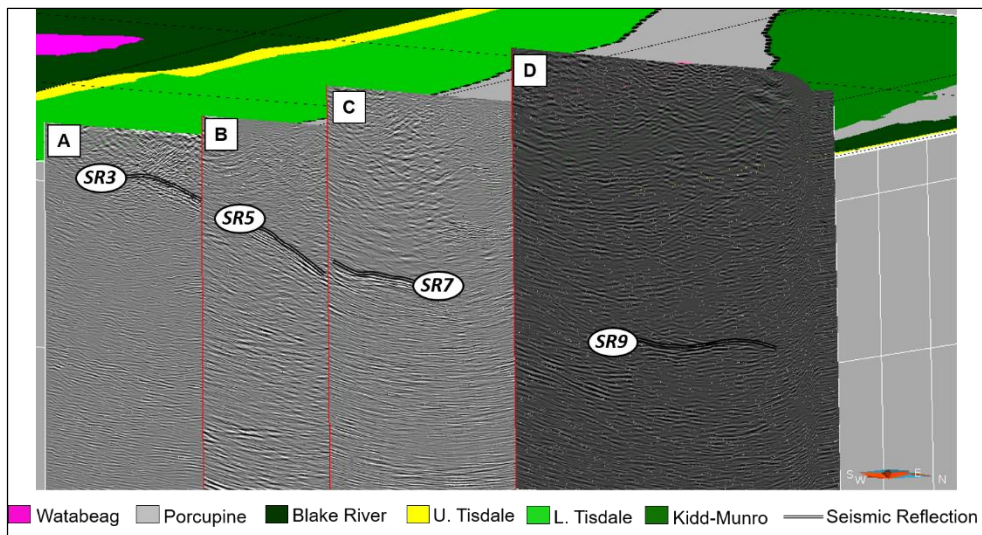


Figure 6.1. View from below looking NW to the high-resolution (R2) seismic sections overlaid by the surface geology map. The deeper reflections are identified on the seismic sections (*SR3*, *SR5*, *SR7*, and *SR9*).

Even though the Deloro assemblage's rocks have not been mapped in the MSA, the Metal Earth project compiled 30 density property samples to the west of this area. Figure 6.2 shows a histogram of the density samples compiled by the ME project.

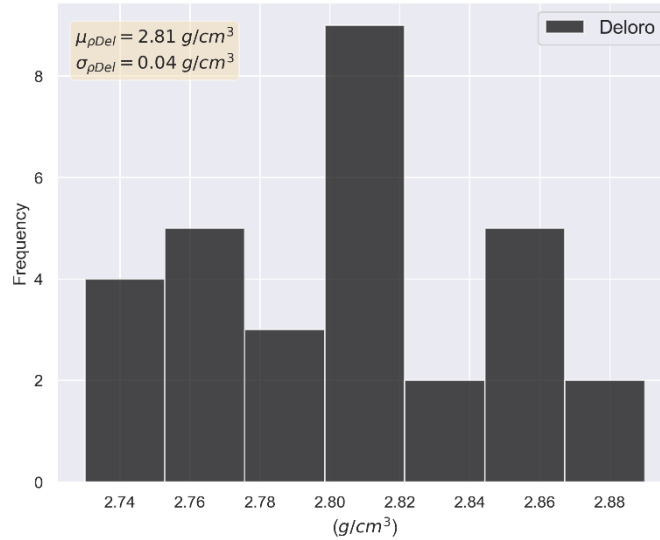


Figure 6.2. Histogram of the measured density values of the Deloro assemblage with the mean ($\mu_{\rho Del}$) and the standard deviation ($\sigma_{\rho Del}$) given in the top left of the figure.

The 30 samples provided the density mean of $2.81 \pm 0.04 \text{ g/cm}^3$ for the Deloro assemblage. These values will be used in the gravity modeling.

6.1. 2D Models

Assigning the density mean for the units cut by the four gravity profiles, and using the surface geological map, four 2D models were obtained as shown in Figures 6.3, 6.4, 6.5, and 6.6. These models were based on the seismic reflections evident on Figure 6.7, which were interpreted as only highlighting a limited extent of the upper Deloro interface (thicker black lines on Figures 6.3 to 6.6). This limited interface was extended to the north and south as part of the GM-SYS modeling, which also included adjusting the other interfaces without seismic reflections until the RMS errors are comparable to the values reported in Chapter 4.

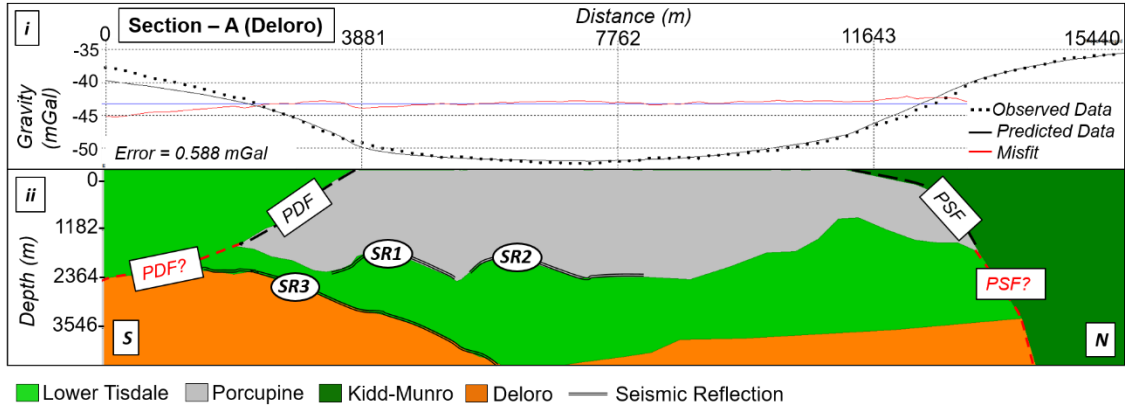


Figure 6.3. Section A model with the Deloro included. The measured and predicted gravity data and the difference (red line) (i). The modified model showing faults localizations and seismic reflections – SR (ii).

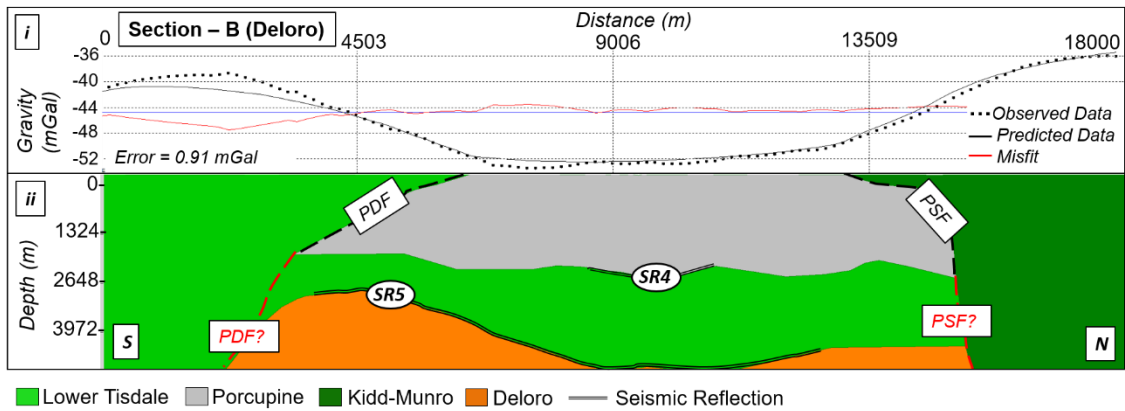


Figure 6.4. Section B model with the Deloro included. The measured and predicted gravity data and the difference (red line) (i). The modified model showing faults localizations and seismic reflections – SR (ii).

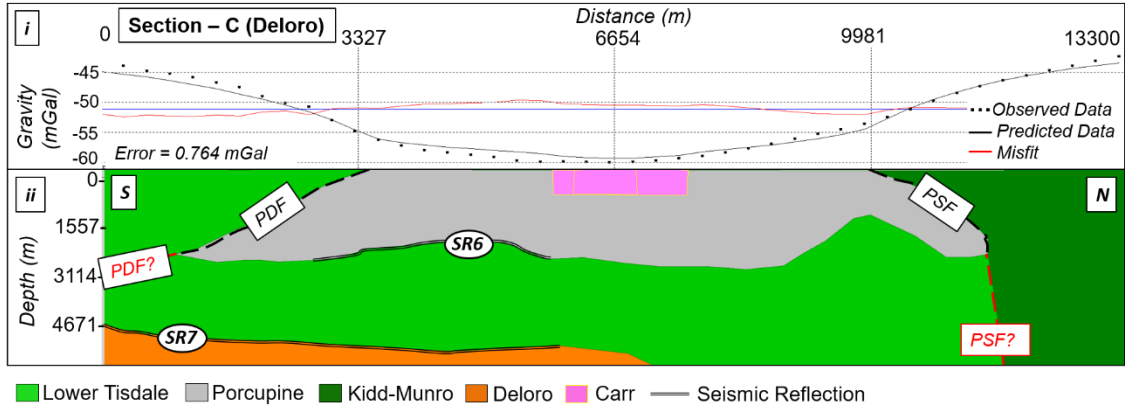


Figure 6.5. Section C model with the Deloro included. The measured and predicted gravity data and the difference (red line) (i). The modified model showing faults localizations and seismic reflections – SR (ii).

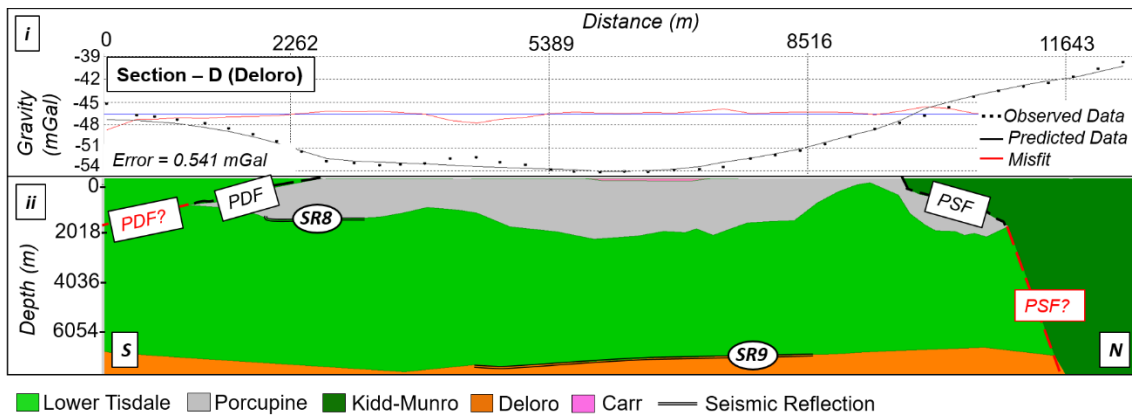


Figure 6.6. Section D model with the Deloro included. The measured and predicted gravity data and the difference (red line) (i). The modified model showing faults localizations and seismic reflections – SR (ii).

In Section D the changes made to the Porcupine assemblage’s geometry and thickness are not noticeable compared to the model with no Deloro shown in Figure 4.19. This is because the SR9 in section D is much deeper than the other reflections associated with the Deloro assemblage, so its gravitational effect at the surface is smaller. However,

in the other three sections (A, B, and C), shown in Figures 4.13, 4.15, and 4.17), the Porcupine geometry is different from the geometries shown on the sections in this chapter. This is because the Deloro assemblage has a lower density than the Lower Tisdale assemblage does. When the Deloro is inserted into the section on the western lines, the Porcupine assemblage displays a more consistent depth along the strike extent, which is reasonable geologically.

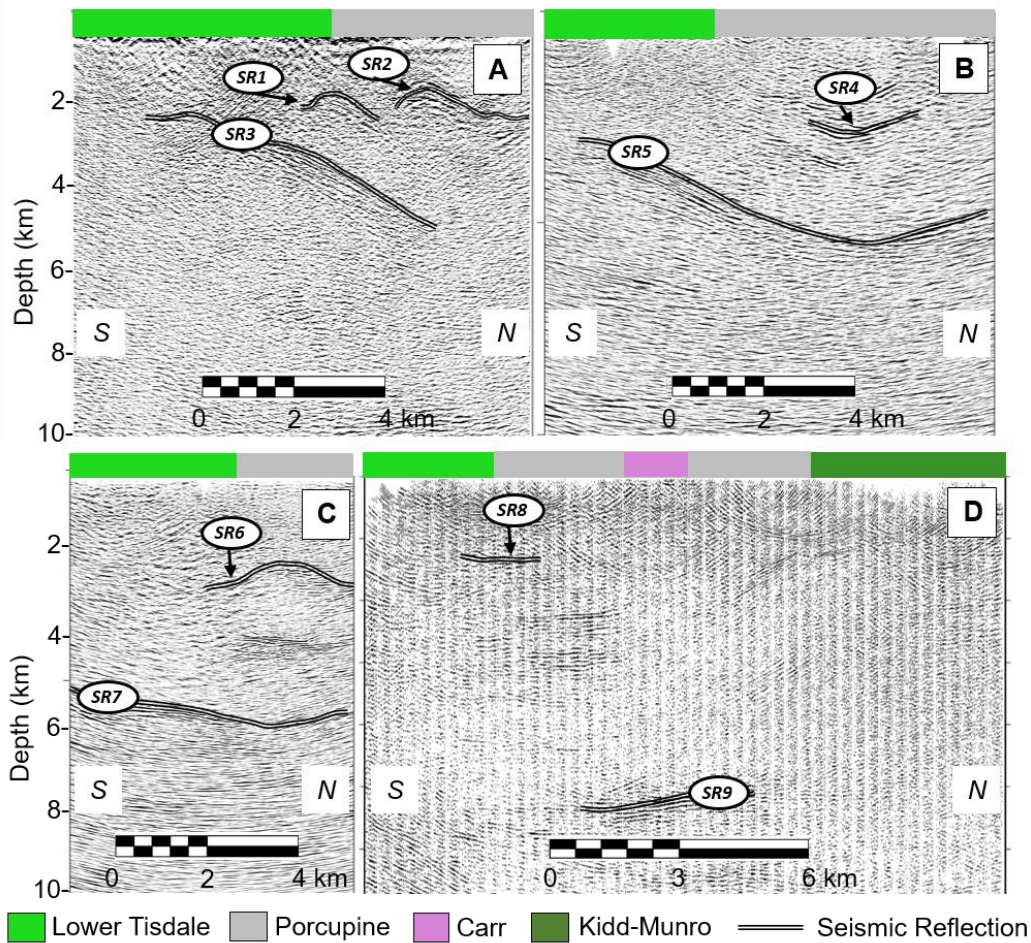


Figure 6.7. High-resolution seismic-section interpretation indicating the seismic reflections (SR) used in the modeling.

The 2D models misfits in the scenarios without and with the Deloro are both comparable, so either scenario explains the data equally well when considering only the misfit. However, the Deloro-included scenario explains more of the seismic reflectors. Table 6.1 summarizes the main differences in the interpretation of the seismic sections between the original interpretation (Chapter 4), and by including the Deloro assemblage into the models. A key difference is the revised interpretations of SR3 and SR5.

Table 6.1 – Seismic interpretation comparison between the original interpretation and by including the Deloro assemblage.

Seismic Reflection/Section	No Deloro assemblage	Including Deloro assemblage
<i>SR1/A</i>	Not interpreted	Bottom of Porcupine assemblage
<i>SR2/A</i>	Not interpreted	Bottom of Porcupine assemblage
<i>SR3/A</i>	Bottom of Porcupine assemblage	Top of Deloro assemblage
<i>SR4/B</i>	Not interpreted	Bottom of Porcupine assemblage
<i>SR5/B</i>	Bottom of Porcupine assemblage	Top of Deloro assemblage
<i>SR6/C</i>	Not interpreted	Bottom of Porcupine assemblage
<i>SR7/C</i>	Not interpreted	Top of Deloro assemblage
<i>SR8/D</i>	Bottom of Porcupine assemblage	Bottom of Porcupine assemblage
<i>SR9/D</i>	Not interpreted	Top of Deloro assemblage

6.2 Homogeneous 3D Models

As in Chapter 5 (Section 5.4.5.2), the 2D models were combined to construct a 3D model. Model Alpha (α) was built based on the sections A, B, C, and D described in Chapter 4, while Model Beta (β) was built using the 2D sections A, B, C, and D proposed in this chapter. Both models incorporated the same geometry and thickness of the Carr intrusion obtained in the Section 5.4.5.2. The gravity data and model area span the area shown in Figure 5.32 (i), which is slightly smaller than the PASA.

In Model α , the Deloro assemblage was not included, but Model β was built including this assemblage. Figure 6.8 shows three-dimensional perspective views of Models α and β on the left and on the right, respectively.

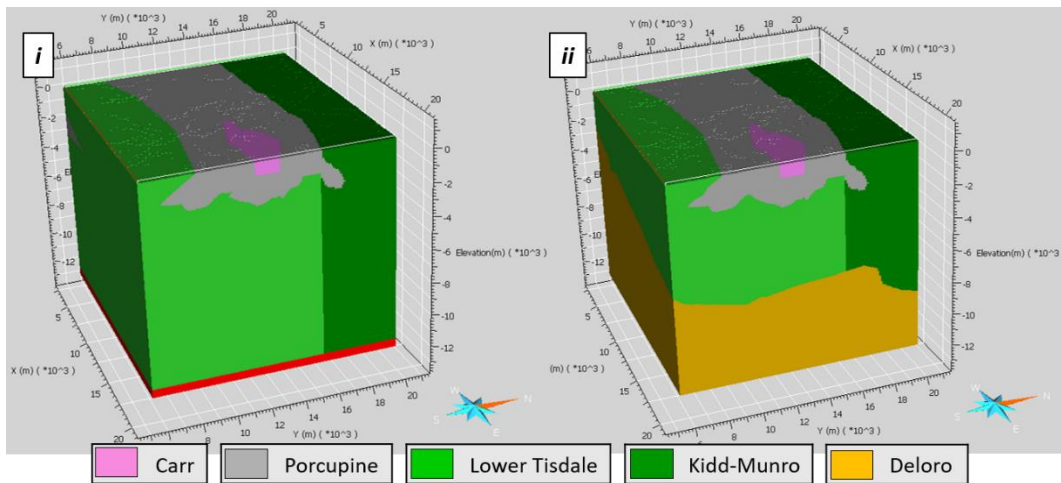


Figure 6.8. 3D models generated from the 2D modeling sections. On the left (i) Model α and on the right Model β (ii). Both models are viewed from the southeast.

The character of the Porcupine and Deloro assemblage are highlighted in Figure 6.9. The thickness of the Porcupine assemblage is greatest in Model α , particularly to the west (Figure 6.9-*i*). For Model β , the Porcupine is generally thinner than 2000 meters (see Figure 6.9-*ii*). The shallowing of the Deloro to the west is also evident on Figure 6.9-*ii*.

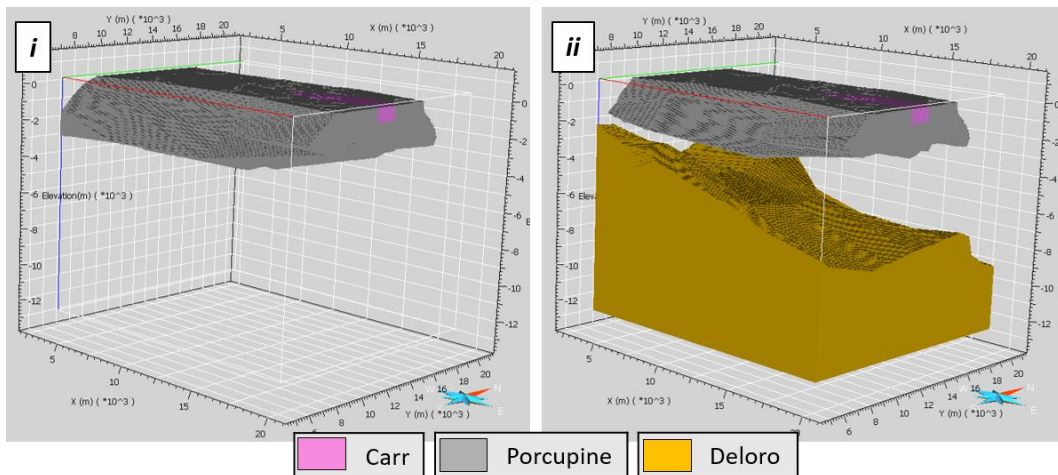


Figure 6.9. 3D models highlighting the Porcupine and Deloro assemblages generated from the 2D modeling sections. On the left (*i*) the Porcupine assemblage in Model α , and on the right the Porcupine assemblage and the Deloro in Model β . The geological legend is shown on the bottom and the view is from the southwest.

The forward gravity response for the models α and β were then computed at the gravity stations (GS) returning similar RMS misfit values: 4.16 mGal and 4.30 mGal for α and β , respectively. Figure 6.10, for Model α , shows the calculated data grid (*ii*) and the residual data grid (*iv*). Like in Section 5.4.5.5 in the previous chapter, the calculated and the residual grids were resampled at the gravity station positions (Figure 6.10-*iii* and *v*), since the gravity stations were not regularly distributed. These grids might be compared to the observed data grid in the same figure (*i*).

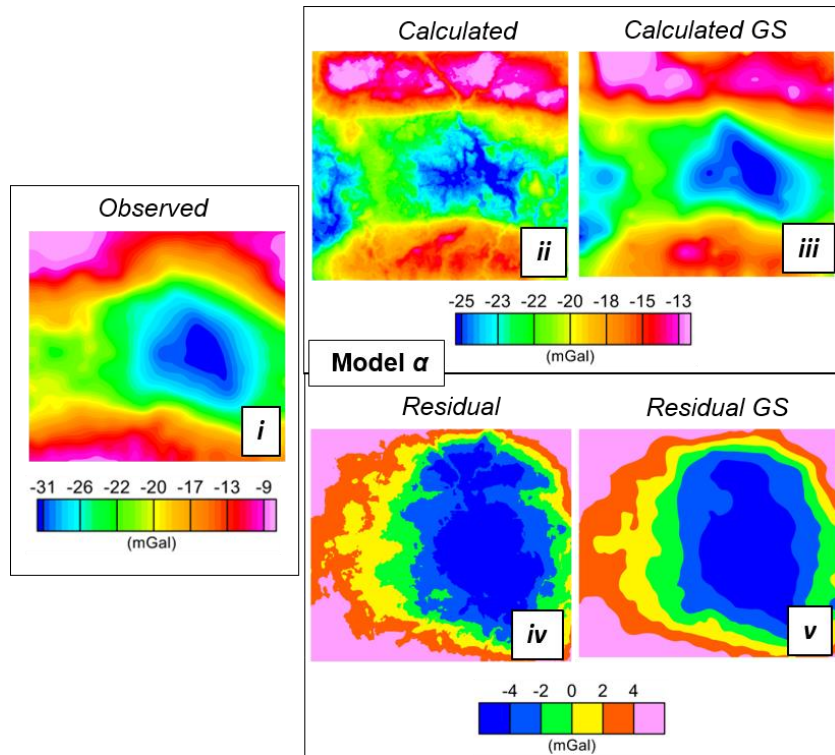


Figure 6.10. Observed data grid (*i*), calculated data grid (*ii*), and the residual data grid (*iv*) from the forward modeling of Model α . In *iii* and *v* the calculated data grid and residual data are computed solely at the gravity station (denoted GS).

Figure 6.11 shows the same data grids found in Figure 6.10, but for Model β . Figures 6.10 and 6.11 look are very similar, not only the grid maps but also the color-bar values. A more detailed comparison of the calculated data for these two models can be seen on Figure 6.12, which shows the residual data grid for Model α (*i*) and Model β (*ii*), with the difference between the two residual data grids being shown on the right (*iii*).

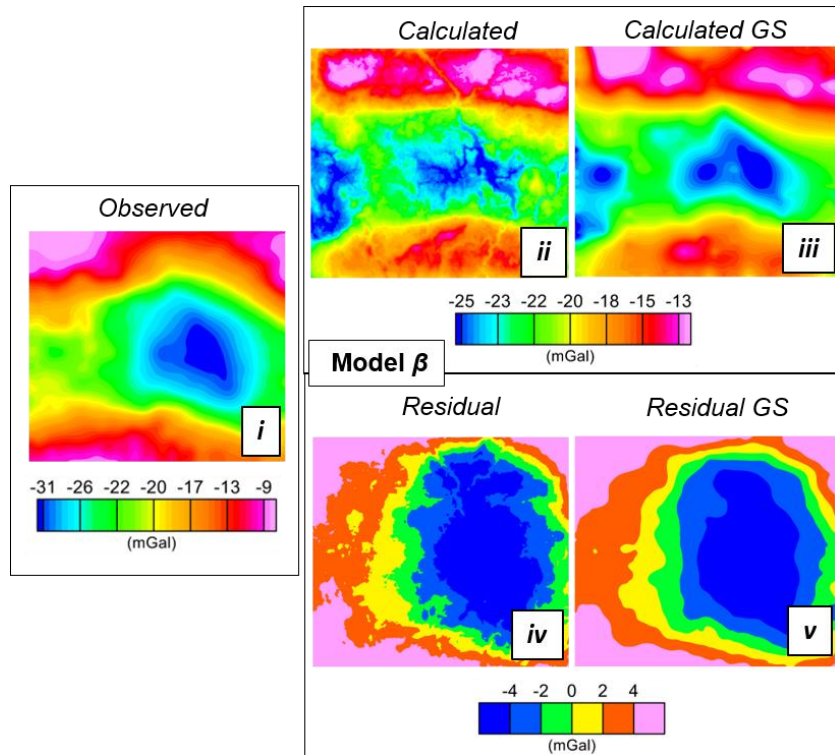


Figure 6.11. Observed data grid (*i*), calculated data grid (*ii*), and the residual data grid (*iv*) from the forward modeling Model β . In panels (*iii*) and (*v*) the calculated data grid and residual data are computed solely at the gravity station (denoted GS).

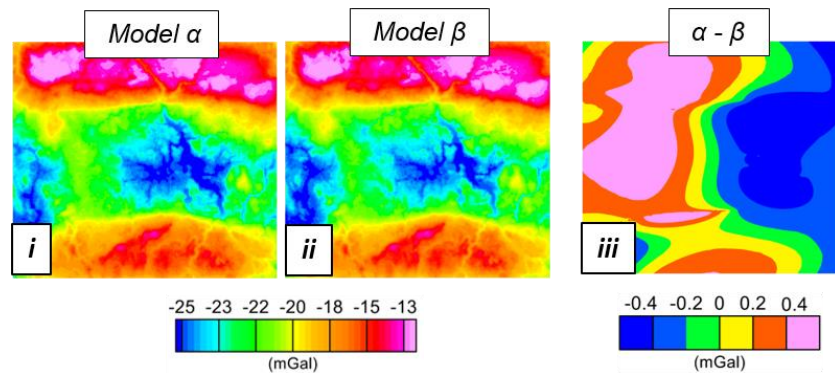


Figure 6.12. The predicted data for models α (*i*) and β (*ii*) and the grid difference (*iii*) between these two grids.

Even though the difference between the two models is less than 0.4 mGal, a west-east trend may be visualized (Figure 6.12–*iii*). This trend might be associated with the top of the Deloro assemblage, which has been included in model β and is dipping east. This systematic east-west variation might be due to the depths of the Deloro being incorrect, but these depths have been constrained by seismic data. If the seismic velocities have been estimated incorrectly, then the depths could be incorrect and the inversion could adjust these. However, the systematic variation might also be due to the densities being slightly different from what has been assumed in model β . In the following, we will assume the later explanation as it does not involve changing any of the constraints that we have applied so far in our analysis.

6.3. 3D Heterogeneous Models

In the previous section the density of the geological units in the model were defined as homogeneous, with so only one single density value was assigned to each unit. However, smoothed models (αS and βS) were obtained by allowing the inversion algorithm to smoothly vary the density of the cells within the allowable range (the mean density plus or minus one standard deviation). The means and standard deviation used for each unit are shown in Table 5.1. However, the geometry of unit contacts is not allowed to be changed. This type of inversion is called a smooth model or physical property inversion, as opposed to a geometry inversion. The physical properties can vary in a unit of interest, or multiple units (Fullagar et al., 2004)

6.3.1. Model αS (Heterogeneous)

A physical property inversion was undertaken starting from Model α , allowing the densities in all units to vary up to one standard deviation from the mean for each unit obtained from the density compilation (Table 5.1). An RMS misfit less than 1 mGal was obtained in the 32th iteration, as seen in Figure 6.13.

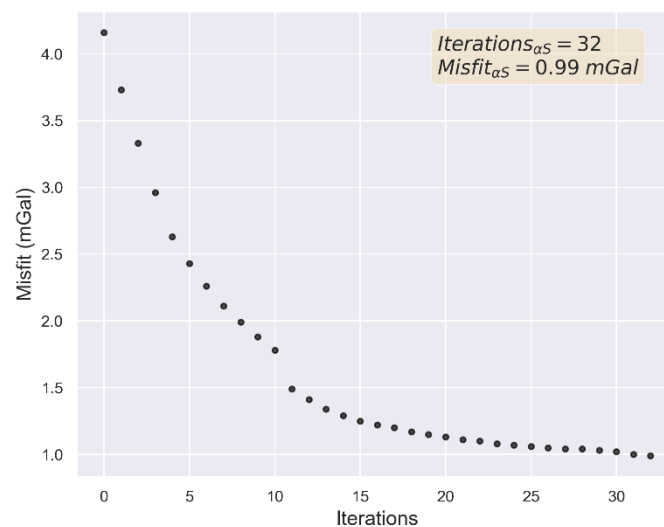


Figure 6.13. RMS misfit as a function of the number of iterations to compute the smoothed Model αS . The maximum number of iterations and the achieved misfit are on the top right of the figure.

In Figure 6.14, the model from the inversion has been visualized. In 6.14(i), a 3D view of the entire Porcupine assemblage is shown, and changes in color reflect changes in the density distribution. The same image also shows a single south-north section displaying variations in the density of the Lower Tisdale and the Kidd-Munro assemblage. In 6.14(ii), the Porcupine assemblage was removed and the Lower Tisdale and Kidd-

Munro assemblages are displayed in a perspective view. In 6.14(iii) and 6.14(iv), the lithological units are visualized.

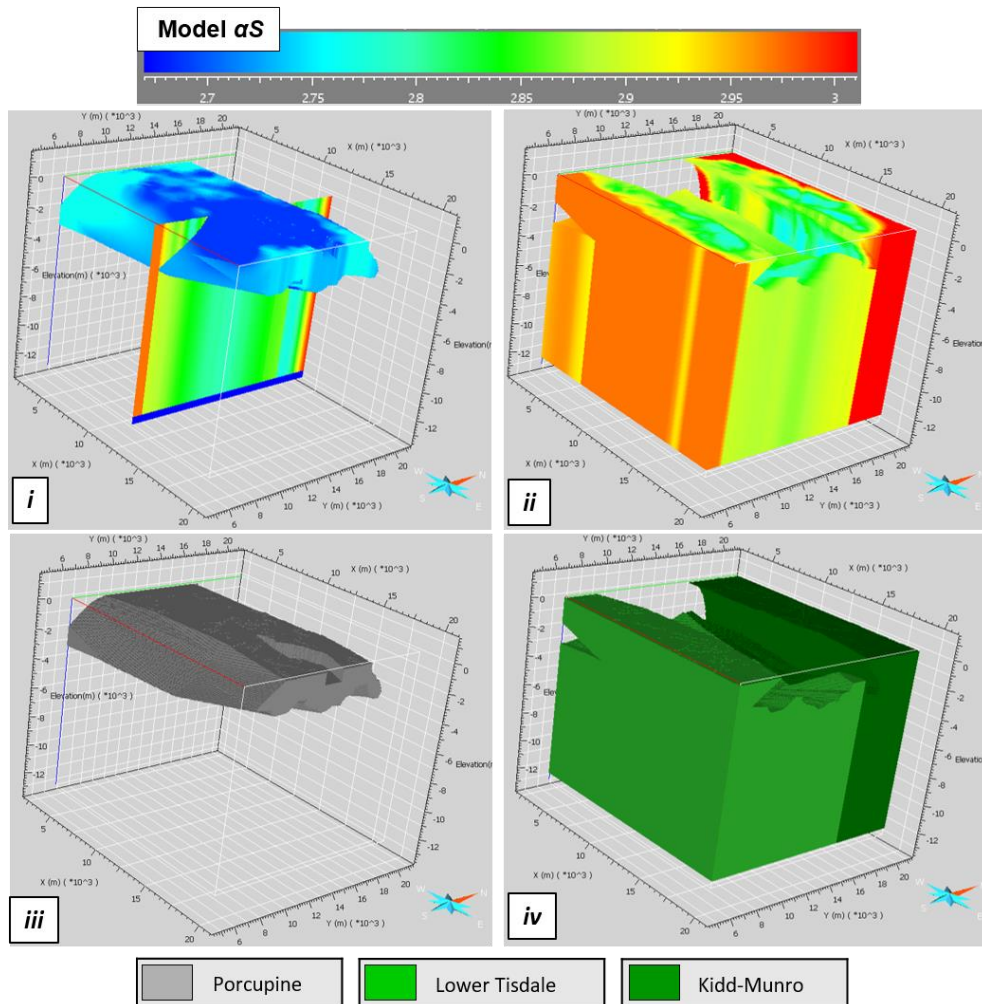


Figure 6.14. Model αS . Panel (iii) shows the volume classified as Porcupine assemblage and panel (i) shows the density variation in this assemblage and within a north-south section. Panel (iv) is the volume designated as the Lower Tisdale (light green) and Kidd-Munro (dark green) assemblages. Panel (iii) is the density variations within these two assemblages.

Figure 6.15 show the observed data, calculated data, as well as the residual data for Model αS . As expected, the calculated data became more similar to the observed data

than the homogeneous model. It is easier to see the broad scale variations when the calculated data is generated only at the gravity station points (denoted GS).

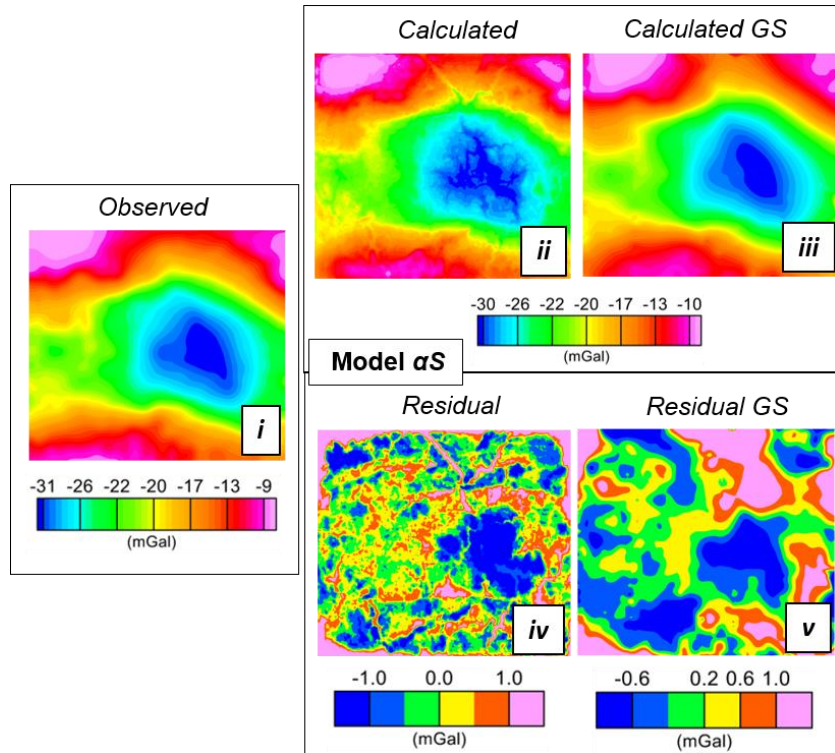


Figure 6.15. Observed data grid (*i*), calculated data grid (*ii*), and the residual data grid (*iv*) from Model αS . In panels (*iii*) and (*v*) the calculated data grid and residual data grids are computed solely at the gravity stations (denoted GS).

6.3.2. Model βS (Heterogeneous)

A physical property inversion was then undertaken starting from Model β . As with the Model αS case, the inversion was able to adjust the densities for each lithology, within the range of the mean plus or minus one standard deviation. These values are taken from Table 5.1 and Figure 6.2 for the Deloro assemblage.

As shown in Figure 6.16 the inversion was not able to achieve a RMS misfit lower than 1.00 mGal. However, the final value of 1.03 mGal is very close. The model associated with this final value, achieved after 34 iterations, is called Model βS .

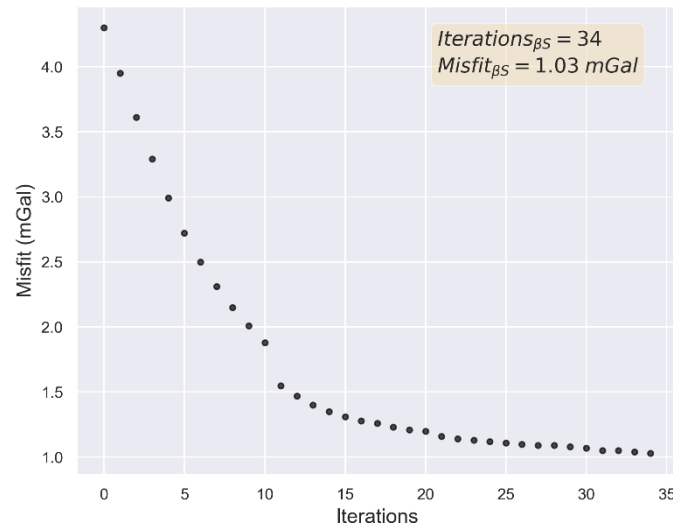


Figure 6.16. RMS misfit as a function of the number of iterations while inverting to obtain the smoothed Model βS . The maximum number of iterations and the achieved misfit are displayed on the top right of the figure.

In Figure 6.17, Model βS is shown. Figure 6.17-*iii* shows the volume occupied by the Porcupine and Figure and 6.17-*iv* shows the Lower Tisdale, Kidd-Munro and Deloro assemblage and 6.17-*i* and 6.17-*ii* respectively show the density variations within these units. Figure 6.18 is showing the calculated data grid, residual data grid as well as the calculated and residual data grid computed only using the gravity station locations (GS).

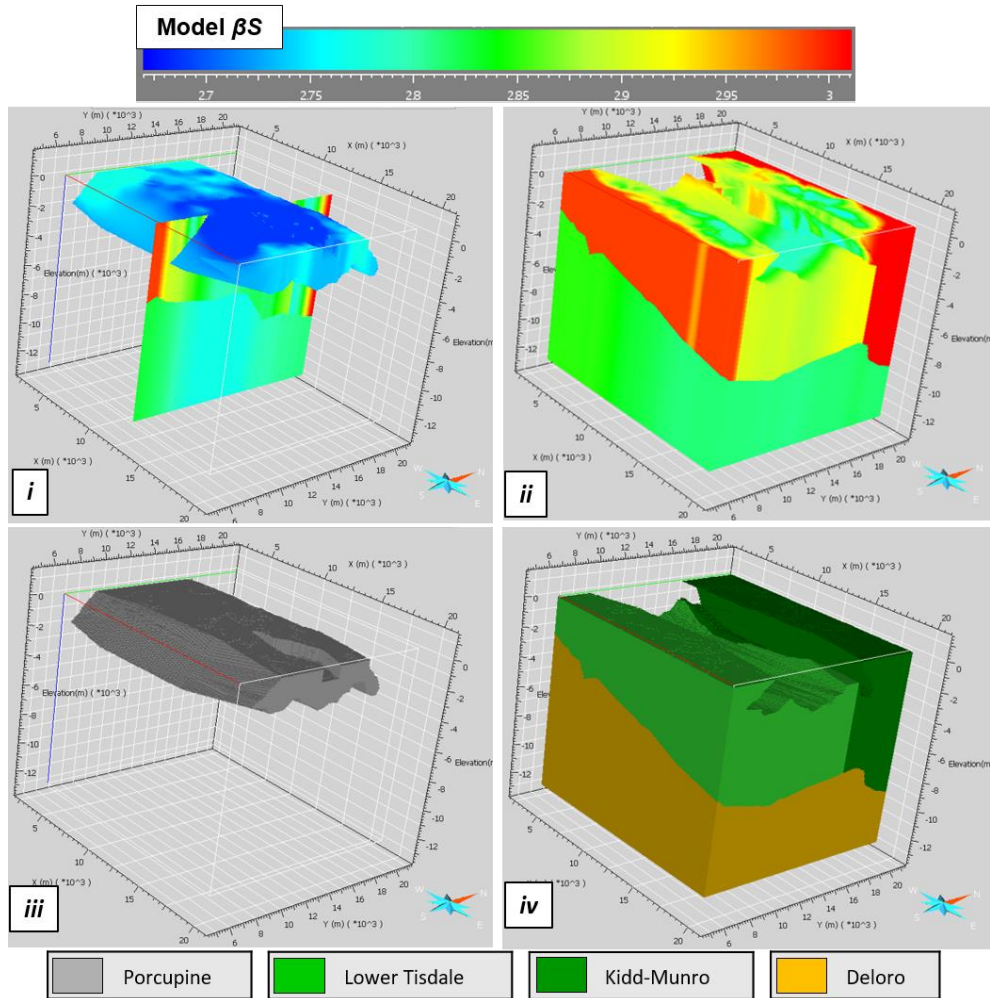


Figure 6.17. Model βS . Panel (iii) shows the volume classified as Porcupine assemblage and panel (i) shows the density variation in this assemblage and within a north-south section. Panel (iv) is the volume designated as the Lower Tisdale (light green) Kidd-Munro (dark green) and Deloro (brown) assemblages. Panel (iii) is the density variations within these three assemblages.

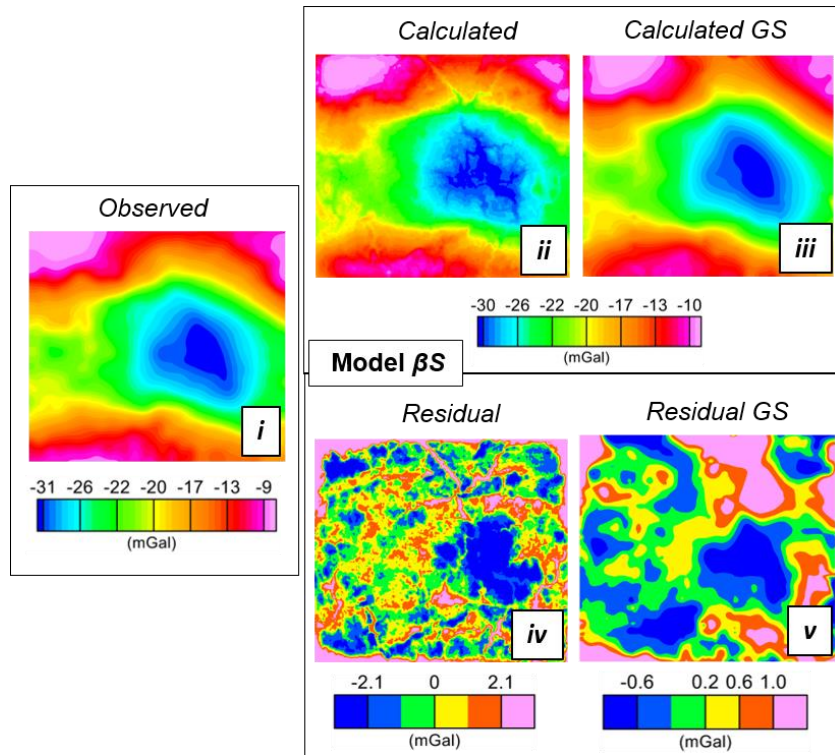


Figure 6.18. Observed data grid (*i*), calculated data grid (*ii*), and the residual data grid (*iv*) from the Model βS . In panels (*iii*) and (*v*) the calculated data grid and residual data grids are computed solely at the gravity stations (denoted GS).

6.4. Model Comparison

Table 6.2 provides the statistical information on the densities for the two inverted models. The final density means agree with each other to two decimal places (Carr, Porcupine and Kidd-Munro) or agree within the standard deviations in the cases of the Lower Tisdale. The standard deviations are also identical to two significant figures, or very close.

Table 6.2 – Density variation statistics for the computed models.

Unit	Model α S		Model β S	
	Density (g/cm ³)	St. dev. (g/cm ³)	Density (g/cm ³)	St. dev. (g/cm ³)
Carr	2.68	0.01	2.68	0.01
Porcupine	2.72	0.03	2.72	0.03
Lower Tisdale	2.88	0.05	2.86	0.06
Kidd-Munro	2.92	0.07	2.92	0.08
Deloro	-	-	2.81	0.02

The misfits in Figures 6.13 and 6.16 and the residuals in Figures 6.15 and 6.18 are essentially the same, so it is not possible to distinguish between the models using these measures. However, the actual models are quite different. Firstly, the geometry/thickness of the Porcupine assemblage has changed. In Figure 6.19, the difference in the geometry of the Porcupine assemblage is shown from two different perspectives. The geometry of model β is shown as grey, and the additional volume that had to be added to Model β to make Model α is shown in red. Secondly, the Deloro assemblage has been added at the base of the model and this unit gets shallower to the west. This model has been proposed, as it is a geologically reasonable scenario. This hypothesis is consistent with the geophysical data. In order for the hypothesis to be confirmed requires further evidence.

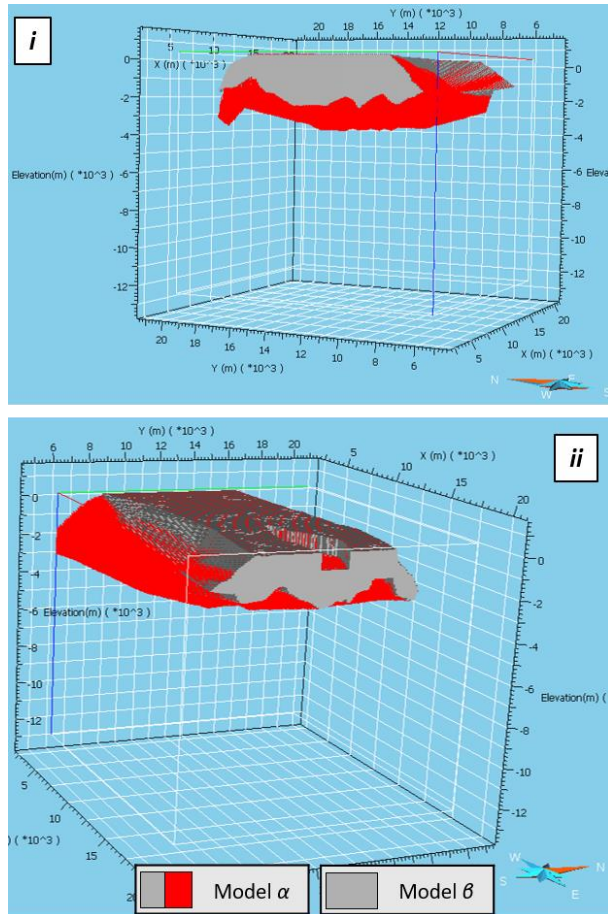


Figure 6.19. Porcupine assemblage 3D models comparison looking NE (*i*) and looking NW (*ii*).

The red material is what must be added to Model β in order to make Model α .

In this chapter the PDF angles was also estimated and compared. Once again, the values changed but the consistency between the magnitudes on the three sections (Val Gagné, Watabeag, and Matheson) remains consistent as shown in Table 6.3.

Table 6.3. Comparison of estimated PDF dip angles

Profile	Linear fault (Chapter 3)	Piecewise linear fault (Chapter 4)	Piecewise linear fault (including Deloro) (Chapter 6)
B - Val Gagné	$28 \pm 1^\circ$	30°	28°
C - Watabeag	$54 \pm 1^\circ$	49°	47°
D - Matheson	$45 \pm 2^\circ$	36°	36°

6.5. Discussion and Conclusions

The modeling in previous chapters did not take into consideration some deep reflectors evident in the seismic data. In this chapter, these were taken into account. However, because our starting model is based on 2D models, we first had to go back to the 2D profiles and include a deeper interface and hypothesize that there was less dense material (Deloro assemblage) below this interface. This 2D modeling could be used to extend the top of the Deloro assemblage associated with the seismic reflectors further to the south and north. These deep seismic reflectors suggest that the Deloro shallows to the west, which is consistent with the gravity data provided that the Porcupine is made thinner to the west, with a uniform thickness of 2000 m or less. This new model is consistent with the location of Deloro outcrops even further to the west. When these 2D models are converted to a 3D model and the gravity map data is modeled, the models that do and do not include the Deloro are both consistent with the gravity map data. Hence, it is not possible to select one model as more preferable to the other based on the gravity map data. Although the gravity profile data has a smaller uncertainty than the

grid data, the fact that the 2D profile models with and without Deloro also have comparable responses makes it difficult to draw a conclusion as to which model is most consistent with the profile gravity data. Further confirmation as to whether the Deloro exists at depth and whether the Porcupine has a thickness of less than 2000 m requires other evidence, for example drilling.

Although the Porcupine assemblage thickness and the geometry is not the same for models αS and βS , both exhibit a similar feature in the east portion of this assemblage. This continuous darker-blue low-density feature (see Figures 6.14-*i* and 6.17-*i*) might suggest the Carr intrusion is wider underneath since the density compilation shows it has a lower density than the Porcupine assemblage does. This feature might also be explained by some other intrusion(s), which would be in agreement with a more detailed geological map (Montsion et al., 2018), which shows smaller intrusions surrounding the Carr intrusion in that area.

7. Thesis Conclusions

The many models presented in this study demonstrate that the geometry of subsurface features, the depth to the interfaces and/or the density of regions can vary significantly in a subsurface model and still explain the same gravity data, as they have a similar misfit between the observed and the predicted gravity data. This is known as the non-uniqueness problem.

Geophysicists address this problem by introducing constraints to the modeling, which can use either geological or geophysical data. The following paragraphs summarize the constraints applied throughout this thesis as well as the improvement that they have brought into the model.

The first important information was the data uncertainty. By estimating the data error for the Metal Earth dataset, I could make sure that the subsurface models were consistent with these errors. If the misfit between the response of the model and the measured data is larger on average than the data error, then there is not enough complexity or variability in the model. On the other hand, if the misfit is smaller than the data error, then there might be too much complexity in the model that is not justified by the data. When modeling the data from a small part of the gravity profile on three short traverses within the Matheson study area (MSA) that cross the Porcupine-Destor fault (PDF), I found that a simple linear two-dimensional fault was able to explain the data, with the model response and measured response being comparable within error bounds. However, geophysicists are also interested in the errors in their geophysical models, and I have introduced a procedure for estimating the model errors. In this procedure, I assume

that the measured data along a profile might not be correct and replace each measurement with another random measurement that could easily have been the measured value, i.e. it is in a range that is a standard deviation either side of the mean value. The PDF dip angle can then be estimated for this perturbed profile. If the gravity profile is perturbed multiple times, then it is possible to obtain multiple dip angles, each of which is a valid estimate and consistent with the measured data uncertainty. Undertaking a statistical analysis of these dips provides a measure of uncertainty in the dip estimate. When I applied this procedure to three different traverses in the MSA (Val Gagné, Watabeag and Matheson), the estimated dip angle errors were as low as 1 to 2 degrees. This is a reasonable uncertainty for the estimate of a dip angle. If instead of using the Metal Earth data we had used the historic gravity data, then the uncertainties in this historic data are unknown and most likely are an order of magnitude larger. In that case, the uncertainties in the model dips are also significantly larger, as much as 90°, which is more than an order of magnitude.

The gravity data errors for the ME dataset were estimated using two different methodologies: error propagation and the repeatability of reduced data. While the later solely compared reduced gravity data (after all corrections are applied) at the same gravity stations, the error propagation can take into account every correction step throughout the data reduction. The data reduction details were given in Chapter 2. Both techniques showed consistency in the estimated uncertainties for free-air, Bouguer and terrain correction. Either method could be used in practise, depending on the survey size, area, costs and logistics.

The data compilation of rock densities was also important, either in the 2D forward modeling or in the 3D inverse modeling, for ensuring that the densities in the model were consistent with the physical properties of the rocks in the area. An example of this was that the unconstrained model generated in Chapter 5 gave densities in the range from 2.58 to 2.77 g/cm³, which is not consistent with the density values in the density compilation, where the major rock types had mean density values ranging from 2.63 to 2.99 g/cm³. The inconsistency of the densities in the unconstrained model with the density compilation suggests that, in this case, unconstrained modeling is not that realistic.

One example of the utility of constraining the density of surface features was evident in the 2D forward modeling. When the density on either side of the PDF was constrained, it is possible to explain the south-north gravity gradient in that area with a PDF dipping to the south. If the surface density was not constrained, then some other model, for example a gradual change in surface density, could also have been used to explain the gravity data. In the 3D inverse modeling, combining the surface geology map (or bedrock geology map) with the petrophysical data, improved the consistency between the inverse model and the density compilation. However, the bedrock geology was not realistic with deeper features in the study area being not well resolved by surface constraints alone. Model GIA had units where the geometry was oversimplified. For example, the shapes of features in model GIA were rectangular with vertical dips and constant thickness.

The high-resolution seismic sections were able to identify some reflective features that were most likely lithological contacts where there could be changes in density. When

one reflector was interpreted as the base of the Porcupine assemblage, this could be used to specify the depth of the interface between the Porcupine and the underlying Lower Tisdale assemblage. The addition of this seismic constraint in the geometry inversion of the MSA meant that model GIB (compared with model GIA) had a much smaller misfit and was a more geologically realistic model, with non-vertical dips and variable thicknesses.

Information from previous studies can also be used to constrain the data. The depth weighting in the smoothed-model inversion (Chapter 5) can be adjusted in such a fashion that the thickness of the Porcupine assemblage is consistent with the seismic interpretation on the Shillington seismic section (Snyder, 2008). In this case, the misfit between the model data and the measured data can agree to within the estimated uncertainty. In fact, it is usually possible to adjust near-surface parameters of the model to achieve an adequate misfit. Hence inferring deeper features can be difficult, unless there are strong constraints on the near-surface geology or very small data errors. Further constraints are required to resolve the deeper features. In the MSA, there was an indication of a deeper interface from the seismic data, which could be the top of the Deloro assemblage. It was possible to estimate the depth to the Deloro using 3D inversion, but only when the depth to the bottom of the Porcupine assemblage was fixed. This Porcupine depth could either be specified from the seismic data (where a reflector could be identified); or where it could not be identified, it could be re-estimated using 2D modeling in such a way that it is consistent with the seismic data and previous studies (Ayer et al., 2002; Snyder et al., 2008; Berger et al., 2011; Haugaard et al., 2021). The initial model for the 3D inversion was determined by interpolating in between the sections.

After inversion, this new model showed the Deloro shallowing to the west. Although, the new model did not show a reduction in the misfit, the *a priori* information taken into consideration enhanced the model geologically.

I found that although the misfit might be used as a guide throughout the modeling workflow, it is not the only information that should be considered. The geological feasibility of the model should provide strong guidance towards a good quality model.

I have previously mentioned that the Porcupine-Destor fault dip angles were estimated from 2D modeling on three traverses in the MSA: Matheson, Watabeag, and Val Gagné. However, the fault was also modeled with three different levels of constraints and assumptions. First of all, assuming the fault was linear and using just a few gravity stations close to the fault, the obtained angles were $28 \pm 1^\circ$, $54 \pm 1^\circ$, and $45 \pm 2^\circ$ for Val Gagné, Watabeag, and Matheson, respectively (see Chapter 3). Secondly, in Chapter 4 the fault was assumed to be slightly more complex and piecewise linear and all available ME gravity station were used, the estimated angles were approximately 30° (Val Gagné), 49° (Watabeag) and 36° (Matheson). Finally, the dips were estimated also being piecewise linear but including the Deloro assemblage into the model, the angles were 28° , 47° , and 36° for Val Gagné, Watabeag, and Matheson, respectively (see Chapter 6). Although the estimated angles for the same traverse differed quantitatively as different constraints are introduced into the model, the angles agree. The PDF is always dipping in a higher angle on the Watabeag and Matheson traverses, than on the Val Gagné traverse in all three scenarios. This suggests that the PDF is not only dipping south but also suggests a change along the strike, dipping at shallower angles towards the west.

References

- Abdelrahman, E. M., A. I. Bayoumi, and H. M. El-Araby, 1989, Dip angle determination of fault planes from gravity data: *Pure and Applied Geophysics PAGEOPH*, **130**, 735–742.
- Astic, T., and D. W. Oldenburg, 2018, Petrophysically guided geophysical inversion using a dynamic Gaussian mixture model prior: *SEG Technical Program Expanded Abstracts*, 2312–2316.
- Ayer, J., Y. Amelin, F. Corfu, S. Kamo, J. Ketchum, and K. Kwok, 2002, Evolution of the southern Abitibi greenstone belt based on U – Pb geochronology: autochthonous volcanic construction followed by plutonism, regional deformation and sedimentation: *Precambrian Research*, **115**, 63–95.
- Ayer J., P. Thurston, R. Bateman, B. Dubé, H. Gibson, M. Hamilton, B. Hathway, S. Hocker, M. Houlé, G. Hudak, V. Ispolatov, B. Lafrance, C. Leshner, P. MacDonald, A. Péloquin, S. Piercey, L. T. P. Reed, 2005, overview of results from the greenstone architecture project: discover abitibi initiative; Ontario Geological Survey, Open File Report 6154, 146p.
- Ayer, J. A., B. Dubé, and P. Ross, 2007, The Abitibi Greenstone Belt : update of the Precambrian geoscience section program , the targeted geoscience initiative III Abitibi and deep search projects; *in* Summary of Field Work and Other Activities 2007, Ontario Geological Survey, Open File Report 6213, p.3-1 to 3-44.
- Bárdossy, G., and J. Fodor, 2001, Traditional and new ways to handle uncertainty in geology: *Natural Resources Research*, **10**, 179–187.
- Bateman, R., J. A. Ayer, B. Dubé, and M. A. Hamilton, n.d. The Timmins-Porcupine Gold Camp, Northern Ontario: the anatomy of an Archaean greenstone belt and its gold mineralization: Discover Abitibi Initiative; Ontario Geological Survey, Open File Report 6158, 90p.
- Baumann, S. D., T. Arrospe, and A. E. Wolosyzn, 2011, Preliminary Redefinition of the Cobalt Group (Huronian Supergroup), in the southern geologic province: preliminary redefinition of the cobalt group (Huronian Supergroup), in the southern geologic province , Ontario , Canada: Midwest Institute of Geosciences and Engineering, Publication Number G-012011-2A.
- Berger, B., W. Bleeker, O. van Breemen, J. Peter, D. Layton-Matthew, and J. Gemmell, 2011, Results from the targeted geoscience initiative III Kidd–Munro Project; Ontario Geological Survey, Open File Report 6258, 142p.
- Berger, B. R., and D. R. B. Rainsford, 2008, 4 . Project Unit 06-001 . Gravity profiles across the Kidd-Munro assemblage: constraints on geological modelling: summary of field work and other activities 2008, Ontario Geological Survey, Open File Report 6226, p.4-1 to 4-9.
- Bevington, P. R., and D. K. Robinson, 1992, *Data reduction and error analysis for the physical sciences*: McGraw-Hill.
- Blakely, R. J., 1996, *Potential theory in gravity and magnetic*: Cambridge University Press.
- Bond, C. E., 2015, Uncertainty in structural interpretation: Lessons to be learnt: *Journal of Structural Geology*, **74**, 185–200.

- Cella, F., and M. Fedi, 2012, Inversion of potential field data using the structural index as weighting function rate decay: *Geophysical Prospecting*, **60**, 313–336.
- Chen, J., and J. C. Macnae, 1997, Terrain corrections are critical for airborne gravity gradiometer data: *Exploration Geophysics*, **28**, 21–25.
- Cheraghi, S., M. Naghizadeh, D. Snyder, R. Haugaard, and T. Gemmell, 2020, High-resolution seismic imaging of crooked two-dimensional profiles in greenstone belts of the Canadian shield: results from the Swayze area, Ontario, Canada: *Geophysical Prospecting*, **68**, 62–81.
- Darijani, M., C. G. Farquharson, and P. G. Lelièvre, 2020, Clustering and constrained inversion of seismic refraction and gravity data for overburden stripping: Application to uranium exploration in the Athabasca Basin, Canada: *Geophysics*, **85**, B133–B146.
- Della Justina, F., and Smith, R. S., 2020, 2D forward gravity and magnetic modeling of the Porcupine assemblage, Matheson area. SEG Technical Program Expanded Abstracts, 999–1003.
- Della Justina, F., and Smith, R. S., 2021, 3-D Gravity geometry inversion of the Matheson Area, Abitibi Greenstone Belt: maintaining the contacts of one of the geological unit fixed for obtaining superior results. AEGC 2021: Short abstracts. (2021). Preview, 2021(213), 63–112
- Dentith, M., and S. Mudge, 2018, *Geophysics for the mineral exploration geoscientist*, Cambridge University Press.
- Elhussein, M., 2021, New inversion approach for interpreting gravity data caused by dipping faults: *Earth and Space Science*, **8**, 1–10.
- Ehsaghi, E, Smith, R S, and Ayer, J A. 2018. Metal Earth superior data compilation. <https://merc.laurentian.ca/research/metal-earth>: Petrophysical Compilation
- Eshaghi, E., A. M. Reading, M. Roach, M. Duffett, D. Bombardieri, M. J. Cracknell, J. L. Everard, G. Cumming, and S. Kuhn, 2020, Inverse modeling constrained by potential field data, petrophysics, and improved geologic mapping: A case study from prospective northwest Tasmania: *Geophysics*, **85**, K13–K26.
- Essa, K. S., 2013, Gravity interpretation of dipping faults using the variance analysis method: *Journal of Geophysics and Engineering*, **10**. 015003 (7pp)
- Fomel, S., and E. Landa, 2014, Structural uncertainty of time-migrated seismic images: *Journal of Applied Geophysics*, **101**, 27–30.
- Fullagar, P., Pears, G., Hutton, D. and Thompson, A., 2004, 3D gravity and aeromagnetic inversion for MVT lead-zinc exploration at Pillara, Western Australia, *Exploration Geophysics*, **35**, 142–146.
- Fullagar, P., and G. Pears, 2007, Towards geologically realistic inversion: advances in geophysical inversion and modeling, **28**, 444–460.
- Fullagar, P., 2013, VPmg user documentation: <https://www.scribd.com/document/452771716/VPmg-doc-7-1>, Accessed July 02, 2019
- Geldart, L. P., D. E. Gill, and B. Sharma, 1966, Gravity Anomalies of Two-Dimensional Faults: *Geophysics*, **31**, 372–397.
- Geng, M., J. K. Welford, C. G. Farquharson, and X. Hu, 2019, Gravity modeling for crustal-scale

- models of rifted continental margins using a constrained 3D inversion method: *Geophysics*, **84**, G25–G39.
- Geoscience Data Repository for Geophysical Data, 2018. <http://gdr.agg.nrcan.gc.ca/gdrdap/dap/search-eng.php>. Gravity anomaly point data of Canada, Accessed May 05, 2018.
- Gibb, R. A., 1968, The densities of Precambrian rocks from northern Manitoba: *Canadian Journal of Earth Sciences*, **5**, 433–438.
- Halls, H. C., G. M. Stott, and D. W. Davis, 2005, Paleomagnetism geochronology geochemistry proterozoic mafic dike swarms in northwestern Ontario; Ontario Geological Survey, Open File Report 6171, 59p.
- Haugaard, R., F. Della Justina, E. Roots, S. Cheraghi, R. Vayavur, G. Hill, D. Snyder, J. Ayer, M. Naghizadeh, and R. Smith, 2021, Crustal-scale geology and fault Geometry along the gold-endowed Matheson transect of the Abitibi greenstone belt: *Economic Geology*, **116**(5): 1053–1072.
- Hinze, W. J., 2003, Bouguer reduction density , why 2.67 ? *Geophysics*, **68**, 1559–1560.
- Hubbert, K., 1948, A line-integral method of computing the gravimetric effects of two-dimensional masses: *Geophysics*, **13**, 215–225.
- Jacoby, W., and P. L. Smilde, 2009, Gravity interpretation - fundamentals and application of gravity Inversion and geological interpretation: Springer.
- Jin, X., G. Wang, P. Tang, C. Hu, Y. Liu, and S. Zhang, 2020, 3D geological modelling and uncertainty analysis for 3D targeting in Shanggong gold deposit (China): *Journal of Geochemical Exploration*, **210**, 106442.
- Kamm, J., I. A. Lundin, M. Bastani, M. Sadeghi, and L. B. Pedersen, 2015, Joint inversion of gravity, magnetic, and petrophysical data - A case study from a gabbro intrusion in Boden, Sweden: *Geophysics*, **80**, B131–B152.
- Kane, M.F., 1962. A comprehensive system of terrain correction using a digital computer. *Geophysics*, **27**, 455-462
- Kekana, S., D. Broughton, B. de Wet, N. Williams, S. Nielsen, D. Grobler, 2017, Discovery of the deep flatreef PGE-Ni-Cu-Au deposit on Turfspruit Farm, Northern Limb, Bushveld Complex, South Africa. In “Proceedings of Exploration 17: Sixth Decennial International Conference on Mineral Exploration” edited by V. Tschirhart and M.D. Thomas, 671–678.
- Kelley, K. D., H. C. Golden, M. Jessell, L. Aillères, E. de Kemp, M. Lindsay, F. Wellmann, M. Hillier, G. Laurent, T. Carmichael, and R. Martin, 2014, Next generation three-dimensional geologic modeling and inversion: building exploration capability for the 21st century. Society of Economic Geologists, Inc., Special Publication **18**, 261–272
- Khanfari, H., and M. J. Fard, 2017, An approach to correlate the statistical-based Lorenz method, as a Way of Measuring Heterogeneity, with Kozeny-Carman Equation: *International Journal of Geotechnical and Geological Engineering*, **11**, 852–855.
- Kusumoto, S., 2017, Eigenvector of gravity gradient tensor for estimating fault dips considering fault type: *Progress in Earth and Planetary Science*, **4**, 15.
- Li, Y., and D. W. Oldenburg, 1996, 3-D inversion of magnetic data: *Geophysics*, **61**, 394–408.

- Li, Y., and D. W. Oldenburg, 1998, 3-D inversion of gravity data: *Geophysics*, **63**, 109–119.
- Lindsay, M. D., L. Aillères, M. W. Jessell, E. A. de Kemp, and P. G. Betts, 2012, Locating and quantifying geological uncertainty in three-dimensional models: Analysis of the Gippsland Basin, southeastern Australia: *Tectonophysics*, **546–547**, 10–27.
- Maag-Capriotti, E., and Y. Li, 2021, Understanding the information content in gravity gradiometry data through constrained inversions for salt bodies: *Geophysics*, **86**, G35–G53.
- Mann, C. J., J. C. Davis, and U. C. Herzfeld, 1993, *Uncertainty in geology: Computers in geology – 25 years of progress*: Oxford Univ. Press, 241–254.
- Maleki, A., W. J. McNeice, F. Justina, E. Eshaghi, and R. S. Smith, 2018, Potential field data acquisition and compilation across Metal Earth’s areas of interest. Summary of field work and other activities 2018, Ontario Geological Survey, OFR 6350, 46, 1-5.
- Mahmoodi, O., R. S. Smith, and B. Spicer, 2017, Using constrained inversion of gravity and magnetic field to produce a 3D litho-prediction model: *Geophysical Prospecting*, **65**, 1662–1679.
- Menke, W., 2012, *Geophysical data analysis: discrete inverse theory*, 3rd edition.: Elsevier Inc.
- Monecke, T., P. Mercier-Langevin, and B. Dubé, 2017, Archean base and precious metal deposits, southern Abitibi greenstone belt, Canada: *Reviews in Economic Geology*, Society of Economic Geologists, **19**.
- Montsion, R M et al .2018. 1:2 000 000 scale geological compilation of the superior craton – version 1: Mineral Exploration Research Centre, Harquail School of Earth Sciences, Laurentian University Document Number MERC-ME-2018-017.
- Naghizadeh, M., D. Snyder, S. Cheraghi, S. Foster, S. Cilensek, E. Floreani, and J. Mackie, 2019, Acquisition and processing of wider bandwidth seismic data in crystalline crust: Progress with the metal earth project: *Minerals* 2019, 9(3), 145.
- Nagy, D., 1966, The prism method for terrain corrections using digital computers: *Pure and Applied Geophysics* **63**, 31–39.
- Natural Resources Canada, 2016, Geoscience data repository for geophysical data, <http://gdr.aggr.nrcan.gc.ca/gdrdap/dap/search-eng.php>, Accessed March 26, 2021.
- Natural Resources Canada, 2022, Height reference system modernization. <https://www.nrcan.gc.ca/maps-tools-and-publications/21448>. Information about the Canadian Geodetic Vertical Datum of 2013 (CGVD2013), Accessed January 10, 2022.
- Nowell, D., 1999, Gravity terrain corrections - an overview: *Journal of Applied Geophysics*, **42**, 117–134.
- Olierook, H. K. H., R. Scalzo, D. Kohn, R. Chandra, E. Farahbakhsh, C. Clark, S. M. Reddy, and R. D. Müller, 2021, Bayesian geological and geophysical data fusion for the construction and uncertainty quantification of 3D geological models: *Geoscience Frontiers*, **12**, 479–493.
- Ontario Geological Survey, 2000, Kirkland lake area - geophysical data set 1102: <http://www.geologyontario.mndm.gov.on.ca/mndmfiles/pub/data/records/GDS1102.html>, Accessed September 20, 2018.

- Ontario Geological Survey, 2005, Matheson Area - Geophysical Data Set 1055: <http://www.geologyontario.mndm.gov.on.ca/mndmfiles/pub/data/records/GDS1055.html>, Accessed September 20, 2018.
- Osmani, I. A., 1991, Proterozoic mafic dike swarms in the Superior Province of Ontario, *Geology of Ontario*, Ontario Geological Survey, Special Volume 4, **1**, 661-681.
- Phillips, J., Duval, J., and Ambroziak, R., 1993, National geophysical data grids; gamma-ray, gravity, magnetic, and topographic data for the conterminous United States, Data Series 9, <https://doi.org/10.3133/ds9>, Accessed July 20, 2021.
- Pollack, H. N., 1973, Longman tidal formulas: resolution of horizontal components: *Journal of Geophysical Research*, **78**, 2598–2600.
- Pratt, G., 2018, Time series analysis and inverse theory for geophysicists: Department of Earth Sciences, University of Western Ontario, Lecture notes.
- Reed, L., D. B. Snyder, and M. Salisbury, 2005, Two-dimensional (2D) reflection seismic surveying in the Timmins-Kirkland lake area, Northern Ontario, acquisition, processing, interpretation: Discover Abitibi Initiative; Ontario Geological Survey, Open File Report 6169, 96p.
- Roy, K. K., 2008, *Potential Theory in Applied Geophysics*: Springer.
- Roy, L., M. K. Sen, D. D. Blankenship, P. L. Stoffa, and T. G. Richter, 2005, Inversion and uncertainty estimation of gravity data using simulated annealing: An application over Lake Vostok, East Antarctica: *Geophysics*, **70**, 1–12.
- Scintrex Autograv System, 2012, Cg-5 operation manual: <https://scintrexltd.com/download/cg-5-operation-manual/>, Accessed September 20, 2018.
- Snyder, D. B., W. Bleeker, L. E. Reed, J. A. Ayer,, M. G. Houle, and R. Bateman, 2008, Tectonic and metallogenic implications of regional seismic profiles in the Timmins mining camp: *Economic Geology*, **103**, 1135–1150.
- Seequent, 2022, Montaj Gravity and Terrain Correction How-ToGuide: <http://updates.geosoft.com/downloads/files/how-to-guides>, Accessed September 15, 2018.
- Sun, J., and Y. Li, 2015, Multidomain petrophysically constrained inversion and geology differentiation using guided fuzzy c-means clustering: *Geophysics*, **80**, ID1–ID18.
- Sun, S., C. Chen, and Y. Liu, 2019, Constrained 3D inversion of magnetic data with structural orientation and borehole lithology: A case study in the Macheng iron deposit, Hebei, China: *Geophysics*, **84**, B121–B133.
- Telford, W. M., L. P. Geldart, and R. E. Sheriff, 1990, Chapter 2-Gravity Methods: *Applied geophysics*, 6–61.
- Tukey, J. W., 1977, *Exploratory data analysis*. Addison-Wesley
- Ugalde, H. A., E. L’Heureux, R. Lachapelle, and B. Milkereit, 2006, Measuring gravity on ice: an example from Wanapitei Lake, Ontario, Canada: *Geophysics*, **71**, J23-J29.
- Vaillancourt, C., 2001, Precambrian Geology of the Watabeag Lake Area: Ontario Geological Survey, Open File Report 6042

- Vallée, M. A., W. A. Morris, S. Perrouty, R. G. Lee, K. Wasyliuk, J. J. King, K. Ansdell, R. Mir, P. Shamsipour, C. G. Farquharson, M. Chouteau, R. J. Enkin, and R. S. Smith, 2019, Geophysical inversion contributions to mineral exploration: Lessons from the footprints project: *Canadian Journal of Earth Sciences*, **56**, 525–543.
- Vitale, A., and M. Fedi, 2020, Self-constrained inversion of potential fields through a 3D depth weighting: *Geophysics*, **85**, G143–G156.
- Wellmann, J. F., F. G. Horowitz, E. Schill, and K. Regenauer-Lieb, 2010, Towards incorporating uncertainty of structural data in 3D geological inversion: *Tectonophysics*, **490**, 141–151.
- Williams, N. C., 2009, Geologically-constrained UBC-GIF gravity and magnetic inversions with examples from the Agnew-Wiluna greenstone belt, Western Australia, Ph.D, thesis, University of British Columbia.
- Won, I. J., and M. Bevis, 1987, Computing the gravitational and magnetic anomalies due to a polygon: algorithms and Fortran subroutines: *Geophysics*, **52**, 232–238.
- Xia, H., and W. T. Dewhurst, 1986, Terrain corrections with variable density distributions: SEG Technical Program Expanded Abstracts. Society of Exploration Geophysicists, 142–143.
- Yun, Z., X. Sun, Y. Wang, and J. Li, 2019, Finding buried hills by using high resolution gravity and magnetic data integrated with seismic data: GEM 2019 Xi'an: International Workshop on Gravity, Electrical & Magnetic Methods and Their Applications Xi'an, China, May 19–22, 2019, 149–152, 10.1190/GEM2019-038.1.
- Zhong, Y., Z. Ren, J. Tang, Y. Lin, B. Chen, Y. Deng, and Y. Jiang, 2022, Constrained gravity inversion with adaptive inversion grid refinement in spherical coordinates and its application to mantle structure beneath Tibetan plateau: *Journal of Geophysical Research: Solid Earth*, **127**, e2021JB022916.